Trapped Atoms in Cavity QED for Quantum Optics and Quantum Information

Thesis by

Jason McKeever

In Partial Fulfillment of the Requirements

for the Degree of

Doctor of Philosophy

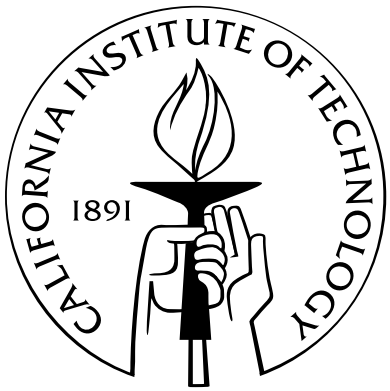

California Institute of Technology

Pasadena, California

2004

(Submitted June 3, 2004)

© 2004
Jason McKeever
All Rights Reserved

Acknowledgements

My first thanks go to Jeff Kimble for providing me the opportunity to work in this exciting field, and to be a part of his outstanding research group. Needless to say, his tireless efforts have played an instrumental role in the progress we've made these past few years. Beyond this direct contribution, I have learned immeasurable amounts from him, not only in terms of scientific skills both theoretical and experimental.

I also owe a debt of gratitude to my colleagues from Lab 11, where all the work in this thesis was done. This list begins with David Vernooy and Jun Ye, who constructed the heart of the experiment, which continues to beat to this day. Postdoctoral fellows Dan Stamper-Kurn and Hanns-Christoph Nägerl provided excellent leadership, and I learned a great deal from both of them. Special thanks also go to Joe Buck, with whom our first real breakthroughs were achieved. Joe was a great friend and colleague throughout both the good times and the months before that weren't quite as pleasant. Alex Kuzmich provided several important scientific contributions to our lab, which are greatly appreciated. Andreea Boca, David Boozer and Russ Miller have been tremendous friends and co-workers, and a separate paragraph of gratitude could be written about each of them. Amazing progress already being made as of this writing is a testament to the fact that the lab could not be in better hands.

Beyond the few I have just named, with whom I have directly interacted the most, I gratefully acknowledge everyone else in the Quantum Optics group whose time has overlapped with mine. I am lucky and proud to have spent several years with this fine collection of people.

I will always value the great friends I have made at Caltech, with whom I hope to stay in contact for years to come. Ali Husain and Ed Chen have been great roommates through several years and a couple of apartments too many. Although I hesitate to start listing others by name for fear of glaring omissions, some fellow members of my incoming class deserve special mention: Paul Skerritt, Martin Griffiths, Alexei Dvoretskii and Michele Vallisneri. Also I cannot leave out "the fools", who know all too well that I use that term with only the most complimentary intentions.

Finally, I deeply appreciate the support I've received from my family, in particular my parents Pat and Garry McKeever. Their unquestioning support through sometimes trying times has been essential for the completion of this work.

Abstract

One of the requirements for the physical implementation of many protocols in quantum information science is the ability to convert quantum information from stationary to travelling form and transmit it over long distances. The strong coupling domain of cavity quantum electrodynamics (QED) provides a near-ideal setting for the pursuit of these goals. In addition, cavity QED is a unique system for the study of open quantum systems and quantum coherence. Cavity QED experiments have entered a new era in recent years, with the advent of single atom intracavity trapping.

Experiments described in this thesis represent significant progress in these areas. Beginning with a tremendous set of improvements to far-off-resonance optical trapping of single Cs atoms in a Fabry-Perot resonator, we have undertaken a series of investigations in which strongly coupled trapped atoms have been used for quantum optics and quantum information. These improvements in trapping go beyond quantitative lengthening of storage times, in that the trap is largely insensitive to the atom's internal state.

As a result of this unique property of the optical trap, a breakthrough was made in the continuous observation time of trapped atoms. Individual atoms can be observed for times of order 1 second, and this scheme enables real-time monitoring and measurement of the number of atoms strongly coupled to the cavity. This enables deterministic preparation of a particular atom number of the experimenter's choice.

Using single trapped atoms in our cavity, we have also experimentally realized the one-atom laser in a regime of strong coupling. The unconventional characteristics of this system are explored in detail, including strongly nonclassical output. This represents a significant milestone of long-standing interest in the quantum optics community, and goes beyond previous work with atomic beams where there was a fluctuating atom number in the cavity.

Finally, we have achieved the first deterministic generation of single photons in a setting suitable for quantum networks. By illuminating a strongly coupled, trapped atom by classical laser pulses, single photons have been generated on demand, with intrinsic efficiency near unity. Although a great deal of work remains to configure this system as a true node in a quantum network, the ground-work has been laid for progress in the near future, where one goal is to create an entangled state of two atoms in distantly separated cavities.

Contents

Chapter 1

Introduction

The confinement, isolation, and manipulation of individual particles has been a long-standing pursuit of experimental physicists. There is a fundamental desire to reduce systems down to their elementary constituents and to study interactions and behavior at a basic level, including the emergence of quantum phenomena. Within the realm of atomic and optical physics, the ion trapping community has played a pioneering role in leading this charge [1, 2]. Laser cooling and trapping was also applied to neutral atoms, leading to an explosion in this field throughout the 1990's [3, 4, 5]. These techniques led to the study of single trapped neutral atoms, first in magneto-optical traps [6, 7, 8, 9] and magnetic traps [8], and later in optical dipole traps [10, 11].

The field of quantum information science (QIS) [12] has been simultaneously emerging along with this development and expansion of laser cooling and trapping. In fact, cold, trapped atoms and ions are considered one of the best candidates for the experimental realization of QIS protocols and systems [13]. Electromagnetic fields can be used to cool and trap atoms, their long-lived internal states are well suited for the storage of quantum information, and the interaction of atoms with laser light can be used for readout and transmission. More specifically, many of the standard, accepted physical requirements for quantum computation [14] are satisfied by the ability to confine a small number of atoms in such a way that they are individually addressable by laser light and can undergo controllable interactions with each other. Trapped ion systems seem to be the leading candidate right now [15], and tremendous progress is being made [16, 17].

However, the field of quantum information science extends beyond the realm of local quantum computation. Indeed, there is a strong interest in the ability to convert stationary quantum information to a mobile type (hence the term *flying* qubits [18]). This must then be complemented by the ability to faithfully transmit these flying qubits across long distances. These requirements are considered crucial for ideas of quantum communication, which are intimately connected to quantum computation and represent a major component of QIS in general [14].

The main system typically considered for the achievement of these goals is cavity quantum electrodynamics (QED) in the regime of strong coupling [19, 20]. In particular, one or several trapped

atoms strongly coupled to an optical cavity could represent a node in a quantum network, and schemes exist where quantum information can be transmitted from one node to another using optical interconnects, such as fibers [21, 22]. The strong interaction between the atom and the optical field is enabled by small cavity mode volume and high resonator quality, allowing coherent interactions to dominate dissipation. These attributes permit the reversible interconversion of stationary qubits (hyperfine atomic ground states) to flying qubits (optical photons). Beyond its applicability to QIS, however, cavity QED is a unique system suitable for many other types of scientific investigation. As has been documented extensively over the years, cavity QED provides an open quantum system with well-understood interactions (see, e.g., Ref. [23] and references therein). This system then enables studies of quantum control and feedback, real-time observation of quantum dynamics [24], and more generally the study of quantum coherence. Hopefully, the developments described in this thesis, in particular the improvements in the ability to confine an atom in a cavity, could lead to fruitful research in these fields.

This thesis documents a series of cavity QED experiments undertaken the past several years in the Caltech Quantum Optics group. Specifically, these experiments are based on trapping single cesium atoms inside an optical cavity, aiming toward the realization of a quantum network. David Vernooy and Jun Ye [25, 26] laid the foundations for these efforts starting around 1998, to be continued by a large group of researchers since then. In this thesis I will concentrate on the period beginning in the summer of 2002, when a dramatic improvement in trapping ability was achieved. This improvement allowed us to qualitatively change our approach from concentrating only on intracavity trapping to using the atom-cavity system for experiments in quantum optics and quantum information science. In this introductory chapter I intend to briefly describe each one of these experiments, and to place them in the broader context of other similar experiments in the community.

The aforementioned breakthrough in trapping is documented in Ref. [27] and Chapter 3, where mean storage times of 2 to 3 seconds for single Cs atoms were achieved. This was, and still remains, the longest trap lifetime ever realized for atoms in the strong coupling regime of CQED, and eclipses the previous best by two orders of magnitude [26]. The mechanism for trapping is the optical dipole force, in the far-detuned regime (far-off-resonance trap, or FORT). The central idea for our system is to use a longitudinal mode of the cavity to sustain a standing-wave FORT, so that the trapping takes place in the same region as the cavity QED interactions. Although this integration of optical trapping with cavity QED proved to be a substantial technical challenge, we achieved a long-standing goal, the first step toward the creation of a viable node for a quantum network. In order to achieve our success in trapping, we had to diagnose, understand and correct several technical problems involving our trap, some of which are extensively documented in Ref. [28].

A critical feature of our FORT is its state-insensitive nature, meaning the strength of the trap is only weakly dependent on the atom's internal state. Stated differently, the atomic excited states

are shifted by nearly the same amount as the ground states, meaning the critical optical transition for cavity QED experiences only a small shift. This presents important advantages such as the simplification of atom-cavity spectroscopy, and the facilitation of laser cooling of trapped atoms. Our experiments are unique in that they combine this state-insensitivity with the strong coupling domain of cavity QED. In ion trapping systems, the internal and external degrees of freedom are indeed independent, but the cavities in these experiments have yet to reach the strong-coupling regime [29, 30]. Other cavity QED experiments with trapped neutral atoms have been done with more conventional FORTs, where the excited state is not trapped [31, 32].

Not only did we dramatically improve atomic storage times in these experiments, we also demonstrated continuous observation of trapped atoms for unprecedented durations, thanks in part to the state-insensitive FORT. This was another major milestone since all protocols seeking to use CQED for quantum information science require the ability to optically address trapped atoms in a non-destructive manner. These results are mentioned in Chapter 3, and documented more extensively in Chapter 4 and Ref. [33]. A central feature of this scheme is the ability to determine the number of atoms trapped in the cavity in real time. The ability to count intracavity atoms is important not only for experiments requiring multiple atoms in the same cavity. It also circumvents a possible criticism of our experiments: the fact that we load our trap in a "non-deterministic" manner. Other experiments have been built around the idea of delivering a pre-determined number of trapped atoms into a cavity region [34]. Although our experiments indeed lead to random trap-loading, in Chapter 4 we outline a scheme for quickly measuring the atom number, which is possibly faster than the other deterministic schemes.

The achievement of this continuous probing was a crucial stepping stone on the way to our next major accomplishment: the experimental realization of a one-atom laser in the regime of strong coupling. In this experiment, which was reported in Ref. [35], we configured our atom-cavity system as the fundamentally simplest possible laser (see Chapter 5 of this thesis). As a result of the strong atom-field coupling and highly quantum nature of the interaction, this device had very different characteristics from a conventional laser, and we explored these features in detail. We observed nonclassical, or manifestly quantum photodetection statistics of the output light, characterized the output power vs. pumping strength, and compared these results with various theoretical models. Although research on "single-atom" micromasers and lasers has been reported in the past, those experiments were performed with atomic beams in which the intracavity atom number was fluctuating, with one atom on average, and each atom only incrementally contributing to the output.[1] By contrast, our experiment was done with one and the same atom trapped in the cavity for times much longer than necessary to reach steady-state.

The one-atom laser led naturally to the next step along the road to quantum networking: the

[1] See references in Chapter 5/Ref. [35]

deterministic production of single photons using our atom-cavity system. We accomplished this goal in the autumn of 2003, with results comparable to or better than the state of the art in the literature. As documented in Ref. [36], photons were produced with near unit efficiency, and two-photon events were suppressed by more than 20-fold compared to a coherent state. Our system provides an intrinsically coherent and reversible photon source where the internal atomic state decoheres slowly, so that it can remain entangled with the state of the cavity output field, precisely the requirement for the implementation of a quantum network.

Although the experiments described herein do represent significant progress toward the stated goals, there remains a great deal to be done. Atomic confinement inside the cavity has developed nicely, but other atomic degrees of freedom have remained uncontrolled. For instance, further cooling of trapped atoms would be desirable, potentially leading to the investigation of quantized center-of-mass motion in cavity QED [37]. The magnetic sublevel of the trapped atoms also needs to be deterministically prepared and maintained for many schemes. However, experiments underway as of this writing are making tremendous strides toward full control of both of these variables. Some goals for the immediate future in this laboratory are to demonstrate the indistinguishability of our single photons, and the coherent reversibility of the photon emission. With these goals and improvements imminently realizable, the possibility of entangling two atoms in distantly separated cavities definitely seems within reach.

Chapter 2

Experimental Apparatus

2.1 Introduction

The apparatus for the experiments described herein has a long history, and many students and postdocs deserve credit for its evolution over the last 5 years or more. The vacuum chamber was constructed by David Vernooy and Jun Ye around 1998-99 [25, 26], and some fraction of the equipment and table setup were left over from experiments done by Hideo Mabuchi and Jun Ye on the same table in earlier years [38, 39]. Jun and Dave's chamber has been stable and functioning continually since its construction, and this should not be underestimated as a factor in leading to the successes in the lab since late 2002. In this section I will concentrate on the layout of the experiment on the optical table, since it seems that this area has undergone an important set of changes since Dave documented the experiment in his thesis [25]. We have simplified and upgraded the setup little by little since he and Jun moved on, and the cumulative effect of many seemingly incremental changes has been substantial. As for the vacuum chamber, the various sets of coils and the cavity construction (ours in particular [25] and newer techniques in general [40, 41]), I defer to previous theses and possibly future ones. Notably, Joe Buck did some analysis of the properties of our particular vacuum system, including the pressure in the cavity region and its effect on the rate of collisions [28].

I will discuss the experimental layout in three main parts, the first of which, Section 2.2, describes the cavity "input side," namely, the lasers and metrology necessary for introducing the relevant intracavity fields. Section 2.3 will outline the output side, mostly the photodetection schemes we have used and the techniques for separating the fields at different wavelengths. Finally, Section 2.4 will go over the lasers and frequency control required for the two magneto-optical traps (MOTs) and the beams delivered to the cavity mode region "from the side" (in the transverse direction).

2.2 Frequency metrology and cavity inputs

The layout of the optical table leading to the cavity input is schematically depicted in Figure 2.1. This section will be divided into three parts, one for each of the lasers that drive standing-wave modes in the physics cavity (PC). It is worth noting that the experiment as it functions today employs only diode lasers. Although it can be difficult to procure single-mode diodes at particular wavelengths, and sometimes our home-built systems can be unreliable, commercial systems for larger, more unwieldy lasers are often just as bad and require a good deal more maintenance. All things considered, this all-diode configuration has been very convenient and stable.

2.2.1 Diode laser for cavity QED interactions

In early generations of this and other cavity QED experiments [25, 40], Ti:Sapphire lasers were used for driving the cavity modes near the cesium resonance. Improvements to diode laser designs introduced to the group primarily by Hanns-Christoph Nägerl, along with an accompanying increased confidence in their reliability, led to a change in philosophy around the year 2000. In spite of concerns about known high-frequency phase noise on diode lasers [42], we decided to begin using one for our cavity QED probe laser, which I will refer to as the CQED laser. As it turns out, this seems to have been a good idea, and the noise issues have caused no known problems to date.

Besides switching to the diode system, we have also re-configured the frequency metrology and laser locking scheme since Ref. [25]. The basic principles of the locking scheme are still the same, but the particular frequencies used and techniques for shifting them have changed. It is useful however to begin with a brief recap of the locking scheme relevant to the CQED laser. The transition in cesium used for experiments described herein is the D2 line at $\lambda_0 \approx 852.36$ ($6S_{1/2} \rightarrow 6P_{3/2}$). More specifically, we tune the probe beam to transitions involving the $F = 4$ hyperfine ground state, and either the $F = 4'$ or $5'$ excited states (which are separated by a 251 MHz hyperfine splitting). The frequency locking and shifting scheme to be described can be used for these and other transitions. For detailed information on cesium I refer to the excellent set of notes compiled by Daniel Steck [43].

The CQED laser is locked to the transfer cavity (TC), for reasons described in Refs. [25, 39] and below. We use the Pound-Drever-Hall technique for this [44], with the reflected light directed to a fast photodetector (PD1). The sidebands at 45 MHz are generated by an electro-optic modulator (EOM1) which sits in the path to the TC only, meaning that the sidebands are not on the light that reaches the physics cavity (PC). When the diode laser was first set up for CQED, these sidebands were generated using modulation of the diode current. Due to concerns over unwanted frequencies possibly causing atomic heating, we switched to the EOM setup; it turned out however that this made no measurable difference.

Once this prestabilization on the TC is achieved, the system drifts freely on long timescales

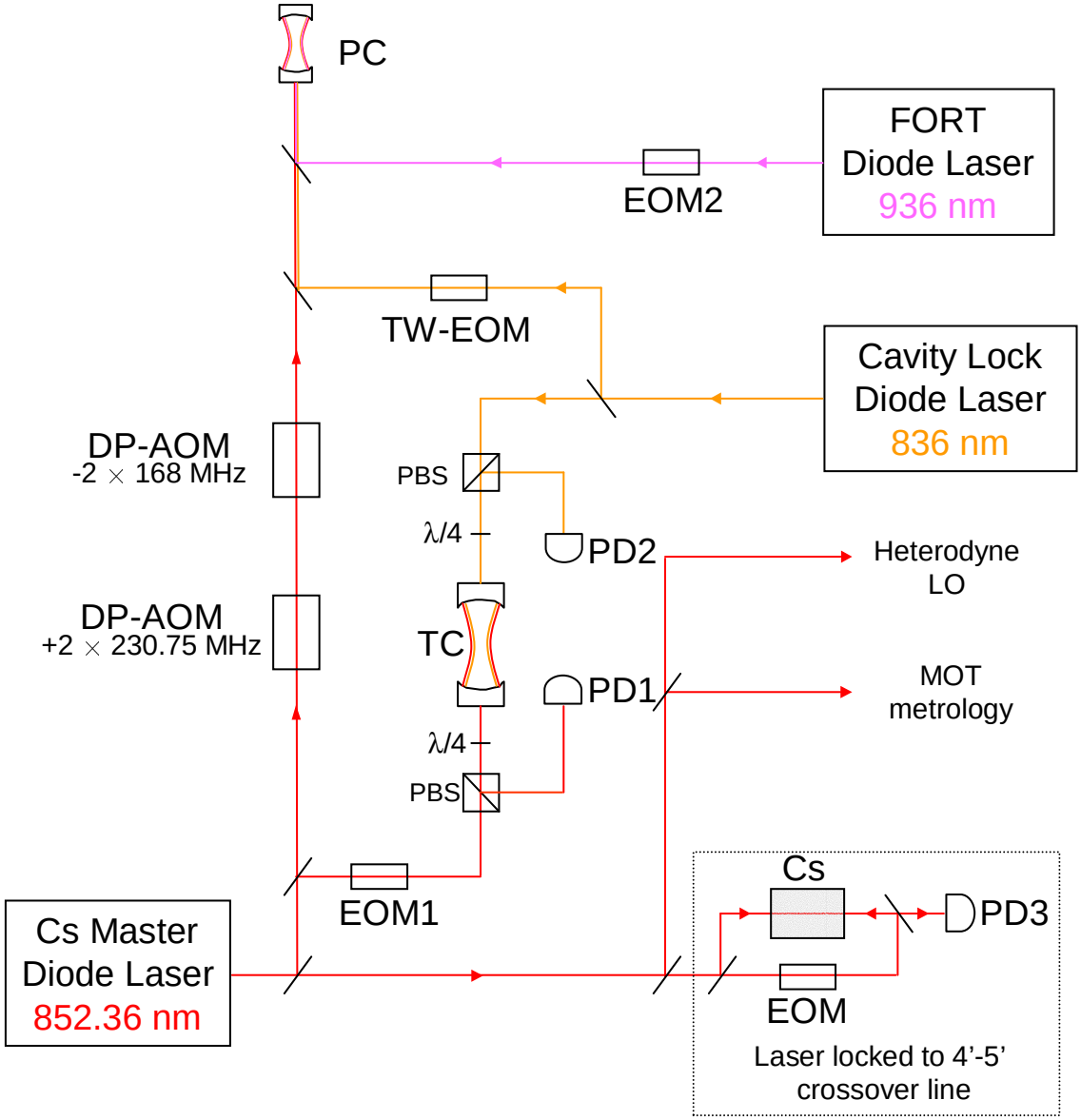

Figure 2.1: Schematic diagram of lasers and metrology for cavity QED, in particular the cavity input side. Some of the light is diverted to the heterodyne detectors as the local oscillator (LO) (see Fig. 2.2), and some to provide a frequency reference for cooling and trapping (MOT metrology, see Fig. 2.2). (TW-)EOM: (Travelling Wave) Electro-optic modulator, (DP-)AOM: (Double passed) Acousto-optic modulator, PD: Photodetector, PC: Physics cavity, TC: Transfer cavity, PBS: Polarizing beam splitter, $\lambda/4$: Quarter-wave plate.

with the TC length, which then needs to be referenced to the cesium transition. In other words, fast frequency fluctuations are eliminated by the TC lock for all intents and purposes, but absolute frequency stablility is not yet established. This latter goal is accomplished using modulation transfer spectroscopy on a Cs vapor cell [45, 46] (symbolically enclosed in the dotted box in Fig. 2.1). Using this spectrum, the length of the TC (via the CQED laser frequency) is locked to the crossover

resonance with frequency halfway between the $4 \rightarrow 4'$ and $4 \rightarrow 5'$ transitions. This means that the laser frequency is about 125.5 MHz below $4 \rightarrow 5'$ and above $4 \rightarrow 4'$. Earlier generations of the experiment locked to the $4 \rightarrow 5'$ transition with an offset of 40 MHz to the blue [25, 26].

The light directed to the physics cavity thus begins at this crossover frequency, and needs to be shifted according to the cavity QED experiment of choice. This is accomplished using a pair of double-passed acousto-optic modulators (DP-AOM) configured in series. The frequencies indicated in Fig. 2.1 correspond to the $4 \rightarrow 5'$ transition with zero detuning, as can be easily verified by noting that twice the difference in the drive frequencies is 125.5 MHz. Swapping these frequencies addresses the $4 \rightarrow 4'$ transition instead. We chose to use two double-passed AOMs in order to achieve broad tunability and high extinction ratio. Alternatively, for example, we could have elected to use one single-passed AOM around 125.5 MHz, but to cite one of many drawbacks, this would have restricted us to addressing only one hyperfine transition with small detuning.

The previous scheme for shifting the frequency involved one AOM and a travelling wave EOM, which generated a sideband near 240 MHz [25, 26]. This sideband itself was used as the probe and its absolute frequency was tuned to the resonance of choice. The downside of this technique is that the carrier, albeit fairly far-detuned from the atom-cavity resonance, remains on continuously. This means that residual off-resonant light gets into the cavity, and experiments with Dan Stamper-Kurn in 2001 revealed that this was a very significant source of atomic heating. At that time we discovered that switching off the probe by eliminating the EOM sideband was insufficient, and that we also had to switch off the upstream AOM. This increased the trapping times from below 1 ms to several tens of ms. Unfortunately we never understood the discrepancy between these lifetimes and those of Ref. [26] (where the AOM was not switched off and a 28 ms trap lifetime was achieved). However, this concern alone does not explain the change to the two-DP-AOM configuration, since we seemingly resolved the early scheme's main problem by switching off both the EOM and the AOM. The other concern that led to the change was that in the EOM scheme, the carrier still shines while the probe is *on*. This means that a known source of unwanted light gets into the cavity during experiments in which a probe is needed. It is a near certainty that we could not have done the experiments we eventually did (e.g., Chapter 4) without eliminating this problem.

2.2.2 Diode laser for locking the physics cavity

The next laser necessary for these cavity QED experiments is a dedicated laser for locking the physics cavity to a stable and precisely tunable absolute frequency [39]. We will refer to this laser as the locking laser. Ref. [25] includes a detailed description of this locking scheme, so here I provide only a brief discussion.

The first question to be addressed regarding this laser is why do we need it at all? After all, the CQED laser provides a very stable beam referenced to cesium to which the cavity could be locked.

There are several problems with this simple approach. The first is that the probe beam at λ_0 would have to be on continuously for the feedback loop to be functioning, and in experiments described herein, the probe beam sometimes needs to be *off* for long periods of time. The second is that CQED probe beams typically have very low power (on the order of pW) so that shot noise would place severe limits on a feedback loop. Thirdly, introducing detunings between the probe and the cavity would be difficult, especially detunings larger than the cavity linewidth.

With these considerations in mind, it is clear that a continuous beam is needed which couples as little as possible to the atom's motion and its internal state. The ideal situation would be a beam with very large detuning from λ_0 for which the cavity finesse is still very high. This way, the laser can drive a longitudinal mode of the cavity for the purpose of length stabilization, and the field has a negligible effect on the atom. Unfortunately the two criteria of large detuning and high finesse conflict to some extent, because the cavity coating is optimized for high reflectivity at the atomic transition λ_0. Fortunately, the frequency of the locking beam can still be far-detuned by atomic physics standards while still being close to the optimal cavity coating. The wavelength chosen for these purposes by Dave and Jun was $\lambda_L = 836$ nm, which corresponds to two free spectral ranges from the mode at λ_0. The fact that $\lambda_L < \lambda_0$ means that the standing wave at λ_L creates a repulsive force on the atom. See below for a quantitative discussion of this effect and other issues related to this laser.

We turn now to a description of the frequency metrology setup for this locking laser, and thus the physics cavity. The one basic principle still to be explained is that the locking laser is only useful if its frequency can be stabilized and referenced in an absolute manner to the cesium resonance. This is the purpose of the transfer cavity, which in the final configuration is doubly resonant with both the locking and the CQED lasers (see Fig. 2.1). Since both lasers are locked to the TC and since the TC is stabilized to constant absolute length (see Section 2.2.1), the frequency spacing of the two lasers is constant.

The procedure for completing the physics cavity lock begins by tuning the CQED probe beam at λ_0 to the desired physics cavity resonance frequency. This chosen frequency near c/λ_0 then dictates the ultimate cavity length, and hence the target frequency $\nu_L^{(0)}$ for the locking laser (the resonance two modes to the blue).

The next step is to decide which of the TC's modes to lock the laser to. At this stage, the TC already has fixed length (it has been locked to cesium) so that its modes correspond to a fixed set of frequencies (integer multiples of the TC's free spectral range, $\nu_{FSR}^{(TC)} \approx 500$ MHz). This means that the locking laser will be set to an arbitrary frequency which coincides with one of the TC modes, in general different from the target $\nu_L^{(0)}$. By scanning the PC around the resonance at λ_0 and monitoring the PC transmission at both λ_0 and λ_L and the TC transmission at λ_L, one can tune the frequency of the locking laser around until a TC mode near $\nu_L^{(0)}$ is found. Operationally,

this means looking for the locking laser to jump into TC lock when the λ_L transmission peak is close to the λ_0 peak on the PC scan. At this stage, the two lasers have fixed frequencies that do not quite correspond to a double resonance of the PC ($|\nu_L - \nu_L^{(0)}| \lesssim \nu_{FSR}^{(TC)}$).

This discrepancy between the closest TC resonance and the target $\nu_L^{(0)}$ necessitates a frequency shifting element for the locking beam sent to the physics cavity. The choice of the travelling-wave electro-optic modulator (TW-EOM) was made due to its broad tunability (in my experience we have used it from around 50 MHz to almost 1 GHz, but it may be useful up to much higher frequencies). The cavity is ultimately locked to one of the sidebands generated by the TW-EOM (i.e., the absolute frequency of one the sidebands is set to $\nu_L^{(0)}$). The fact that we need very little power at λ_L for the PC lock (of order nW) means that the typical 10% sideband fraction is not a problem at all (the laser output is several mW). The final detail to discuss is that in order to use Pound-Drever-Hall to derive an error signal and lock the cavity, the sideband used must *itself* have sidebands on it. This is accomplished by applying frequency modulation to the radio frequency source which generates the sideband in question (see ref. [25] for additional details).

Turning now to some quantitative details, the sideband used for locking the physics cavity contained about 7 nW of output power according to the most recent measurement. Although a good measurement of the cavity finesse at $\lambda_L = 836$ nm is required for an accurate determination of the corresponding peak intracavity intensity, our best estimates yield an upper bound of approximately $I_L = 7.5 \times 10^6$ W/cm^2. This gives a maximum ac Stark shift of about 250 kHz.[1] This is a fairly large Stark shift, representing about 0.5% of the FORT depths used in experiments to date. Since the standing waves from the locking and FORT lasers are of different wavelengths, each well of the FORT is distorted by the trapping light in a different way. Additionally, these distortions will effectively be amplified in any future experiments where the FORT depth is lowered, unless a comparable reduction of the locking power is feasible. Reduction of the FORT depth is desirable for the purpose of reducing decoherence from FORT scattering. In order to alleviate this concern it will be necessary at some point to do a serious signal-to-noise analysis of the physics cavity locking and the implications for the possibility of reducing this power. Incidentally, the scattering rate arising from this intensity estimate is $\Gamma_L = 1.1$ s^{-1}, lower by about a factor of 50 from the FORT scattering rate (see chapter 3). This means that photon scattering from the locking light is negligible for current experiments, and ideally will be reduced in future configurations.

It should also be noted that this estimate of the shift is at odds with the 50 kHz figure presented in Refs. [25, 26], although the power used in experiments has not been intentionally changed and the power quoted in Ref. [25] (10 nW) does not account for the discrepancy, which seems to be due to an error in their calculations.

[1] The intensity is calculated assuming the transmission of the cavity mirrors is the same at 836 nm as it is at 852 nm. It is probably safe to assume that the true value is actually higher than this, yielding a smaller intensity. See Chapter 7 for details on calculating intracavity intensity and Stark shifts.

2.2.3 Diode laser for the FORT

The final step in configuring a stable system for trapping cesium atoms in our cavity is to introduce the FORT beam and stabilize its frequency with respect to the locked physics cavity. The FORT wavelength is $\lambda_F = 935.6$ nm, a full 83 nm away from λ_0. At this wavelength, the PC mirror coatings are far from optimal, and the cavity linewidth is about $2\kappa_F \approx 3.2$ GHz (FWHM). As a result of this very large linewidth, the FORT laser only needs to be stabilized within a frequency range much smaller than κ_F, which is trivially accomplished using a low-bandwidth integrator to the laser's grating. The FORT lock is by far the simplest of all the lasers on the table. This simplicity is a far cry from earlier generations of the experiment. Not only were we using a Ti:Sapphire for the FORT laser which had to be pre-stabilized on its own auxiliary narrow-linewidth cavity in order to suppress its large native frequency fluctuations, but we were also using cavity modes much closer to λ_0, making the locking requirements very stringent.

Sidebands at around 100 MHz are applied to the FORT beam using EOM2, the laser is tuned and locked to the frequency corresponding to triple resonance of the PC, and the system is then ready to go. Please see chapters 3 and 7 for further quantitative details of our FORT.

2.3 Photodetection and cavity outputs

2.3.1 Photon counting system

The incorporation of single-photon counting was one of the most critical changes to the experimental apparatus in recent years. Accomplished together with Joe Buck and Alex Kuzmich, our task was to acquire appropriate detectors for our system as well as the proper electronics for recording the data. In this section I will describe the system and discuss some important measurements of the detector properties.

The detectors used are the SPCM-AQR series avalanche photodiodes (APD's) from Perkin-Elmer. The specified quantum efficiency is about 50% at $\lambda_0 = 852$ nm, and our most recent measurement gave $(49 \pm 5)\%$. The fiber-coupled versions were purchased due to fairly severe space constraints on our optical table. Had we bought the free-space detectors, a very well shielded box would have had to be built around the detectors to block stray light, which would have been difficult to make room for. As shown in Fig. 2.2 the cavity output light is focused into one fiber launcher, and a fiber coupler is used as a beam splitter to send half the light to each of two APD's.

The output TTL pulses from the detectors are sent to a computer card that records the arrival time of each pulse. The card is the P7888 from Fast Comtec Gmbh, and has one start channel and four stop channels. The time resolution is 1 ns in two channel mode and 2 ns in four channel mode.

The main reason for using two detectors in photon counting experiments is dead time, where

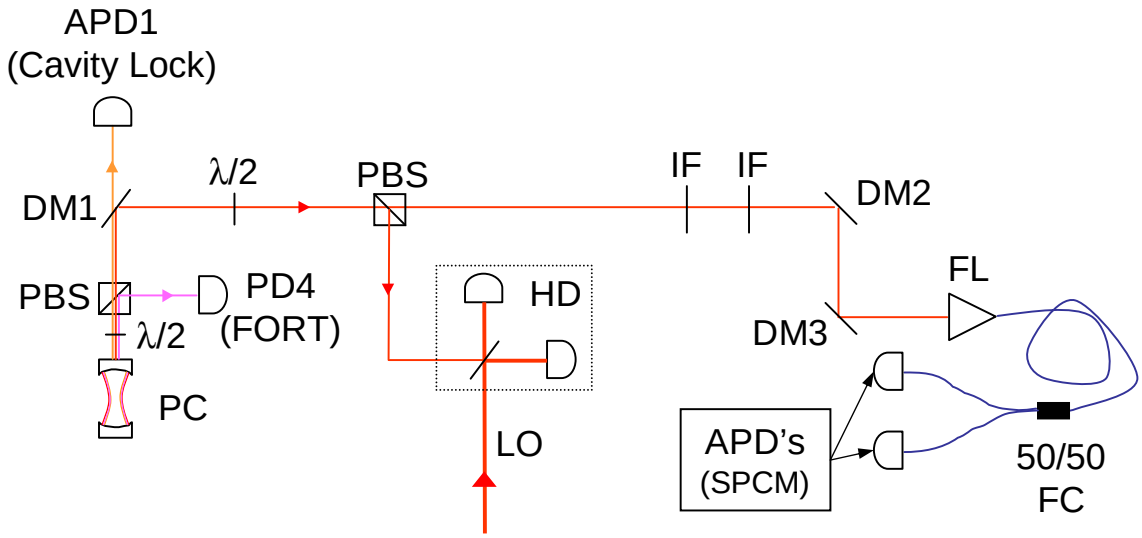

Figure 2.2: Diagram of the optical layout for the output side of the physics cavity. A polarizing beam splitter (PBS) at the cavity output sends some of the FORT light ($\lambda_F = 936$ nm) to photodetector PD4 (the half wave plate is optimized for $\lambda_0 = 852$ nm, resulting in residual FORT light continuing through the PBS). Dichroic mirror DM1 allows most of the locking light at $\lambda_L = 836$ nm to be transmitted to an avalanche photodiode (APD1). Another $\lambda/2$ and PBS combination allows the option of heterodyne detection (HD) or single-photon counting. The local oscillator for HD contains about 5 mW of power. Interference filters (IF) and additional dichroic mirrors (DM2,DM3) prevent remaining power at λ_L and λ_F from reaching the single-photon counting avalanche photodiodes APD's (SPCM). These APD's are fiber coupled, hence the fiber launcher (FL) and fiber coupler (50/50 FC) which acts as a 50/50 beamsplitter here.

after a photoelectric event the detector has a recovery time before it can detect the next photon. Another problem associated with these APD's is afterpulsing, where the detector puts out a spurious TTL pulse a short time after a legitimate event. These two effects are both evidenced in the data presented in Fig. 2.3. These are the results of an autocorrelation measurement, where the TTL output stream from an APD is split, and then sent to the start channel and stop channels of the card, respectively. The detector is illuminated continuously by a light emitting diode. The plotted quantity $A(\tau)$ is a histogram of the stop times relative to the start times.

The fact that $A(\tau) = 0$ for short times τ is a consequence of the dead time: the detector never emits two output pulses within some window τ_{DT}. Fig. 2.3(a) seems to suggest that $\tau_{DT} \approx 33$ ns, but this is not the case. As it turns out, the P7888 card has its own dead time of about 20 ns (independently measured), meaning stop pulses arriving within the first 20 ns of a start event are not recorded, and $\tau = 0$ occurs after this delay. Therefore the APD dead time $\tau_{DT} \approx 53$ ns (manufacturer specification 50 ns).

The next significant feature in Fig. 2.3 is the large number of events in the bins immediately following the end of the dead time ($\tau \approx 33$ ns). This is interpreted to be afterpulsing, since the statistics of the light source (LED) should be flat on this timescale. The small second bump at around

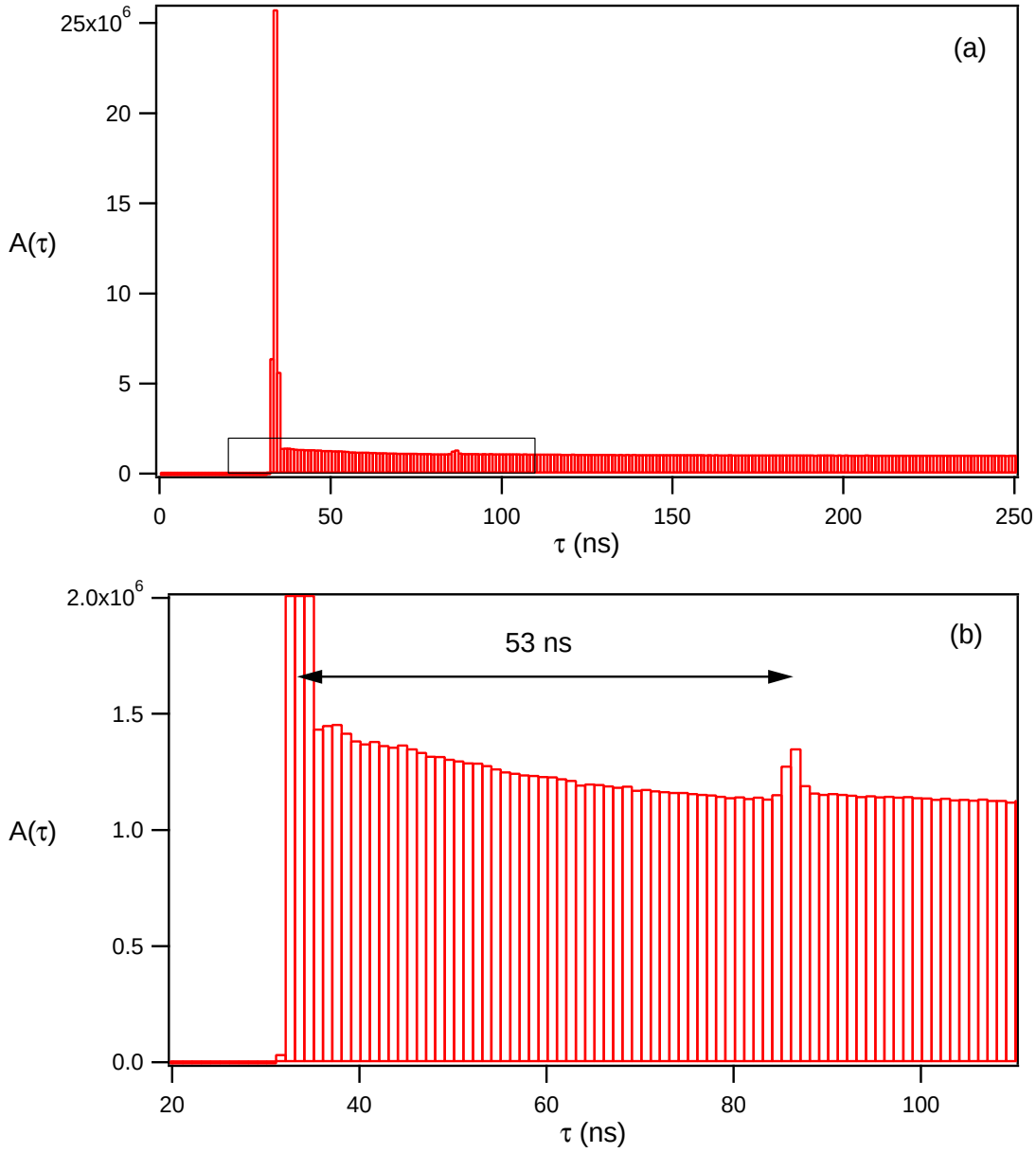

Figure 2.3: Histogram $A(\tau)$ of the time separation between photoelectric events at the same detector. The large spike at 33 ns results from afterpulsing. Panel (b) is a blowup of the boxed region of panel (a).

$\tau = 86$ ns is presumably from events with two consecutive afterpulses, and the time separation of the first and second spikes agrees with the dead time measurement of 53 ns. Counting the number of events in the large spike and dividing by the number of start events gives a good estimate of the afterpulse probability $P_{AP} = 1.2\%$. In addition, it is clear from Fig. 2.3(b) that $A(\tau)$ is not flat for small τ, meaning that some afterpulses may also occur at a distribution of delays which

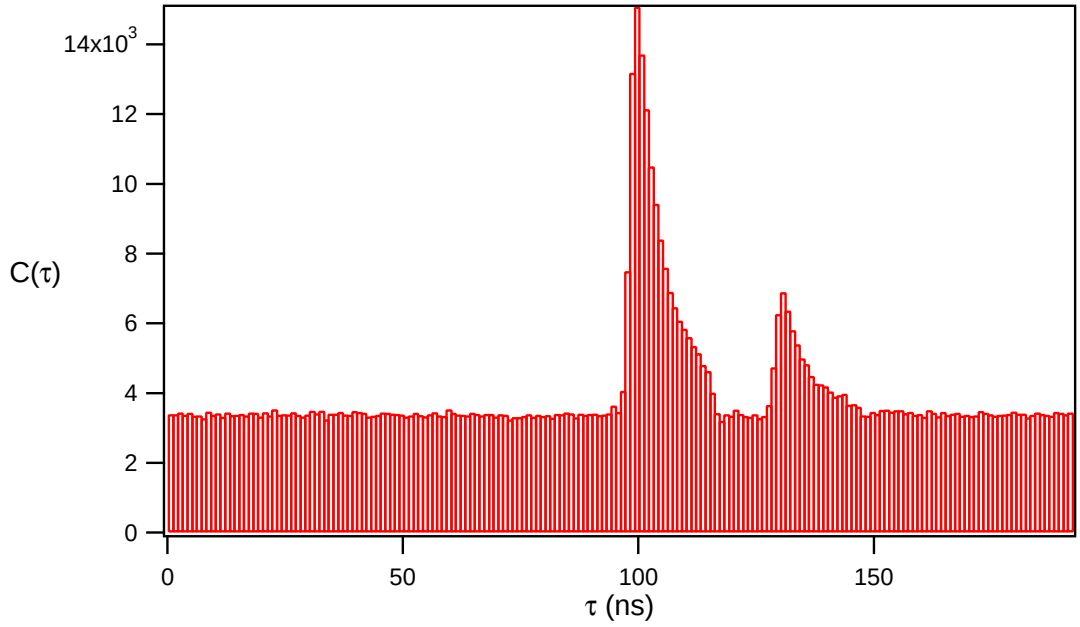

Figure 2.4: Cross-correlation $C(\tau)$ between the two APS's (histogram of time separations τ between events at the two detectors). The two large spikes come from light emitted by one detector reaching the other one. Presumably the two spikes correspond to back reflection from the faces of the two different input fibers to the fiber coupler, which each had different lengths. This problem was no longer measurable after we switched from multi-mode to single-mode fibers.

decays for large τ. It is possible to subtract the average value of $A(\tau)$ for times well beyond this decay (1.5 μs $< \tau <$ 2 μs) in order to quantify this effect. This calculation gives a total afterpulse probability of 2.0% (this includes the events in the spikes). Although this deviation from a flat $A(\tau)$ does not necessarily result from afterpulses, from this analysis it seems fairly certain that the afterpulse probability is between 1% and 2%. This is much higher than the manufacturer specification of 0.3% (typical).

The other effect to be discussed here is the light emission by the APD's during photon detection. As stated in the documentation from Perkin-Elmer, "one peculiarity of silicon avalanche photodiodes is that as an incoming photon is detected a small amount of light is emitted from the avalanche region." We observed this effect when using multimode fibers for this detection system. The light flashed by one detector propagated along the fiber, reflected off the other end, and was detected by the other detector. As shown in Fig. 2.4, these events created large spikes in the cross-correlation data $C(\tau)$ between the two detectors (one detector output was sent to the start channel of the P7888 and the other to a stop channel). I will not describe this in further detail since our more recent experiments have all been done with single-mode fiber, and we can no longer see this effect. Presumably this light from the APD's couples into the much smaller single mode fibers with much lower efficiency, so that we are no longer sensitive to it.

2.3.2 Heterodyne detection

Since most of our recent experiments and plans for the near future involve photon counting, I will not describe the heterodyne detection (HD, Fig. 2.2) system in great detail. In addition, the actual detectors, RF components, local oscillator (LO) cavity and optical path are almost identical today to their status in Ref. [25].

Two small points are in order though. One of several factors that impeded our progress in trap lifetime was stray light from the LO reaching the physics cavity, apparently causing heating of the atomic motion. At this time, the LO frequency was 40 MHz blue of the Cs $4 \rightarrow 5'$ resonance, and blue detuning is largely associated with heating [47, 48]. At first we solved this problem by blocking the LO with a mechanical shutter during the trapping interval and only re-opening it for final detection. Since then, we have changed this detuning to 125.5 MHz to the red (halfway between $4 \rightarrow 4'$ and $4 \rightarrow 5'$) and this problem seems to be alleviated to a large extent (see, e.g., the storage times of Ref. [33]/Chapter 4 in the presence of the LO). Although I do not have quantitative details of the heating rate associated with this LO, anyone trying to use heterodyne detection for cavity QED should be aware of this problem.

I also wanted to include the most recent measurement of the homodyne fringe visibility associated with the HD. The beam size of the cavity output field was changed for the work of Ref. [36], so the LO beam had to be adjusted as well. The mode-matching was optimized in a fairly casual manner since it is only being used for diagnostic purposes these days, giving a new fringe visibility of about 74% (compared to 88% quoted in Ref. [25]).

2.4 Lasers and metrology for cooling and trapping

As shown in Fig. 2.5, two additional diode lasers are needed for the magneto-optical traps (MOTs). One laser supplies the cooling light at $F = 4 \rightarrow 5'$, and the other is a repumper resonant with $F = 3 \rightarrow 3'$ [47].

The laser used for the MOT cooling light is actually an injection-locked slave diode, where the injection light is taken from the CQED laser. This is a very convenient technique because the diode system does not need a grating-based external cavity and the "lock" consists only of optical alignment of the injection light into the slave diode. An additional advantage is that the optical lock is very broadly tunable, i.e., the injection light can be shifted by hundreds of MHz and the lock is maintained, with little to no change in the slave output power. This means that one can put a double-passed AOM in the master path (without stringent efficiency requirements) for frequency shifting. The slave then only needs one single-pass AOM (which can always be operated at the optimal frequency for diffraction efficiency) for switching the MOT light on and off.

The slave power is divided into three paths, one for the upper MOT (UMOT), one for the lower

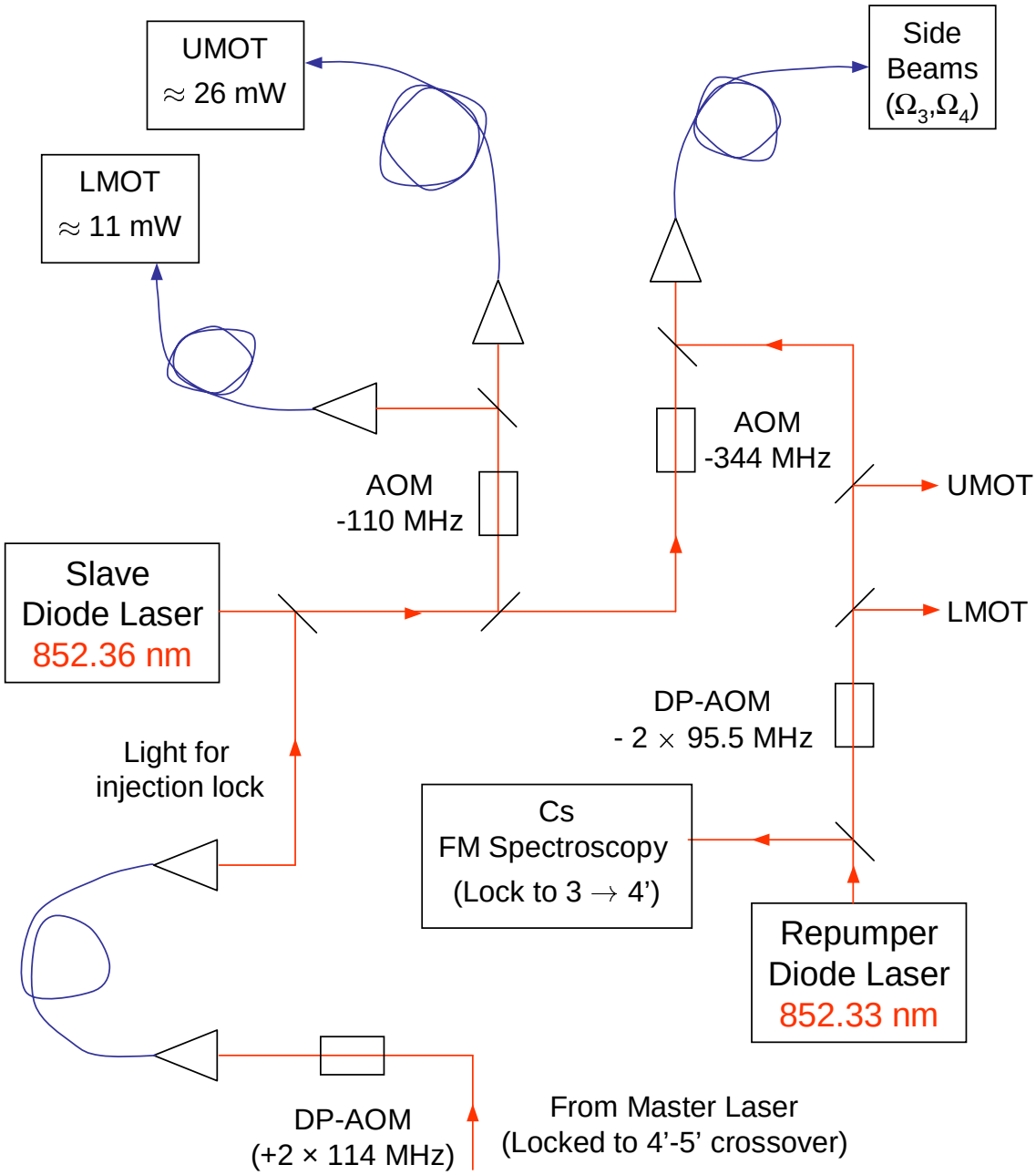

Figure 2.5: Diagram of the optical layout for laser cooling and trapping. Frequency shifting is done using acousto-optic modulators (AOM), some of which are double-passed (DP-AOM). Both repumping and cooling light are sent to the upper MOT (UMOT) and lower MOT (LMOT). All AOM frequencies are tunable and most are regularly switched during experiments. The frequencies shown for the side beams are such that Ω_4 is detuned by +17 MHz from the $4 \rightarrow 4'$ transition, and Ω_3 is detuned by +10 MHz from $3 \rightarrow 3'$.

MOT (LMOT) and one for the transverse beams (denoted Ω_4). Each of those are delivered to the vacuum chamber via single-mode fibers. The frequency configuration depicted in Fig. 2.5 has the Ω_4 beam near the $F = 4 \rightarrow 4'$ resonance.

It is worth mentioning that this part of the apparatus has been greatly simplified in recent years, relative to what was originally set up for Refs. [25, 26]. For those early experiments, separate lasers were constructed for the two MOTs, both for trapping and repumping. In all likelihood, this was done because the exact power requirements were not known before the system was constructed, so they erred on the side of more lasers. Since a completely independent master-slave configuration was implemented for the upper MOT trapping light, this amounted to a total of five diode lasers for the cooling and trapping part of the experiment alone. It was clearly a good investment of time and effort to reconfigure this region of the table, thereby effectively reducing the laser number from five to two. Keeping a large number of home-built laser systems well-behaved on a day-to-day basis ended up consuming large amounts of time, at the expense of making progress in the experiments.

Chapter 3

State-Insensitive Cooling and Trapping of Single Atoms in an Optical Cavity

This chapter is organized as follows. Section 3.1 is reproduced from Ref. [27]. The subsequent sections contain additional data and analysis pertaining to our efforts to trap single atoms in the cavity.

3.1 Main results

A long-standing ambition in the field of cavity quantum electrodynamics (QED) has been to trap single atoms inside high-Q cavities in a regime of strong coupling [20]. Diverse avenues have been pursued for creating the trapping potential for atom confinement, including additional far off-resonant trapping beams [26, 25], near-resonant light with with $\bar{n} \simeq 1$ intracavity photons [24, 49, 50], and single trapped ions in high-finesse optical cavities [30, 29], although strong coupling has yet to be achieved for trapped ions. A critical aspect of this research is the development of techniques for atom localization that are compatible with strong coupling, as required for quantum computation and communication [51, 21, 52, 53, 54, 37].

Here we present experiments to enable quantum information processing in cavity QED by (1) achieving extended trapping times for single atoms in a cavity while still maintaining strong coupling, (2) realizing a trapping potential for the center-of-mass motion that is largely independent of the internal atomic state, and (3) demonstrating a scheme that allows continuous observation of trapped atoms by way of the atom-field coupling. More specifically, we have recorded trapping times up to 3 s for single Cs atoms stored in an intracavity far-off resonance trap (FORT) [47], which represents an improvement by a factor of 10^2 beyond the first realization of trapping in cavity QED [26, 25], and by roughly 10^4 beyond prior results for atomic trapping [24, 49] and localization [50] with $\bar{n} \simeq 1$ photon. We have also continuously monitored trapped atoms by way of strong coupling to a probe

beam, including observations of trap loss atom by atom over intervals $\simeq 1$ s. These measurements incorporate auxiliary cooling beams, and provide the first realization of cooling for trapped atoms strongly coupled to a cavity. Our protocols are facilitated by the choice of a "magic" wavelength for the FORT [55, 56, 57, 48], for which the relevant atomic levels are shifted almost equally, thereby providing significant advantages for coherent state manipulation of the atom-cavity system.

A major obstacle to the integration of a conventional red-detuned FORT within the setting of cavity QED is that excited electronic states generally experience a positive AC-Stark shift of comparable magnitude to the negative (trapping) shift of the ground state [47]. This leads to the unfortunate consequence that the detuning and hence the effective coupling between an atomic transition and the cavity mode become strong functions of the atom's position within the trap [48]. However, due to the specific multi-level structure of Cesium, the wavelength λ_F of the trapping laser can be tuned to a region where both of these problems are eliminated for the $6S_{1/2} \rightarrow 6P_{3/2}$ transition, as illustrated in Fig. 3.1 [55, 56, 57, 48]. Around the "magic" wavelength $\lambda_F = 935$ nm, the sum of AC-Stark shifts coming from different allowed optical transitions results in the ground $6S_{1/2}$ and excited $6P_{3/2}$ states both being shifted downwards by comparable amounts, $\delta_{6S_{1/2}} \simeq \delta_{6P_{3/2}}$, albeit with small dependence on $(F', m_{F'})$ for the shifts $\delta_{6P_{3/2}}$.

The task then is to achieve state-independent trapping while still maintaining strong coupling for the $6S_{1/2} \rightarrow 6P_{3/2}$ transition. Our experimental setup to achieve this end is schematically depicted in Fig. 3.2 [26, 25]. Significantly, the cavity has a TEM_{00} longitudinal mode located nine mode orders below the mode employed for cavity QED at 852 nm, at the wavelength $\bar{\lambda}_F = 935.6$ nm, allowing the implementation of a FORT with $\delta_{6S_{1/2}} \simeq \delta_{6P_{3/2}}$. The field to excite this cavity mode is provided by a laser at $\bar{\lambda}_F$, which is independently locked to the cavity. The finesse of the cavity at $\bar{\lambda}_F$ is $\mathcal{F} \sim 2200$ [59], so that a mode-matched input power of 1.2 mW gives a peak AC-Stark shift $\delta_{6S_{1/2}}/2\pi = -47$ MHz for all states in the $6S_{1/2}$ ground manifold, corresponding to a trap depth $U_0/k_B = 2.3$ mK, which was used for all experiments.

Principal parameters relevant to cavity QED with the system in Fig. 3.2 are the Rabi frequency $2g_0$ for a single quantum of excitation and the amplitude decay rates (κ, γ) due to cavity losses and atomic spontaneous emission. For our system, $g_0/2\pi = 24$ MHz, $\kappa/2\pi = 4.2$ MHz, and $\gamma/2\pi = 2.6$ MHz, where g_0 is for the $(6S_{1/2}, F = 4, m_F = 4) \rightarrow (6P_{3/2}, F' = 5, m'_F = 4)$ transition in atomic Cs at $\lambda_0 = 852.4$ nm. Strong coupling is thereby achieved ($g_0 \gg (\kappa, \gamma)$), resulting in critical photon and atom numbers $n_0 \equiv \gamma^2/(2g_0^2) \simeq 0.006$, $N_0 \equiv 2\kappa\gamma/g_0^2 \simeq 0.04$. The small transition shifts for our FORT mean that g_0 is considerably larger than the spatially dependent shift δ_0 of the bare atomic frequency employed for cavity QED, $g_0 \gg \delta_0 \equiv |\delta_{6P_{3/2}} - \delta_{6S_{1/2}}|$, whereas in a conventional FORT, $\delta_0 \sim 2|\delta_{6S_{1/2}}| \gg g_0$.

In addition to the FORT field, the input to the cavity consists of probe and locking beams, all of which are directed to separate detectors at the output. The transmitted probe beam is monitored

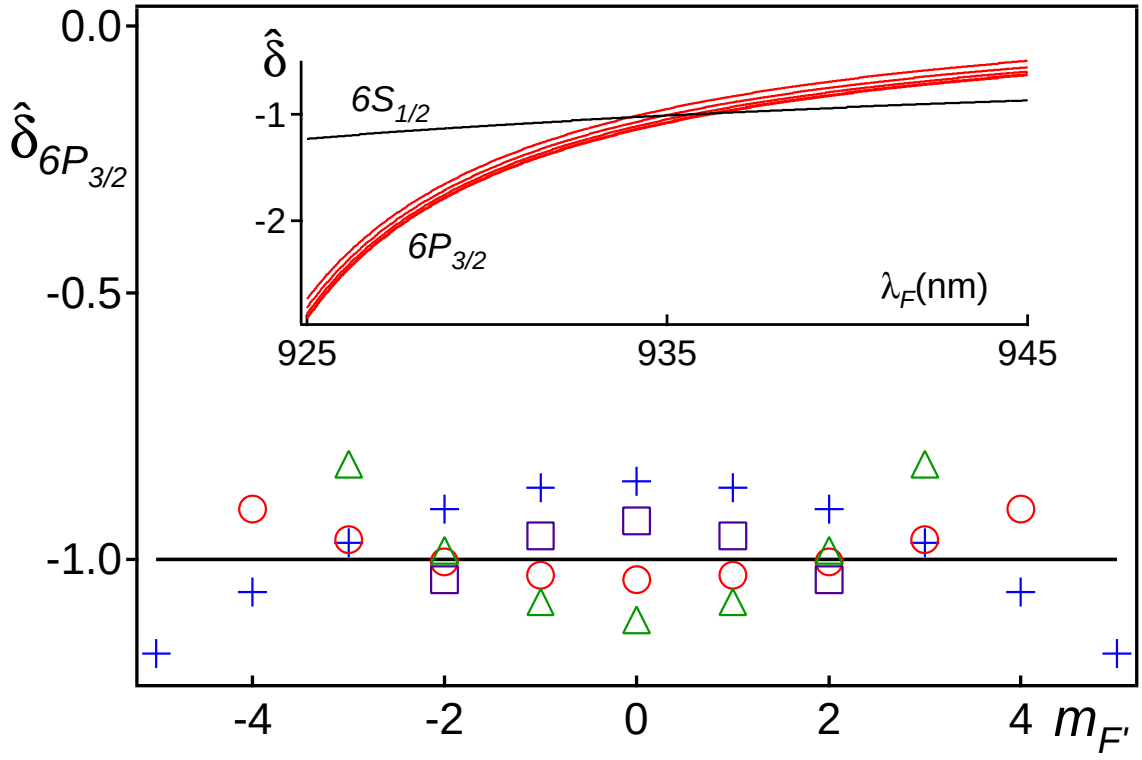

Figure 3.1: AC-Stark shifts $(\hat{\delta}_{6S_{1/2}}, \hat{\delta}_{6P_{3/2}})$ for the $(6S_{1/2}, 6P_{3/2})$ levels in atomic Cs for a linearly polarized FORT. The inset shows $(\hat{\delta}_{6S_{1/2}}, \hat{\delta}_{6P_{3/2},F'=4})$ as functions of FORT wavelength λ_F. The full plot gives $\hat{\delta}_{6P_{3/2}}$ versus $m_{F'}$ for each of the levels $6P_{3/2}, F' = 2, 3, 4, 5$ for $\lambda_F = 935.6$ nm. In each case, the normalization is $\hat{\delta} = \delta/[\delta_{6S_{1/2}}(\lambda_F = 935.6 \text{ nm})]$. The shifts shown here incorporate the following couplings, including counter-rotating terms: $6S_{1/2} \rightarrow nP_{1/2,3/2}$, for $n = 6 - 11$; $6P_{3/2} \rightarrow nS_{1/2}$ for $n = 6 - 15$; $6P_{3/2} \rightarrow nD_{3/2,5/2}$ for $n = 5 - 11$. Relevant parameters are taken from Refs. [40, 58] (see Chapter 7 for more details).

using heterodyne detection, allowing real-time detection of individual cold atoms within the cavity mode [60]. The cavity length is actively controlled using a cavity resonance at $\lambda_C = 835.8$ nm, so the length is stabilized and tunable independently of all other intracavity fields [26, 25]. The probe as well as the FORT beam are linearly polarized along a direction $\hat{l}_+$ orthogonal to the x-axis of the cavity [59].[1]

Cold atoms are collected in a magneto-optical trap (MOT) roughly 5 mm above the cavity mirrors and then released after a stage of sub-Doppler polarization-gradient cooling [47]. Freely falling atoms arrive at the cavity mode over an interval of about 10 ms, with kinetic energy $E_K/k_B \simeq 0.8$ mK, velocity $v \simeq 0.30$ m/s, and transit time $\Delta t = 2w_0/v \simeq 150$ μs. Two additional orthogonal pairs of counter-propagating beams in a $\sigma^+ - \sigma^-$ configuration illuminate the region between the cavity mirrors along directions at $\pm 45°$ relative to $\hat{y}, \hat{z}$ (the "$y - z$ beams") and contain cooling light tuned

[1] Because of small stress-induced birefringence in the cavity mirrors, we align the directions of linear polarization along an axis that coincides with one of the cavity eigen-polarizations [59], denoted by $\hat{l}_\pm$. For initial polarization along $\hat{l}_+$, measurements of FORT [probe] polarization along $\hat{l}_-$ for the cavity output power P give $P_-/P_+ < 0.02[0.002]$ for the FORT [probe] beam.

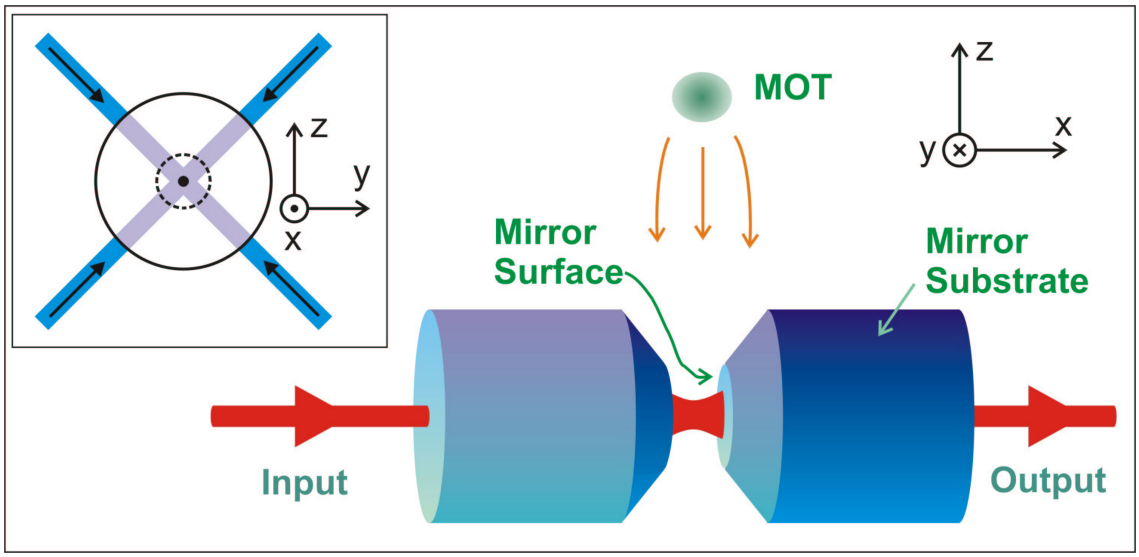

Figure 3.2: Schematic of experiment for trapping single atoms in an optical cavity in a regime of strong coupling. Relevant cavity parameters are length $l = 43.0\ \mu$m, waist $w_0 = 23.9\ \mu$m, and finesse $\mathcal{F} = 4.2 \times 10^5$ at 852 nm. The inset illustrates transverse beams used for cooling and repumping.

red of $F = 4 \rightarrow F' = 5$ and repumping light near the $F = 3 \rightarrow F' = 3$ transition[2]. These beams eliminate the free-fall velocity to capture atoms in the FORT and provide for subsequent cooling of trapped atoms.

We employed two distinct protocols to study the lifetime for single trapped atoms in our FORT.

(1) *Trapping "in the dark"* with the atom illuminated only by the FORT laser at $\bar{\lambda}_F$ and the cavity-locking laser at λ_C. For this protocol, strong coupling enables real-time monitoring of single atoms within the cavity for initial triggering of cooling light and for final detection.

(2) *Trapping with continuous observation of single atoms* with cavity probe and cooling light during the trapping interval. In this case, atoms in the cavity mode are monitored by way of the cavity probe beam, with cooling provided by the auxiliary $y - z$ beams.

(1) In our first protocol, the $F = 4 \rightarrow F' = 5$ transition is strongly coupled to the cavity field, with zero detuning of the cavity from the bare atomic resonance, $\Delta_C \equiv \omega_C - \omega_{4\rightarrow 5} = 0$. In contrast to Ref. [26, 25], here the FORT is *ON* continuously without switching, which makes a cooling mechanism necessary to load atoms into the trap. The initial detection of a single atom falling into the cavity mode is performed with the probe beam tuned to the lower sideband of the vacuum-Rabi spectrum ($\Delta_p = \omega_p - \omega_{4\rightarrow 5} = -2\pi \times 20$ MHz). The resulting *increase* in transmitted probe power when an atom approaches a region of optimal coupling[3] triggers *ON* a pulse of transverse cooling light from the $y - z$ beams, detuned 41 MHz red of $\omega_{4\rightarrow 5}$. During the subsequent trapping interval,

[2]The (incoherent) sum of the four intensities is $I_{4-5} \sim 60\text{mW/cm}^2$ for the cooling and $I_{3-3} \sim 40\text{mW/cm}^2$ for the repumping light, with uncertainties of roughly $2\times$.

[3]Specific examples of single-atom detection events are omitted here. For $\Delta_p \simeq -g_0$, the increases in cavity transmission are quite similar to those in Refs. [24, 61], while for $\Delta_p = 0$, the decreases are similar to those in Refs. [26, 60], albeit now in the presence of the FORT.

all near-resonant fields are turned *OFF* (including the transverse cooling light). After a variable delay t_T, the probe field is switched back *ON* to detect whether the atom is still trapped, now with $\Delta_p = 0$.

Data collected in this manner are shown in Fig. 3.3(a), which displays the conditional probability P to detect an atom given an initial single-atom triggering event versus the time delay t_T. The two data sets shown in Fig. 3.3(a) yield comparable lifetimes, the upper acquired with mean intracavity atom number $\bar{N} = 0.30$ atoms and the lower with $\bar{N} = 0.019$.[4] The offset in P between these two curves arises primarily from a reduction in duration δt of the cooling pulses, from 100 μs to 5 μs, which results in a reduced capture probability. Measurements with constant δt but with $\bar{N}$ varied by adjusting the MOT parameters allow us to investigate the probability of trapping an atom other than the "trigger" atom and of capturing more than one atom. For example, with $\delta t = 5$ μs as in the lower set, we have varied $0.011 \lesssim \bar{N} \lesssim 0.20$ with no observable change in either P_T or the trap lifetime τ. Since a conservative upper bound on the relative probability of trapping a second atom is just $\bar{N}/2$ (when $\bar{N} \ll 1$), these data strongly support the conclusion that our measurements are for single trapped atoms. We routinely observe lifetimes 2 s $< \tau <$ 3 s depending upon the parameters chosen for trap loading and cooling.

Fig. 3.3(b) explores scattering processes within the FORT that transfer population between the $6S_{1/2}, F = (3, 4)$ ground-state hyperfine levels. For these measurements, the $F = 4$ level is initially depleted, and then the population in $F = 4$ as well as the total $3 + 4$ population are monitored as functions of time t_D to yield the fractional population $f_4(t_D)$ in $F = 4$. The measured time $\tau_R = (0.11 \pm 0.02)$s for re-equilibration of populations between $F = (3, 4)$ agrees with a numerical simulation based upon scattering rates in our FORT, which predicts $\tau_R = 0.10$ s for atoms trapped at the peak FORT intensity in an initially unpolarized state in the $F = 3$ level.

Turning next to the question of the mechanisms that limit our FORT lifetime, we recall that parametric heating caused by intensity fluctuations of the trapping field can be quite important [26, 25, 62, 63]. From measurements of intensity fluctuations for our FORT around twice the relevant harmonic frequencies ($\nu_{axial} = 570, \nu_{radial} = 4.8$) kHz, we estimate a lower bound to the FORT lifetime of $\tau_p^{axial} > 1.6$ s.[5] Since this estimate suggests that parametric heating could be a limiting factor in Fig. 3.3, we performed subsequent measurements in which the intensity noise was reduced below the shot-noise level of our detection system, giving a lower bound $\tau_p^{axial} > 9$ s. Unfortunately, the measured FORT lifetime increased only modestly to $\tau = (3.1 \pm 0.4)$ s, indicating that other mechanisms are partially responsible for the observed decay.

A second suspect is a heating process described by Corwin *et al.* [64] associated with inelastic Raman scattering in a slightly elliptically polarized FORT field (due to the aforementioned small

[4] $\bar{N}$ is estimated from the mean number of atom transit events (of duration $\simeq 150\mu$s) during the interval $\simeq$ 10ms from the falling MOT atoms, in the absence of trapping.

[5] The predicted $\tau_p^{radial} > 10^4$ s.

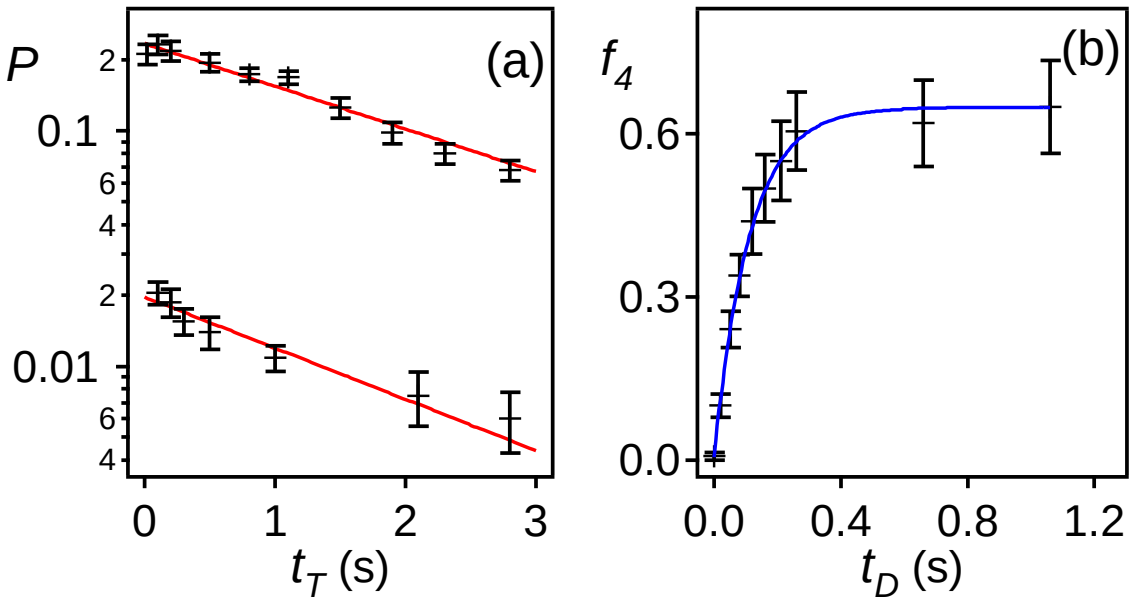

Figure 3.3: (a) Detection probability P as a function of trapping time t_T. The upper data set is for mean intracavity atom number $\bar{N} \approx 0.30$, while the lower set is for $\bar{N} \approx 0.019$ atoms. Exponential fits (solid lines) yield lifetimes $\tau_{\rm upper} = (2.4 \pm 0.2)$ s and $\tau_{\rm lower} = (2.0 \pm 0.3)$ s. (b) The fractional population $f_4(t_D)$ in $F = 4$ following depletion of this level at $t_D = 0$. An exponential fit (solid line) gives $\tau_R = (0.11 \pm 0.02)$ s.

birefringence). We calculate rates Γ_s for spontaneous Raman scattering in our FORT to be 2.5 to 7 s^{-1} for transitions that change the hyperfine quantum number F, and between 0.8 and 2.5 s^{-1} when only m_F changes [65]. Based on Eq. 3 in Ref. [64] (a two-state model), we estimate an upper limit to the heating rate from this mechanism, $\Gamma_{IR} \lesssim 0.2\Gamma_s$, giving heating times as short as 0.7 s for the fastest calculated scattering rate. However, we have also undertaken a full multilevel simulation of the optical pumping processes, which indicates much slower heating, $\Gamma_{IR} \sim 0.02$ s^{-1}. We are working to resolve this discrepancy.

A third suspect that cannot be discounted is the presence of stray light, which we have endeavored to eliminate. For lifetimes as in Fig. 3.3, we require intracavity photon number $\bar{n} \ll 10^{-5}$, which is not trivial to diagnose. A final concern is the background pressure in the region of the FORT. Although the chamber pressure is 3×10^{-10} Torr (leading to $\tau \simeq 30$ s), we have no direct measurement of the residual gas density in the narrow cylinder between the mirror substrates (diameter 1 mm and length 43 μm), except for the trap lifetime itself.

(2) Toward the goals of continuous observation of single trapped atoms [24, 49, 50] and of implementing Λ-schemes in cavity QED [51, 21, 52, 66], we next present results from our second protocol. Here, the $F = 4 \rightarrow F' = 4$ transition is strongly coupled to the cavity field, with $\Delta'_C \equiv \omega_C - \omega_{4\rightarrow4} = 0$. In contrast to our protocol **(1)**, the FORT and the transverse $y - z$ beams are left *ON* continuously, with the latter containing only light near the $F = 3 \rightarrow F' = 3$

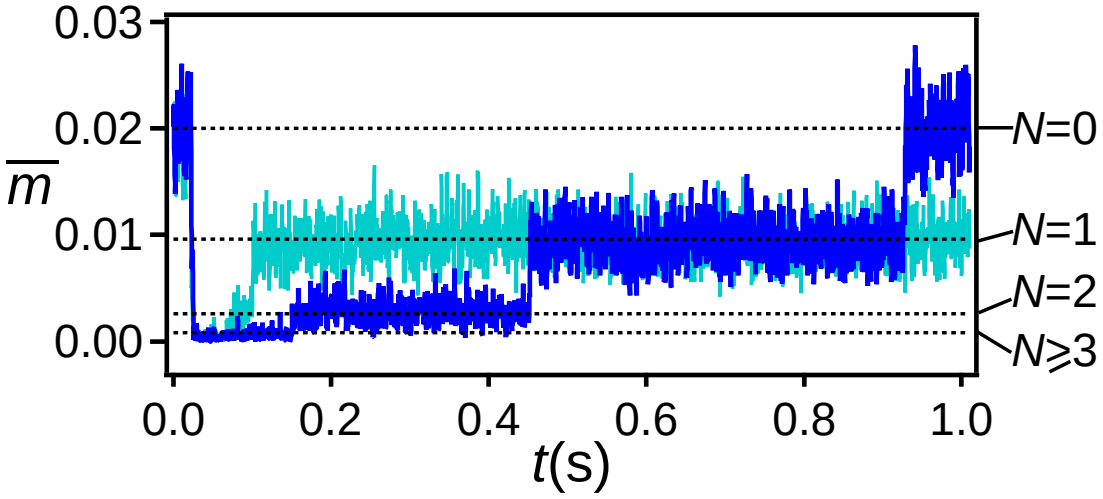

Figure 3.4: Two traces of the continuous observation of trapped atoms inside a cavity in a regime of strong coupling. After an initial sharp reduction around $t = 0$ as atoms are cooled into the cavity mode, the intracavity field strength $\bar{m}$ increases in a discontinuous fashion as trapped atoms escape from the cavity mode one by one. RF detection bandwidth = 1 kHz, $\Delta'_C = 0 = \Delta'_p$, and $\Delta_3/2\pi = 25$ MHz (*blue*).

resonance, with detuning Δ_3. Significantly, we observe trap loading with *no cooling light near the* $F = 4 \rightarrow F' = 5$ *transition.*

An example of the resulting probe transmission is shown in Fig. 3.4, which displays two separate records of the continuous observation of trapped atoms. Here, the probe detuning $\Delta'_p = \omega_p - \omega_{4\rightarrow 4} = 0$ and the probe strength is given in terms of $\bar{m} = |\langle \hat{a} \rangle|^2$ deduced from the heterodyne current, with $\hat{a}$ as the annihilation operator for the intracavity field. We believe that the $y - z$ repumping beams (which excite $F = 3 \rightarrow F' = 3$) provide cooling, since without them the atoms would "roll" in and out of the near-conservative FORT potential (indeed no trapping occurs in their absence). In addition, this is a continuous cooling and loading scheme, so that we routinely load multiple atoms into the trap.

The most striking characteristic of the data collected in this manner is that $\bar{m}$ versus t always reaches its deepest level within the $\simeq 10$ ms window when the falling atoms arrive, subsequently increasing in a discontinuous "staircase" of steps. As indicated in Fig. 3.4, our interpretation is that there is a different level for $\bar{m}$ associated with each value N of the number of trapped atoms (with the level decreasing for higher N), and that each step is due to the loss of an atom from the cavity mode. In addition, we observe a strong dependence both of the initial trapping probability and of the continuous observation time on the detuning of the transverse beams, with an optimal value $\Delta_3 \simeq 25$ MHz to the *blue* of the $3 \rightarrow 3$ transition, which strongly suggests blue Sisyphus cooling [67].

We stress that observations as in Fig. 3.4 are made possible by strong coupling in cavity QED,

for which individual intracavity atoms cause the displayed changes in probe transmission. While $\bar{m}$ in Figure 4 is only $\simeq 0.01$, it represents an output flux $\simeq 5 \times 10^5$ photons per second. The probe is also critical to the cooling, although it is not clear whether this beam is acting as a simple "repumper" [67] or is functioning in a more complex fashion due to strong coupling. We have not seen such striking phenomena under similar conditions for cavity QED with the $F = 4 \rightarrow F' = 5$ transition. Note that our ability to monitor the atom as well as to cool its motion are enabled by the state-insensitive character of the trap, since the net transition shifts are small, $(g_0, \Delta_3) \gg \delta_0$.

In summary, we have demonstrated a new set of ideas within the setting of cavity QED, including state insensitive trapping suitable for strong coupling. Trapping of single atoms with $g_0 \gg (\delta_0, \kappa, \gamma)$ has been achieved with lifetimes $\tau \simeq 2 - 3$ s. Since intrinsic heating in the FORT is quite low (~ 11 μK/s due to photon recoil), we anticipate extensions to much longer lifetimes. Continuous observations of multiple atoms in a cavity have been reported, and involve an interplay of a strongly coupled probe field for monitoring and a set of $y - z$ cooling beams. Our measurements represent the first demonstration of cooling for trapped atoms strongly coupled to a cavity. Beyond its critical role here, state insensitive trapping should allow the application of diverse laser cooling schemes, leading to atomic confinement in the Lamb-Dicke regime with strong coupling, and thereby to further advances in quantum information science.

3.2 Hyperfine relaxation

As documented in Fig. 3.3 of the previous section, we conducted measurements of the relaxation of the ground-state hyperfine levels due to spontaneous Raman scattering driven by the FORT field. These investigations were of interest since we were trying to characterize and understand the behavior of trapped atoms as much as possible. Since all these experiments are performed one atom at a time (for the most part), and inside a small cavity, the number of measurements and diagnostics available is very limited. The spin relaxation dynamics were accessible, however, due to the state-selective nature of the cavity QED interactions. This measurement also held particular interest with respect to our efforts to eliminate stray light from our experiment. Stray light in the cavity (at 852 nm) would drastically affect the results of such a measurement since optical pumping timescales from near-resonant light are very fast (of order 100 ns for a field of saturating intensity on resonance). The results we achieved are consistent with optical pumping calculations for the FORT only, presenting evidence that stray light was probably not causing a harmful amount of spontaneous emission (at least relative to the FORT).

In this section I will present some details about the procedure for these measurements, some additional data, and some calculations of the relevant scattering rates.

The basic protocol for the experiment (Fig. 3.5) is to deplete the $F = 4$ ground state a small fixed delay after trap loading, and then do state-sensitive detection after a variable delay. The optical pumping into $F = 3$ was accomplished using a pulse of our $F = 4 \rightarrow 5'$ cooling light in the absence of repumping light. Although it may have been more sensible to use another transition for this purpose (e.g., $4 \rightarrow 4'$), we did not have that frequency available yet in the lab at the time. In any case, the $4 \rightarrow 5'$ light was adequate for this depumping thanks to off-resonant excitation to the other hyperfine excited states.

The detection was done as usual using a resonant cavity probe ($4 \rightarrow 5'$ transition). However in this case the detection had to be sensitive not only to the atom's presence, but also to its hyperfine ground state. As shown in Fig. 3.5, this was accomplished by doing the detection in two phases, with the $3 \rightarrow 3'$ repumper not turned on until a fixed delay after the probe. The first 300 μs of the detection was then "blind" to any atoms still in $F = 3$, so the only signals seen in this window should be atoms that have undergone a spontaneous Raman transition from $F = 3$ to $F = 4$. Any atoms remaining in $F = 3$ were not detected until the repumper turn-on. The ratio of signals in the first 300 μs to the total number detected in the entire detection window was then interpreted as the fraction of atoms pumped into $F = 4$ by FORT-induced spontaneous Raman transitions.

Some data collected in this manner are presented in Fig. 3.6. Panel (a) contains the same data as Fig. 3.3(b), and we reproduce it here to emphasize the reproducibility of the measurement. Both experimental results are in good agreement with aforementioned calculations based on the

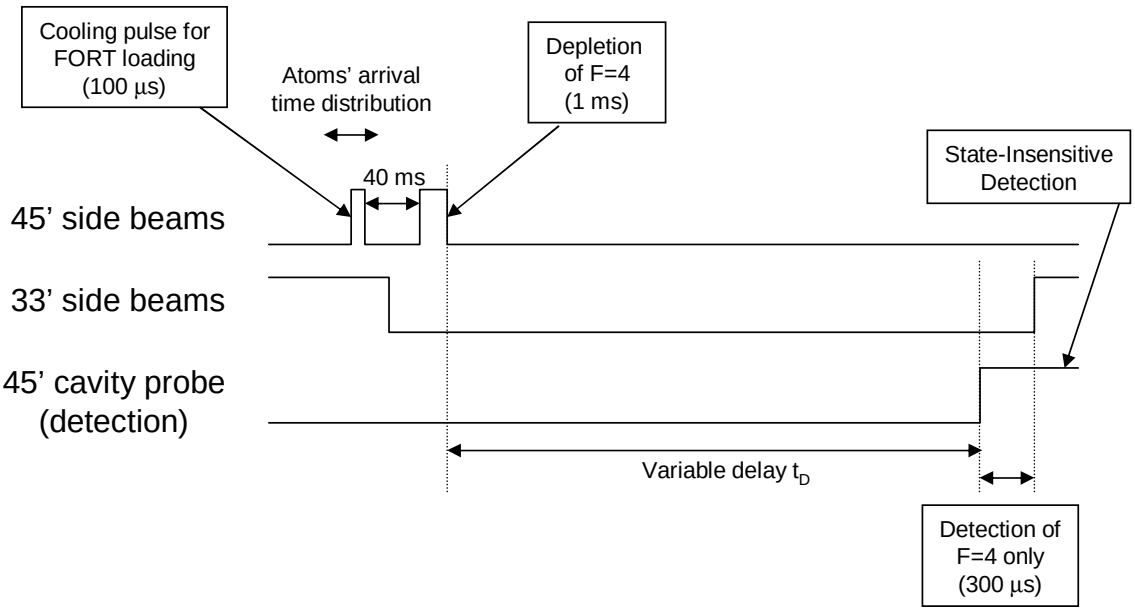

Figure 3.5: Timing diagram for spin relaxation measurements on trapped atoms in our FORT. For these measurements, mechanical shutters were used to ensure full extinction of beams.

spontaneous Raman scattering rates [27].

Although I will not discuss full simulations of optical pumping here, I now briefly present some formalism and results for the spontaneous Raman scattering rates. With these rates in hand, it is not difficult to calculate ground-state population dynamics in a FORT. The transition rate coupling state (F, m) to (F'', m'') is the following [65]:

$$\gamma_{Fm\rightarrow F''m''} = \frac{3\pi c^2 \omega_L^3 I}{2\hbar\mu^4} \left| \frac{\alpha^{(1/2)}_{Fm\rightarrow F''m''}}{\Delta_{1/2}} + \frac{\alpha^{(3/2)}_{Fm\rightarrow F''m''}}{\Delta_{3/2}} \right|^2 , \tag{3.1}$$

where I is the local FORT intensity, $\mu = \langle 44|d_{-1}|55\rangle$ is the dipole matrix element for the cycling transition, $\Delta_{J'} = \omega_L - \omega_{J'}$ and

$$\alpha^{(J')}_{Fm\rightarrow F''m''} = \frac{\Gamma_{J'}}{\omega^3_{J'}} \sum_{q,F',m'} \langle F''m''|d_q|F'm'\rangle\langle F'm'|\hat{\mathbf{d}}\cdot\vec{\varepsilon}_L|Fm\rangle. \tag{3.2}$$

Here, $\Gamma_{J'}$ is the spontaneous decay rate of the $6P_{J'}$ excited state. Please note that the $\hbar$ in the denominator of Equation 3.1 has been corrected from the seemingly erroneous h in Ref. [65]. Equation 3.1 is in agreement with simpler formulae presented elsewhere (see, e.g., Ref. [68]).

The calculation of dipole matrix elements is discussed in detail in Chapter 7. Here we simply present rates in tabular form for all pairs of states in the $6S_{1/2}$ ground manifold (Fig. 3.7). As has been discussed in detail elsewhere [65, 40], state-changing (Raman) transitions are suppressed relative to events where F and m stay the same (Rayleigh scattering). This is an interference effect

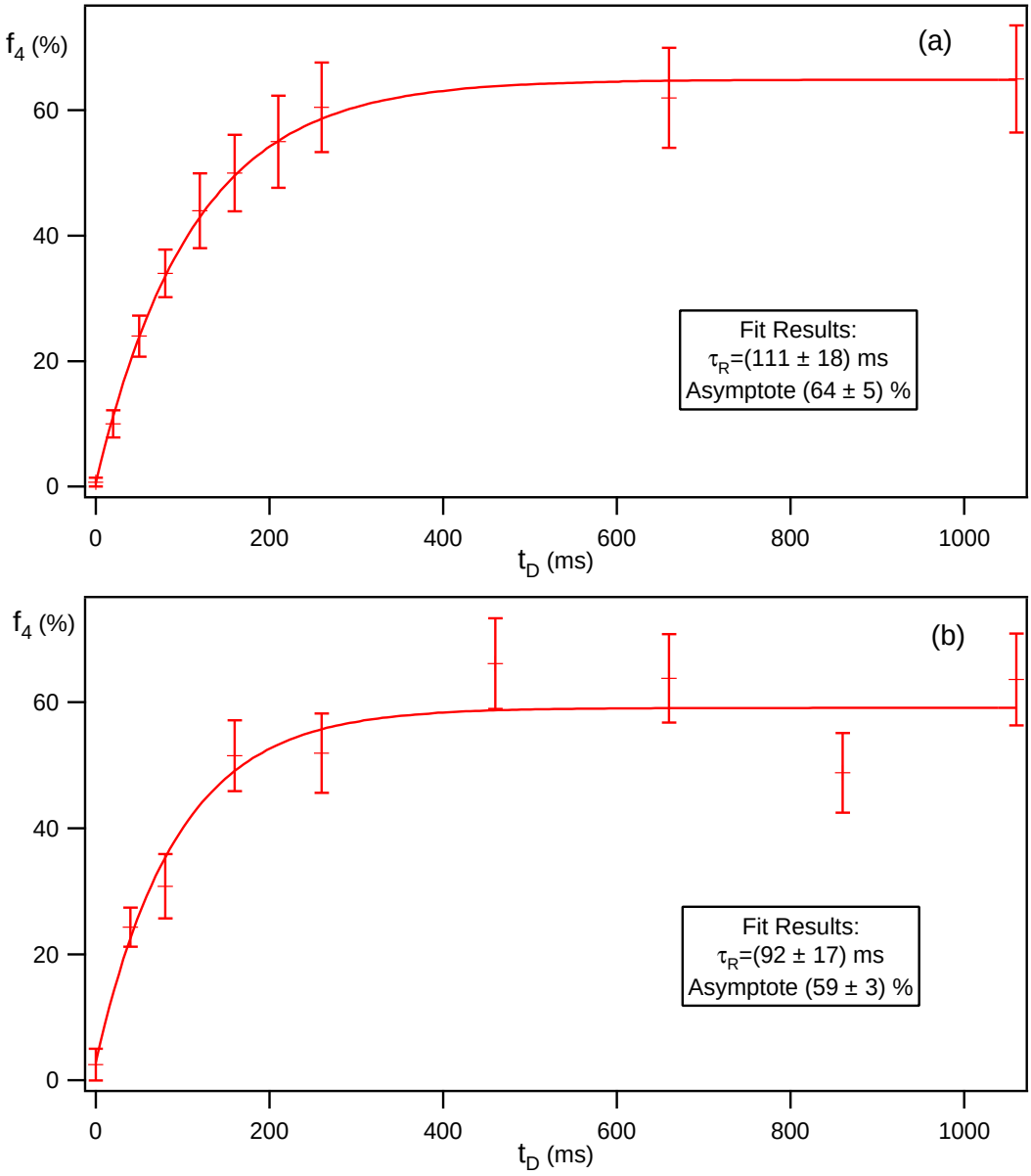

Figure 3.6: Fraction of atoms f_4 pumped into the $F = 4$ hyperfine ground state a delay t_D after that level is depleted. This pumping takes place due to spontaneous Raman scattering driven by the FORT field (timescales τ_R obtained from fits are in agreement with the theory). The expected asymptotic value of f_4 for $t_D \gg \tau_R$ from the theory is $9/16 \approx 56\%$ (see text). Two separate measurements are shown (taken about two weeks apart), with the data in panel (a) the same as plotted in Fig. 3.3(b). Error bars are obtained from basic Poissonian counting statistics based on the number of trials.

between scattering off the $D1$ and $D2$ lines, and the suppression is stronger the farther the FORT is detuned from the resonances.

Beyond these numerical values, it is instructive to point out some additional results of the

Final (4,m")

Initial (4,m)	4	3	2	1	0	-1	-2	-3	-4
4	44.31	0.88	0.00	0.00	0.00	0.00	0.00	0.00	0.00
3	0.88	44.31	1.54	0.00	0.00	0.00	0.00	0.00	0.00
2	0.00	1.54	44.31	1.98	0.00	0.00	0.00	0.00	0.00
1	0.00	0.00	1.98	44.31	2.20	0.00	0.00	0.00	0.00
0	0.00	0.00	0.00	2.20	44.31	2.20	0.00	0.00	0.00
-1	0.00	0.00	0.00	0.00	2.20	44.31	1.98	0.00	0.00
-2	0.00	0.00	0.00	0.00	0.00	1.98	44.31	1.54	0.00
-3	0.00	0.00	0.00	0.00	0.00	0.00	1.54	44.31	0.88
-4	0.00	0.00	0.00	0.00	0.00	0.00	0.00	0.88	44.31

Final (3,m")

Initial (4,m)	3	2	1	0	-1	-2	-3
4	6.16	0.00	0.00	0.00	0.00	0.00	0.00
3	0.00	4.62	0.00	0.00	0.00	0.00	0.00
2	0.22	0.00	3.30	0.00	0.00	0.00	0.00
1	0.00	0.66	0.00	2.20	0.00	0.00	0.00
0	0.00	0.00	1.32	0.00	1.32	0.00	0.00
-1	0.00	0.00	0.00	2.20	0.00	0.66	0.00
-2	0.00	0.00	0.00	0.00	3.30	0.00	0.22
-3	0.00	0.00	0.00	0.00	0.00	4.62	0.00
-4	0.00	0.00	0.00	0.00	0.00	0.00	6.16

Final (3,m")

Initial (3,m)	3	2	1	0	-1	-2	-3
3	44.31	0.66	0.00	0.00	0.00	0.00	0.00
2	0.66	44.31	1.10	0.00	0.00	0.00	0.00
1	0.00	1.10	44.31	1.32	0.00	0.00	0.00
0	0.00	0.00	1.32	44.31	1.32	0.00	0.00
-1	0.00	0.00	0.00	1.32	44.31	1.10	0.00
-2	0.00	0.00	0.00	0.00	1.10	44.31	0.66
-3	0.00	0.00	0.00	0.00	0.00	0.66	44.31

Final (4,m")

Initial (3,m)	4	3	2	1	0	-1	-2	-3	-4
3	6.16	0.00	0.22	0.00	0.00	0.00	0.00	0.00	0.00
2	0.00	4.62	0.00	0.66	0.00	0.00	0.00	0.00	0.00
1	0.00	0.00	3.30	0.00	1.32	0.00	0.00	0.00	0.00
0	0.00	0.00	0.00	2.20	0.00	2.20	0.00	0.00	0.00
-1	0.00	0.00	0.00	0.00	1.32	0.00	3.30	0.00	0.00
-2	0.00	0.00	0.00	0.00	0.00	0.66	0.00	4.62	0.00
-3	0.00	0.00	0.00	0.00	0.00	0.00	0.22	0.00	6.16

Figure 3.7: Scattering rates (s^{-1}) from initial states (F, m) to final states (F'', m'') calculated from Equation 3.1. The FORT wavelength is taken to be 935.6 nm and the intensity is $I = 2.92 \times 10^9$ W/m^2, corresponding to 1 mW of output power for our cavity parameters (FORT depth approximately 40 MHz).

calculations. By averaging these rates over the initial sublevel m and summing over the final states m'', it is possible to obtain total rates of population transfer $\gamma_{F \to F''}$ from F to F''. In general, this

rate $\gamma_{F\to F''} \propto (2F''+1)$ [10], and a simple rate equation model gives a steady-state value

$$f_F(t_D \to \infty) = \frac{\gamma_{F''\to F}}{\gamma_{F\to F''} + \gamma_{F''\to F}} = \frac{2F+1}{2F+1+2F''+1} \tag{3.3}$$

for the fraction of atoms in state F. In other words, the population ends up divided according to the degeneracy of the hyperfine level. For the case of Cs, as in Fig. 3.6, the fraction $f_4(t_D \to \infty) = 9/16$, in reasonable agreement with the data.

3.3 Intensity noise and parametric heating

3.3.1 FORT laser

One of the main possibilities we have investigated as the limit to our FORT lifetime has been parametric heating due to intensity fluctuations of the intracavity FORT field [26, 25, 62, 27, 28]. The purpose of this section is to document the most recent noise measurements on our 935.6 nm FORT. These measurements led to the claims in Ref. [27] that we have lowered the intensity noise below the shot noise limit of our detection system, and as a result the axial heating timescale from this mechanism is at least $\tau_p^{axial} > 9$ s.

The mechanism to be studied here is parametric heating due to fluctuations of the trap strength (or FORT intensity) at twice the relevant oscillation frequencies. This phenomenon is explained in detail in Ref. [62], and the main result is that the energy/temperature of a trapped atom increases exponentially with time constant

$$\tau_p = \frac{1}{\pi^2 \nu_{tr}^2 S(2\nu_{tr})}, \tag{3.4}$$

where $S(2\nu_{tr})$ is the one-sided power spectrum of the fractional intensity noise evaluated at $2\nu_{tr}$, and ν_{tr} is the harmonic trap frequency. In our case since we have an anisotropic trap with two oscillation frequencies ($\nu_{axial} = 570, \nu_{radial} = 4.8$) kHz, we must focus on two separate frequency ranges. In addition, it should be pointed out that the trap is anharmonic in both directions, and that the quoted frequencies ($\nu_{axial}, \nu_{radial}$) are the maximum values corresponding to small amplitude oscillations. Therefore the noise spectrum is important not only at the frequencies ($2\nu_{axial}, 2\nu_{radial}$), but also over a large range of frequencies below these values.

Figs. 3.8 and 3.9 give the most recent comprehensive set of noise measurements in the two frequency ranges of interest. Fig. 3.10 illustrates the measured dependence of the noise level on optical power. Since this scaling is linear, the measurement is likely to be shot noise limited [69]. This means that at high frequencies, we can only state that the true level of intensity fluctuations is bounded by the measured levels, hence the statement $\tau_p^{axial} > 9$ s.

3.3.2 Locking laser

Although the direct measurements of intensity noise on the FORT field suggest that parametric heating is probably not a contributing factor to the trap lifetime, there is a small contribution to the trapping potential from the locking laser that was not considered in the analysis above. As discussed in Section 2.2.2, the maximum Stark shift from the locking field is at most about 5% of the FORT depth. If there is intensity noise on the field at $\lambda_L = 836$ nm, parametric heating can also ensue. We have performed a measurement of this noise contribution, which is the subject of this section.

When calculating the heating rate arising from this noise, it is crucial to carefully consider the normalization, since the usual consideration of *fractional* intensity noise [62] no longer applies the same way. Clearly the total Stark shift (and hence trapping potential) is dominated by the FORT laser itself, therefore the fractional noise level on the locking laser needs to be scaled down appropriately using the ratio of Stark shifts.

More specifically, in the usual single frequency FORT situation, the heating rate $\tau_p^{-1} \propto S(2\nu_{tr})$ (Equation 3.4), and the fractional intensity noise $S(2\nu_{tr}) \propto 1/I_F^2$, where I_F is the FORT intensity. This intensity appears because the trap depth (total Stark shift) $U_F \propto I_F$. In the case of two lasers contributing to the total intensity, the fractional intensity noise on one laser only contributes to the extent that that laser creates a Stark shift (designated U_L in the case of our locking laser). Therefore in our case, when considering the contribution from the locking field at λ_L we must multiply the fractional noise spectrum $S_L(2\nu_{tr})$ (measured and calculated the usual way) by the ratio $\left(\frac{U_L}{U_F+U_L}\right)^2 \approx \left(\frac{U_L}{U_F}\right)^2$. As a result, the noise power on the locking light is now "normalized" using the total Stark shift $\approx U_F$, as required.

Figure 3.11 documents the measurements of the intensity noise at λ_L. Unfortunately there was very little power on the detector, so that the noise of interest was barely above the detector's noise floor. Even though we made a correction for this, the measurement is very noisy (see the corrected trace in Fig. 3.11(c)) and the results should only be considered a rudimentary estimate of the contribution to atomic heating. More specifically, the electronic noise level in Fig. 3.11(a) rises higher than the total noise at some frequencies, causing the corrected level to become negative. This causes the huge (artificial) dips in the corrected lifetime trace of Fig. 3.11(c). With this issue taken into account, the results indicate that the axial heating from this effect probably leads to heating on a timescale > 10 s. However some of the spikes in the total (uncorrected) measured noise power dip below the 10 s level. This is a large enough contribution that this effect should be not be forgotten or neglected in future endeavors.

It should be noted that the simple treatment above completely neglects the different spatial dependence of the fields at λ_L and λ_F. In particular, the standing-wave patterns along the cavity axis cause different FORT trapping wells to contain different contributions of this noise from the locking laser. A more careful treatment of this effect has not yet been undertaken. There are

several reasons, however, that reduction of the intracavity power at λ_L may be required in future experiments (see Section 2.2.2), which would greatly reduce this contribution to the heating rate.

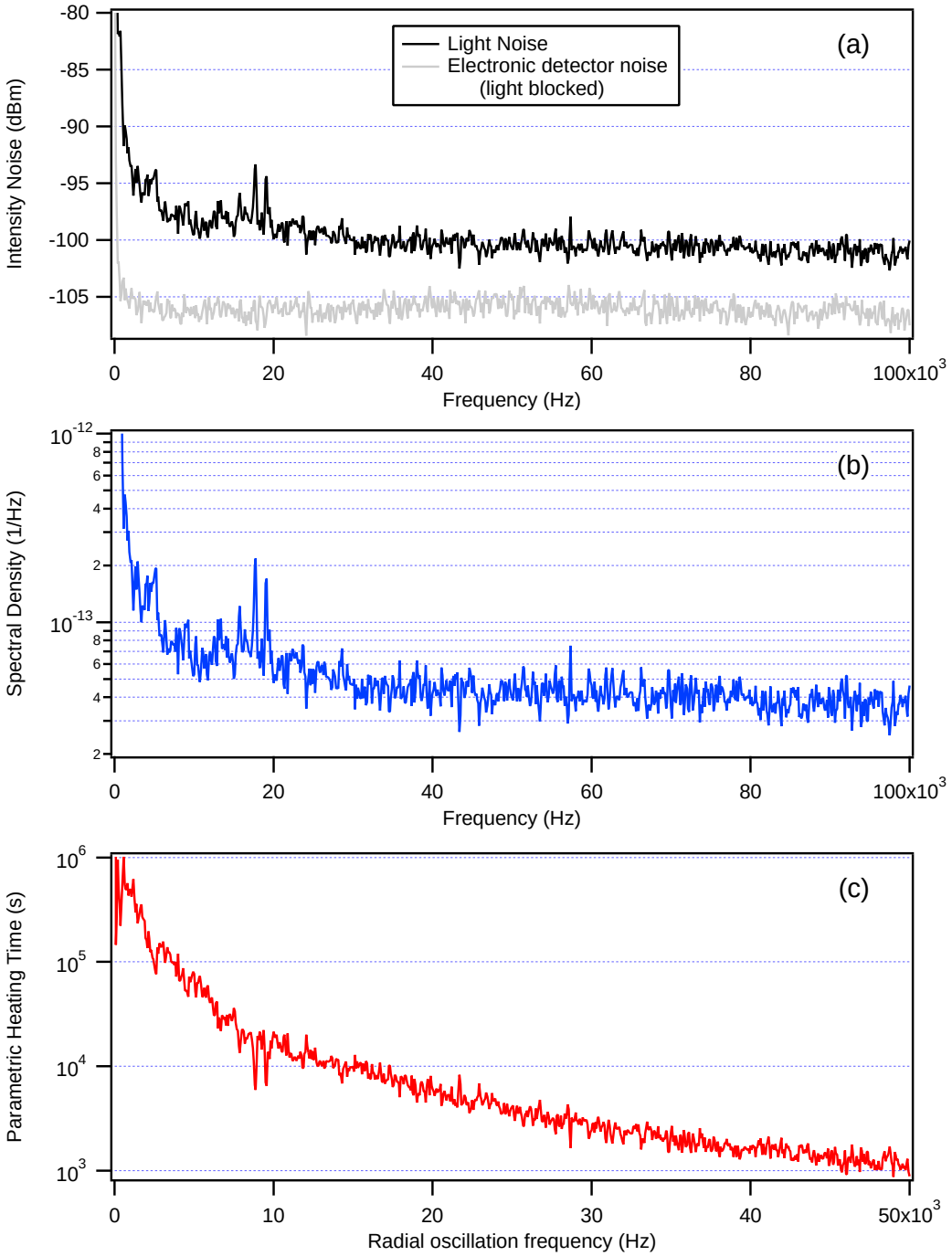

Figure 3.8: Intensity noise measurements of FORT cavity output light at $\lambda_F = 935.6$ nm, at frequencies relevant to the motion of trapped atoms perpendicular to the cavity axis. Panel (a) displays the spectrum analyzer output, panel (b) shows the spectral density of fractional intensity fluctuations, and panel (c) contains the predicted heating timescale, calculated using Equation 3.4. The maximum harmonic frequency of radial oscillation in our FORT is computed to be $\nu_{radial} = 4.8$ kHz. From panel (c) it is clear that lower frequencies give even slower heating rates, so that the parametric heating time should be at least $\tau_p^{radial} > 5 \times 10^4$ s. It is probably safe to assume this effect has a negligible impact on trapping and atomic temperature.

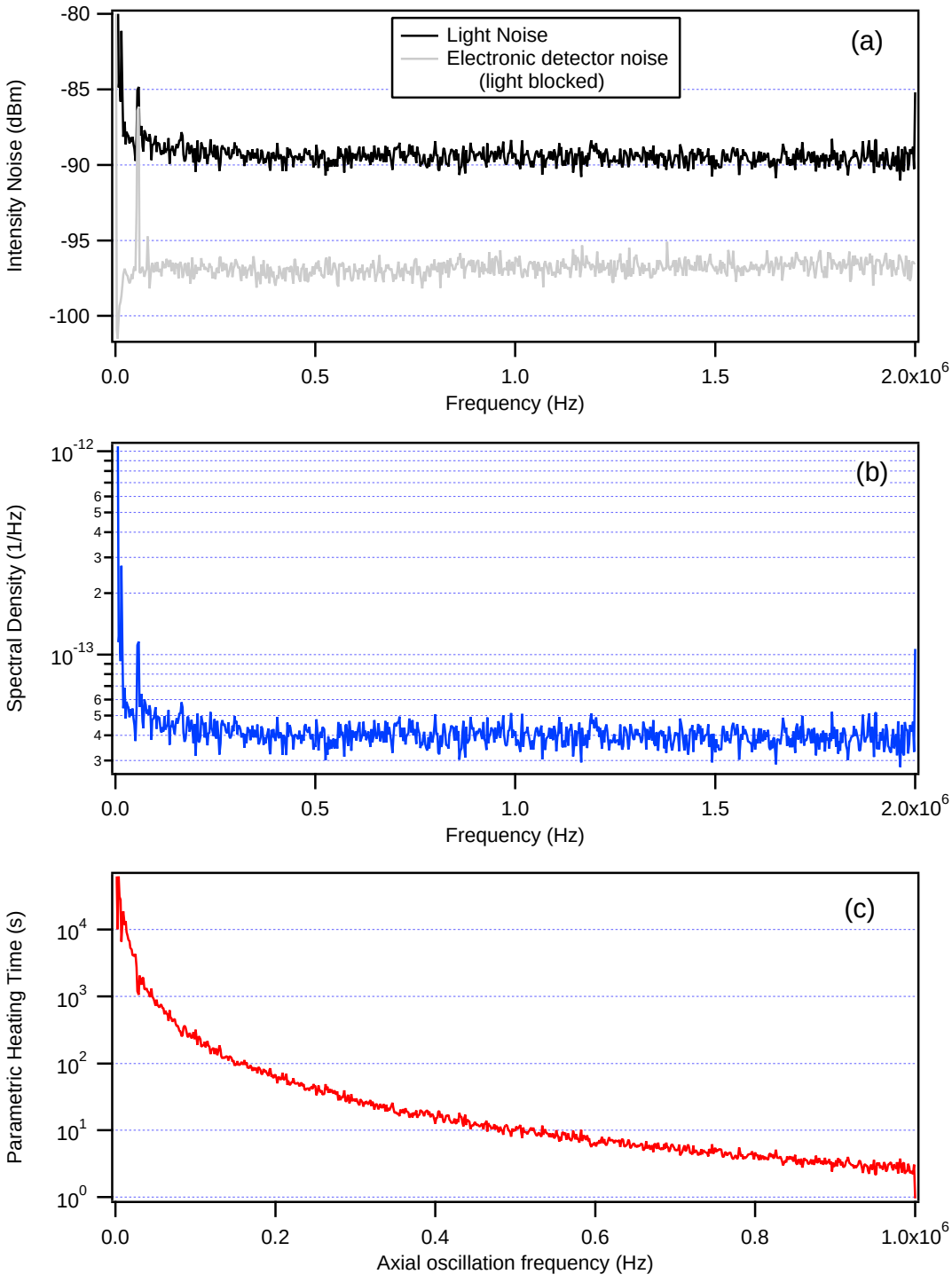

Figure 3.9: Intensity noise measurements of FORT cavity output light at $\lambda_F = 935.6$ nm, at frequencies relevant to the motion of trapped atoms along the cavity axis. The panels are organized as in Fig. 3.8. The maximum harmonic frequency of axial oscillation in our FORT is computed to be $\nu_{axial} = 570$ kHz. From panel (c) it is clear that lower frequencies give even slower heating rates, so that the parametric heating time should be at least $\tau_p^{radial} > 9$ s. This is also a lower bound in a different sense: this measurement is shot-noise limited (see text and Fig. 3.10).

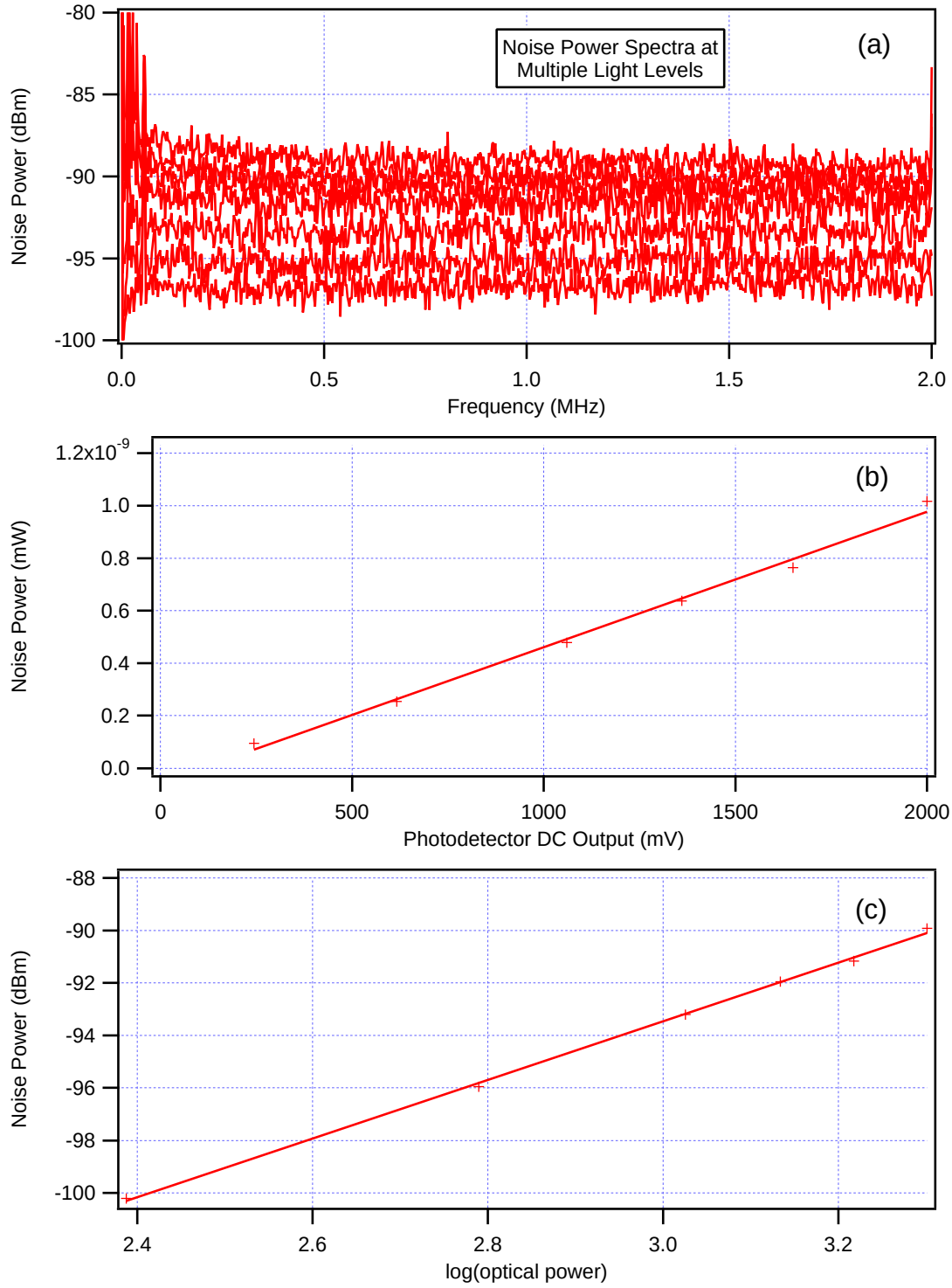

Figure 3.10: Dependence of measured intensity noise on the optical power. Panel (a) contains the noise spectra at the powers used. These traces are then averaged over the frequency range $500-1875$ kHz, and the results are plotted versus optical power in panels (b) and (c) (linear scale and log scale, respectively). The solid curves are linear fits to the data. The linear dependence of noise power vs. optical power strongly suggests that the measurement is shot noise limited.

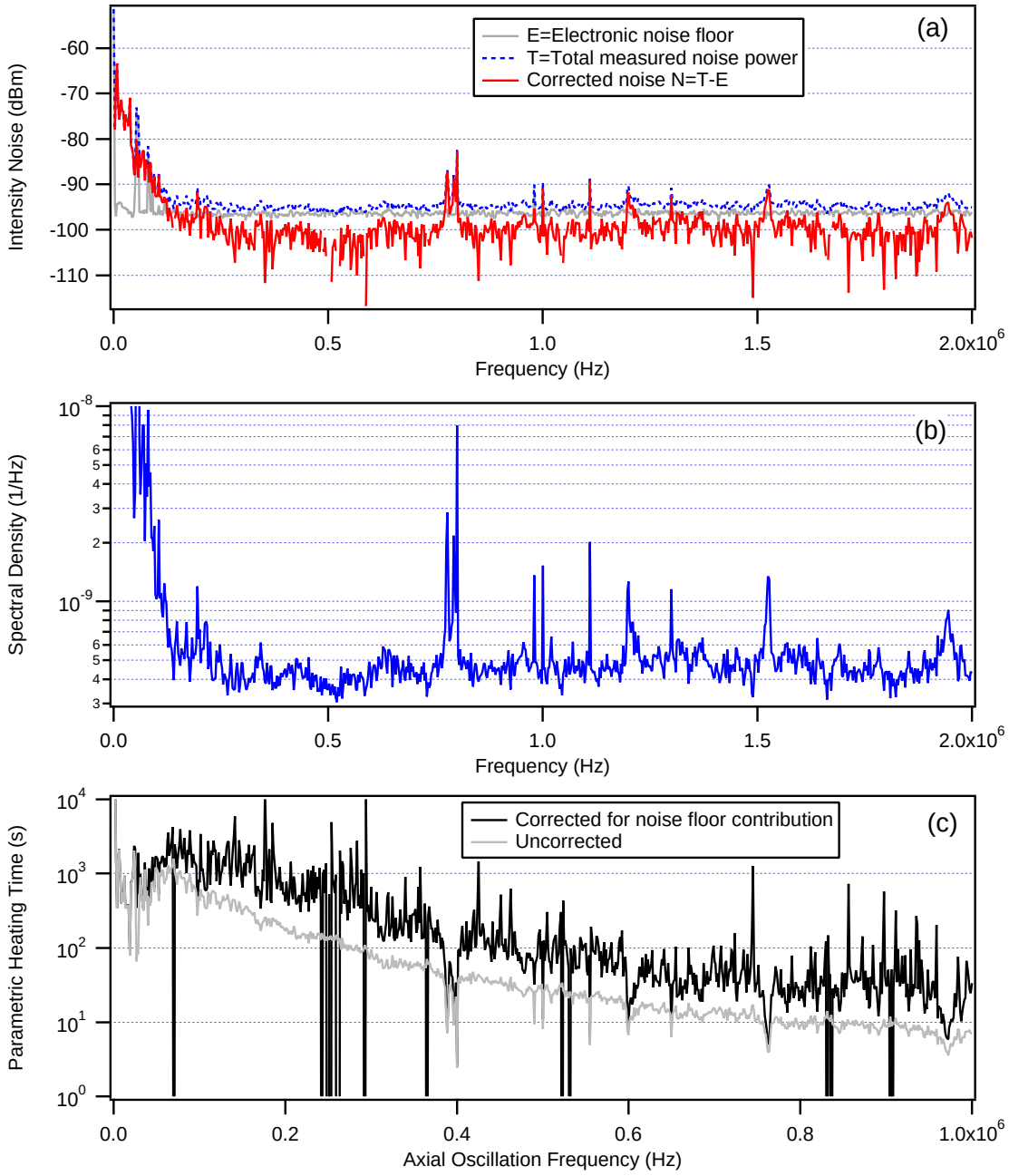

Figure 3.11: Intensity noise measurements of cavity output light from the locking laser at $\lambda_L = 836$ nm, at frequencies relevant to the motion of trapped atoms along the cavity axis. The panels are organized as in Figs. 3.8 and 3.9. In panel (b) the spectral density is *not* corrected for the noise floor contribution. See text for further discussion. In panel (c) the huge dips in the corrected trace should be ignored, since the uncorrected trace provides a lower bound for the heating time.

Chapter 4

Cavity QED "By The Numbers"

This chapter is reproduced from Ref. [33].

Cavity quantum electrodynamics (QED) provides a setting in which atoms interact predominantly with light in a single mode of an electromagnetic resonator of high quality factor Q [20]. Not only can the light from this mode be collected with high efficiency [36], but as well the associated rate of optical information for determining atomic position can greatly exceed the rate of free-space fluorescent decay employed for conventional imaging [24]. Moreover the regime of strong coupling, in which coherent quantum interactions between atoms and cavity field dominate dissipation, offers a unique setting for the study of open quantum systems [23]. Dynamical processes enabled by strong coupling in cavity QED provide powerful tools in the emerging field of quantum information science (QIS), including for the implementation of quantum computation [51] and for the realization of distributed quantum networks [21, 22].

With these prospects in mind, experiments in cavity QED have made made great strides in trapping single atoms in the regime of strong coupling [26, 24, 27, 31]. However, many protocols in QIS require multiple atoms to be trapped within the same cavity, with "quantum wiring" between internal states of the various atoms accomplished by way of strong coupling to the cavity field [51, 70, 71, 72]. Clearly the experimental ability to determine the number of trapped atoms coupled to a cavity is a critical first step toward the realization of diverse goals in QIS. Experimental efforts to combine ion trap technology with cavity QED are promising [30, 29], but have not yet reached the regime of strong coupling.

Here we report measurements in which the number of atoms trapped inside an optical cavity is observed in real time. After initial loading of the intracavity dipole trap with $\bar{N} \approx 5$ atoms, the decay of atom number $N \geq 3 \rightarrow 2 \rightarrow 1 \rightarrow 0$ is monitored by way of changes in the transmission of a near-resonant probe beam, with the transmitted light exhibiting a cascade of "stairsteps" as successive atoms leave the trap. After the probabilistic loading stage, the time required for the determination of a particular atom number $N = 1, 2, 3$ is much shorter than the mean interval over which the N atoms are trapped. Hence, a precise number of intracavity atoms can be prepared for

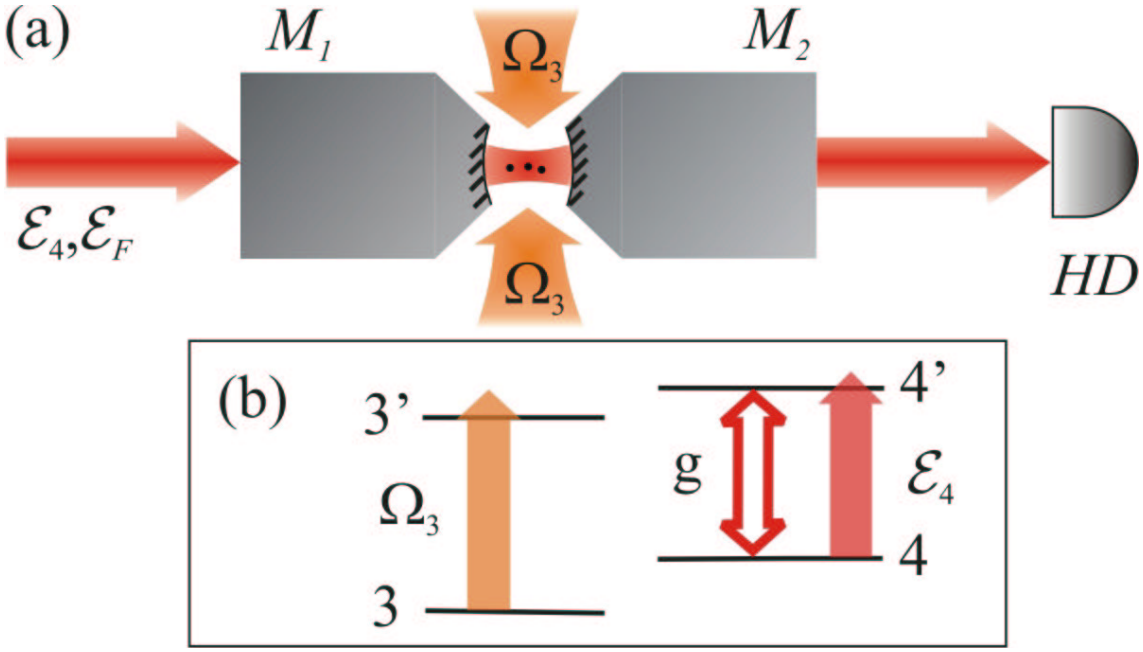

Figure 4.1: Schematic of our experiment. Cs atoms are loaded into an intracavity FORT ($\mathcal{E}_F$) by way of the transverse cooling field Ω_3 and the cavity probe field $\mathcal{E}_4$. The transmitted $\mathcal{E}_4$ field is directed to a heterodyne detector (*HD*), allowing real-time determination of intracavity atom number.

experiments in QIS, for which the timescales ($g^{-1} \approx 10^{-8}$ s) $\ll$ ($\tau \approx 3$ s), where τ is the atomic trapping time [27] and $\hbar g$ is the atom-field interaction energy. In the present case, the atom number is restricted to $N \lesssim 3$, but the novel detection scheme that we have developed may enable extensions to moderately larger atom numbers $N \lesssim 10$.

As illustrated in Fig. 4.1, our experiment combines laser cooling, state-insensitive trapping, and strong coupling in cavity QED, as were initially achieved in Ref. [27]. A cloud of Cs atoms is released from a magneto-optical trap (MOT) several mm above the cavity, which is formed by the reflective surfaces of mirrors (M_1, M_2) . Several atoms are cooled and loaded into an intracavity far-off-resonance trap (FORT) and are thereby strongly coupled to a single mode of the cavity. The maximum single-photon Rabi frequency $2g_0$ for one atom is given by $g_0/2\pi = 24$ MHz, and is based on the reduced dipole moment for the $6S_{1/2}, F = 4 \rightarrow 6P_{3/2}, F' = 4'$ transition of the $D2$ line in Cs at $\lambda_0 = 852.4$ nm. Decay rates for the $6P_{3/2}$ atomic excited states and the cavity mode at $\omega_0 = 2\pi c/\lambda_0$ are $\gamma/2\pi = 2.6$ MHz and $\kappa/2\pi = 4.2$ MHz, respectively. The fact that $g_0 \gg (\kappa, \gamma)$ places our system in the strong coupling regime of cavity QED [20], giving critical atom and photon numbers $n_0 \equiv \gamma^2/(2g_0^2) \approx 0.0057$, $N_0 \equiv 2\kappa\gamma/g_0^2 \approx 0.037$.

The cavity is independently stabilized and tuned such that it supports TEM_{00} modes simultaneously resonant with both the $F = 4 \rightarrow F' = 4'$ atomic transition at λ_0 and our FORT laser at $\lambda_F = 935.6$ nm, giving a length $l_0 = 42.2$ μm. A weak probe laser $\mathcal{E}_4$ excites the cavity mode at λ_0 with the cavity output directed to detector *HD*, while a much stronger trapping laser $\mathcal{E}_F$ drives the

mode at λ_F. In addition, the region between the cavity mirrors is illuminated by two orthogonal pairs of counter-propagating cooling beams in the transverse plane (denoted Ω_3). Atoms arriving in the region of the cavity mode are exposed to the $(\mathcal{E}_4, \mathcal{E}_F, \Omega_3)$ fields continuously, with a fraction of the atoms cooled and loaded into the FORT by the combined actions of the $\mathcal{E}_4$ and Ω_3 fields [27]. For all measurements, the cavity detuning from the $4 \rightarrow 4'$ atomic resonance is $\Delta_C = 0$. The detuning of the $\mathcal{E}_4$ probe from the atom-cavity resonance is $\Delta_4 = +4$ MHz, and its intensity is set such that the mean intracavity photon number $\bar{n} = 0.02$ with no atoms in the cavity. The detuning of the Ω_3 transverse cooling field is $\Delta_3 = +25$ MHz from the $F = 3 \rightarrow F' = 3'$ resonance, and its intensity is about $I_3 \approx 4 \times 10^1$ mW/cm^2.

The field $\mathcal{E}_F$ that drives the standing-wave, intracavity FORT is linearly polarized, resulting in nearly equal ac-Stark shifts for all Zeeman sublevels of the $F = 3, 4$ hyperfine ground states of the $6S_{1/2}$ manifold [64]. The peak value of the trapping potential is $-U_0/h = -47$ MHz, giving a trap depth $U_0/k_B = 2.2$ mK . A critical characteristic of the FORT is that all states within the $6P_{3/2}$ excited manifold likewise experience a *trapping* shift of roughly $-U_0$ (to within $\approx \pm 15\%$) [56, 57, 55, 27], which enables continuous monitoring of trapped atoms in our cavity and avoids certain heating effects.

Figure 4.2(a) displays a typical record of the heterodyne current $i(t)$ resulting from one instance of FORT loading. Here, the current $i(t)$ is referenced to the amplitude of the intracavity field $|\langle \hat{a} \rangle|$ by way of the known propagation and detection efficiencies. The initial sharp drop in $|\langle \hat{a}(t) \rangle|$ around $t = 0$ results from atoms that are cooled and loaded into the FORT by the combined action of the $(\mathcal{E}_4, \Omega_3)$ fields [27]. Falling atoms are not exposed to $\mathcal{E}_4$ until they reach the cavity mode, presumably leading to efficient trap loading for atoms that arrive at a region of overlap between the standing waves at (λ_0, λ_F) for the $(\mathcal{E}_4, \mathcal{E}_F)$ fields. Trap loading always occurs within a ± 10 ms window around $t = 0.025$ s (relative to $t = 0$ in Fig. 4.2(a)). This interval is determined using separate measurements of the arrival time distribution of freely falling atoms in the absence of the FORT [60, 26].

Subsequent to this loading phase, a number of remarkable features are apparent in the trace of Fig. 4.2(a), and are consistently present in all the data. The most notable characteristic is the fact that the transmission versus time consists of a series of flat "plateaus" in which the field amplitude is stable on long timescales. Additionally, these plateaus reappear at nearly the same heights in all repeated trials of the experiment, as is clearly evidenced by the histogram of Fig. 4.2 (b). We hypothesize that each of these plateaus represents a different number N of trapped atoms coupled to the cavity mode, as indicated by the arrows in Fig. 4.2.

Consider first the one-atom case, which unexpectedly exhibits relatively large transmission and small variance. For fixed drive $\mathcal{E}_4$, the intracavity field is a function of the coupling parameter $g^{(i,f)}(\mathbf{r}) = g_0 G_{i,f} \sin(k_0 z) \exp(-2\rho^2/w_0^2)$ where ρ is the transverse distance from the cavity axis (z),

$k_0 = 2\pi/\lambda_0$, and $G_{i,f}$ relates to the Clebsch-Gordan coefficient for particular initial and final states (i, f) within the $F = 4, F' = 4'$ manifolds. Variations in g as a function of the atom's position $\mathbf{r}$ and internal state might reasonably be expected to lead to large variations of the intracavity field, both as a function of time and from atom to atom [61, 73].

However, one atom in the cavity produces a reasonably well-defined intracavity intensity $I \propto |\langle \hat{a} \rangle|^2$ due to the interplay of two effects. The first is that for small probe detunings Δ_4, the intracavity intensity I_1 for one atom is suppressed by a factor f relative to the empty-cavity intensity I_0, where for weak excitation, $f \approx 4C_1^2 \gg 1$ with $C_1 = g^2/2\kappa\gamma$. A persistent, strongly reduced transmission thereby results, since the condition $[C_1^{(i,f)}(\mathbf{r})]^2 \gg 1$ is robust to large fluctuations in atomic position $\mathbf{r}$ and internal state. The second effect is that the $F = 4 \leftrightarrow F' = 4'$ transition cannot be approximated by a closed, two-level system, since the $F' = 4'$ excited states decay to both $F = 3, 4$ hyperfine ground levels. As illustrated in Fig. 4.1(b), an atom thus spends a fraction q of its time in the cavity QED manifold $(4, 4')$, and a fraction $p \approx 1 - q$ in the $(3, 3')$ manifold. In this latter case, the effective coupling is negligible ($C_1^{eff} \approx 4 \times 10^{-4}$), leading to an intensity that approximates I_0. Hence, the intracavity intensity as a function of time $I(t)$ should have the character of a random telegraph signal switching between levels (I_0, I_1), with dwell times determined by $(\mathcal{E}_4, \Omega_3)$, which in turn set p.[1] Since $(\mathcal{E}_4, \Omega_3)$ drive their respective transitions near saturation, the timescale $\tau_P \sim 1$ μs for optical pumping from one manifold to another is much faster than the inverse detection bandwidth $(1/2\pi B) \approx 160$ μs. The fast modulation of the intracavity intensity due to optical pumping processes thereby gives rise to an average detected signal corresponding to intensity $\bar{I}_1 \approx pI_0 + qI_1 \approx pI_0$ for $I_1 \ll I_0$.

This explanation for the case of 1 atom can be extended to N intracavity atoms to provide a simple model for the "stairsteps" evidenced in Fig. 4.2(a). For N atoms, the intracavity intensity should again take the form of a random telegraph signal, now switching between the levels (I_0, I_k), with high transmission I_0 during intervals when all N atoms happen to be pumped into the $(3, 3')$ manifold, and with low transmission $I_k \leq I_1$ anytime that $1 \leq k \leq N$ atoms reside in the $(4, 4')$ manifold, where $I_k \sim I_1/k^2$ for weak excitation with $\Delta_C = \Delta_4 = 0$. The intracavity intensities $\{I_k\}$ determine the transition rates $\{\gamma_{k\to k-1}\}$ between states with k and $k-1$ atoms in the $(4, 4')$ manifold, while Ω_3 determines $\{\gamma_{k-1\to k}\}$ for $k-1 \to k$ via transitions from the $(3, 3')$ manifold. For the hierarchy of states $k = 0, 1, \ldots, N$ with transition rates $\{\gamma_{k\to k-1}, \gamma_{k-1\to k}\}$, it is straightforward to determine the steady-state populations $p_k^{(N)}$. With the physically motivated assignments $\gamma_{k-1\to k} = \gamma_{0\to 1}$ independent of k and $\gamma_{k\to k-1} = \gamma_{1\to 0}/k^2$ corresponding to $I_k \sim I_1/k^2$, we find that $p_0^{(N)} =$

[1] Fluctuations in intracavity intensity can also arise from optical pumping into dark states. Although the $\mathcal{E}_4$ probe field is linearly polarized with dark state $(F = 4, m_F = 0)$, independent measurements indicate the presence of significant Zeeman splittings $\Delta\nu_\pm \approx 0.5$ MHz for $\Delta m_F = \pm 1$, partially arising from residual ellipticity of the FORT field [27, 64] and from uncompensated stray magnetic fields. Moreover, an atom moving at $v = 10$ cm/s travels through the polarization gradients of the Ω_3 field in ≈ 4 μs, ensuring rapid pumping from dark states in the $F = 3$ ground level. Occupation of dark states for extended periods is thereby precluded, as is supported by detailed Monte-Carlo simulations for $N = 1$ [74].

$1/\sum_{k=0}^{N}(k!)^2 y^k$, where $y \equiv \gamma_{0\to1}/\gamma_{1\to0}$. Hence, for $I_k \ll I_0$, the prediction for the average intensity is $\bar{I}_N \approx p_0^{(N)} I_0$, which leads to a sequence of plateaus of increasing heights $\bar{I}_{N+1} \to \bar{I}_N \to \bar{I}_{N-1}$ as successive atoms are lost from the trap $N+1 \to N \to N-1$.

Figure 4.2(c) compares the prediction of this simple model with the measured values of peak positions in (b). The only adjustable parameter is the value $y = 0.5$, resulting in reasonable correspondence between the model and the measurements. Also shown are values $p_0^{(N)}$ for $y = 0.1$ to indicate that it might be possible to enhance the resolution for a particular range of atom number by framing a given few values $N_1, N_1 \pm 1$ in the transition region $p_0^{(N_1)} \approx 0.5$, where $N_1 \approx 6$ in (c). This could be accomplished by adjusting the relative strengths of the $(\mathcal{E}_4, \Omega_3)$ fields and hence y.

Although our simple model accounts for the qualitative features in Fig. 4.2, a quantitative description requires a considerably more complex analysis based upon the full master equation for N intracavity atoms, including the multiple Zeeman states and atomic motion through the polarization gradients of the Ω_3 beams. We have made initial efforts in this direction [74] for one atom, and are working to extend the treatment to $N \geq 2$ atoms.

Beyond these considerations, additional evidence that the plateaus in Fig. 4.2 correspond to definite atom numbers is provided by Fig. 4.3. Here, the data recorded for the probe transmission have been binned not only with respect to the value of $|\langle\hat{a}\rangle|$ as in Fig. 4.2(b), but also as a function of time. Definite plateaus for $|\langle\hat{a}\rangle|$ are again apparent, but now their characteristic time evolution can be determined. The critical feature of this plot is that the plateaus lying at higher values of $|\langle\hat{a}\rangle|$ correspond to times *later* in the trapping interval, in agreement with the expectation that N should always decrease with time beyond the small window of trap loading around $t = 0.025$ s. This average characteristic of the entire data set supports our hypothesis that the plateaus in $|\langle\hat{a}\rangle|$ correspond to definite intracavity atom numbers N, as indicated in Figs. 4.2 and 4.3. Moreover, none of the 500 traces in the data set includes a downward step in transmission after the initial trap loading.

To examine the dynamics of the trap loss more quantitatively, we consider each atom number individually by integrating the "plateau" regions along the $|\langle\hat{a}(t)\rangle|$ axis for each time t. The dashed horizontal lines in Fig. 4.3 indicate the boundaries chosen to define the limits of integration for each value of N. We thereby obtain time-dependent "populations" $\Phi_N(t)$ for $N = 0, 1, 2$, and $\Phi_{\geq3}(t) = \sum_{N=3}^{\infty}\Phi_N(t)$, which are plotted in Fig. 4.4(a). To isolate the decay dynamics from those of trap loading, we plot the data beginning at $t_0 = 0.034$ s with respect to the origin in Figs. 4.2(a) and 4.3. The qualitative behavior of these populations is sensible, since almost all trials begin with $N \geq 3$, eventually decaying to $N = 2, 1, 0$.

The quantities $\Phi_N(t)$ are approximately proportional to the fraction of experimental trials in which N atoms were trapped at time t, so long as the characteristic duration Δt_N of each plateau far exceeds the time resolution of the detection. If the bandwidth is too low, transient steps no longer represent a negligible fraction of the data, as is the case for transitions between the shortest-lived

levels (e.g., $N = 3 \rightarrow 2$). We estimate that this ambiguity causes uncertainties in Φ_N at the $5-10\%$ level.

Also shown in panel (b) of Fig. 4.4 is the result of a simple birth-death model for predicting the time evolution of the populations, namely, $\dot{P}_N(t) = -\Gamma(NP_N(t) - (N+1)P_{N+1}(t))$, where $P_N(t)$ represents the probability of N atoms in the trap. The main assumption of the model is that there is one characteristic decay rate Γ for trapped atoms, and that each atom leaves the trap independently of all others. Initial conditions for $N = 0$, 1 and 2 for the solution presented in Fig. 4.4(b) are obtained directly from the experimental data after trap loading, $\Phi_N(t_0)$. Since the plateaus for higher values of N are not well resolved, we use a Poisson distribution for $N \geq 3$. The mean $\mu = 5.2$ is obtained by solving $\sum_{N=3}^{\infty} e^{-\mu}\mu^N/N! = \Phi_{N\geq 3}(t_0)$. Given these initial conditions, we perform a least-squares fit of the set of analytic solutions $\{P_N(t)\}$ to the set of experimental curves $\{\Phi_N(t)\}$ with Γ the only free parameter, resulting in the curves in Fig. 4.4(b) with $\Gamma = 8.5$ s^{-1}. Although there is reasonable correspondence between Figs. 4.4 (a) and (b), $\Phi_N(t)$ evolves more rapidly than does $P_N(t)$ at early times, and yet the data decay more slowly at long times. This suggests that there might be more than one timescale involved, possibly due to an inhomogeneity of decay rates from atom to atom or to a dependence of the decay rate on N. We have observed non-exponential decay behavior in other measurements of single-atom trap lifetimes, and are working to understand the underlying trap dynamics.

Our experiment represents a new method for the real-time determination of the number of atoms trapped and strongly coupled to an optical cavity. We emphasize that an exact number $N = 1$ to 3 coupled atoms can be prepared in our cavity within ≈ 200 ms from the release of the MOT. Although the trap loading is not deterministic, N can be measured quickly compared to the subsequent trapping time $\tau \approx 3$ s [27]. These new capabilities are important for the realization of various protocols in quantum information science, including probabilistic protocols for entangling multiple atoms in a cavity [70, 71, 72]. Although our current investigation has centered on the case of small $N \leq 3$, there are reasonable prospects to extend our technique to higher values $N \lesssim 10$ as, for example, by way of the strategy illustrated in Fig. 4.2(c). Moreover, the rate at which we acquire information about N can be substantially increased from the current value $\kappa|\langle\hat{a}\rangle|^2 \sim 10^5$/s toward the maximum rate for optical information $g^2/\kappa \gtrsim 10^8$/s, which can be much greater than the rate for fluorescent imaging set by γ [24].

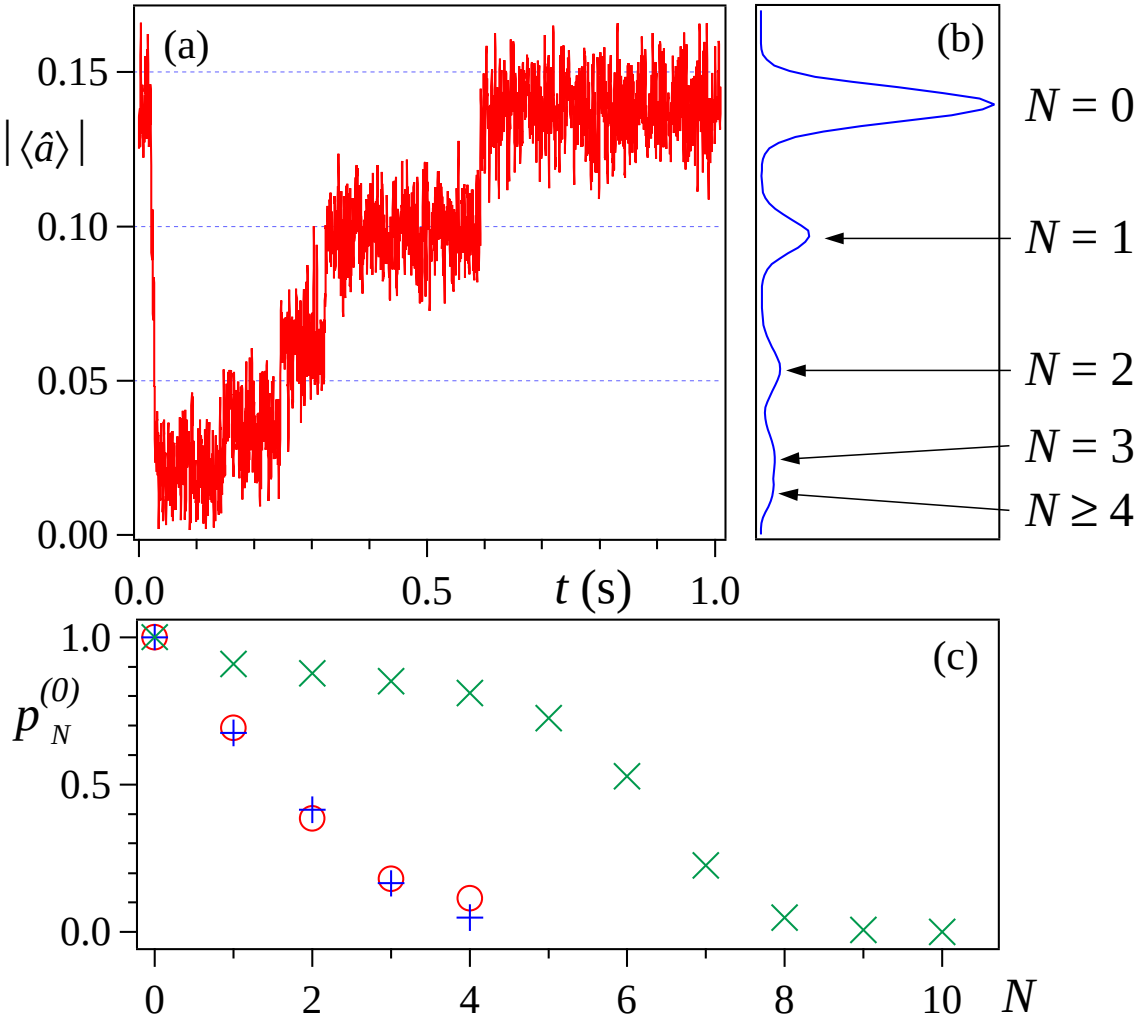

Figure 4.2: (a) A typical detection record in which several ($N > 4$) atoms are loaded into the trap. Heterodyne detection bandwidth is 1 kHz. (b) Histogram of 500 such traces, binned with respect to the heterodyne signal $|\langle\hat{a}\rangle|$. A digital low-pass filter of bandwidth 100 Hz is applied to each trace prior to the computation of the histogram. (c) Comparison of the model prediction for $p_0^{(N)}(y = 0.5)$ (+) with the measured positions of the histogram peaks in (b) (◯). Also shown (×) is $p_0^{(N)}(y = 0.1)$ to indicate the possibility to detect specific atom numbers for larger $\bar{N}$.

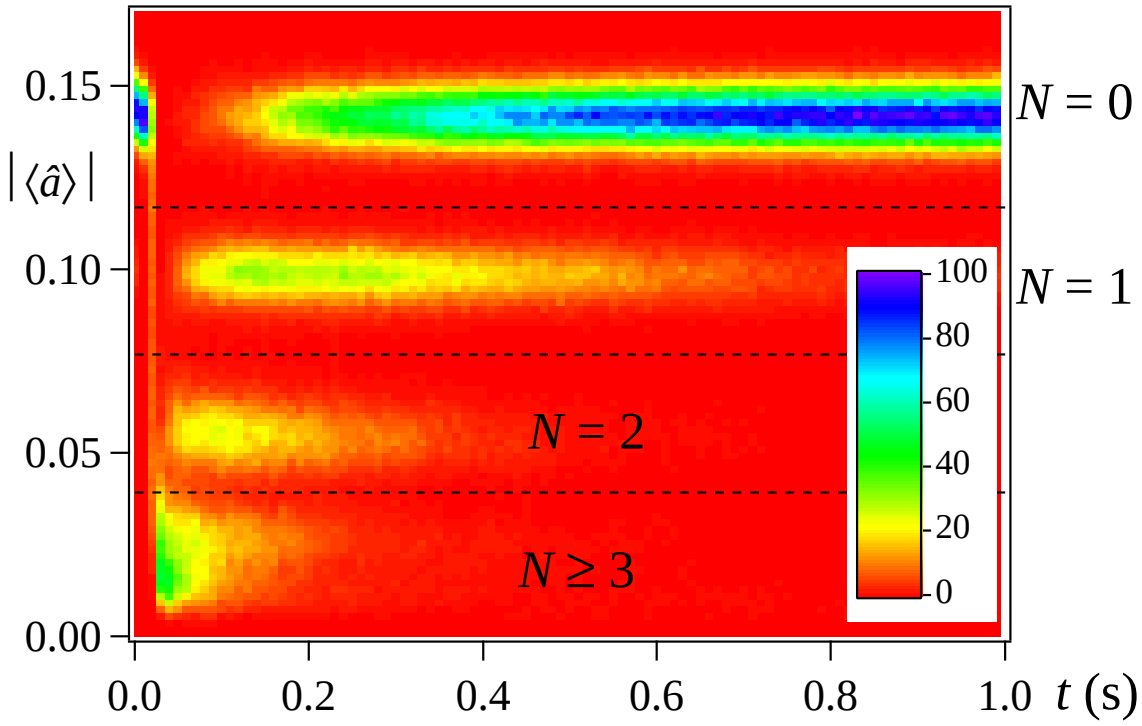

Figure 4.3: Histogram of 500 traces such as the one in Fig. 4.2(a), binned with respect to both signal strength $|\langle\hat{a}\rangle|$ and time t. The signals are filtered first as in Fig. 4.2(b).

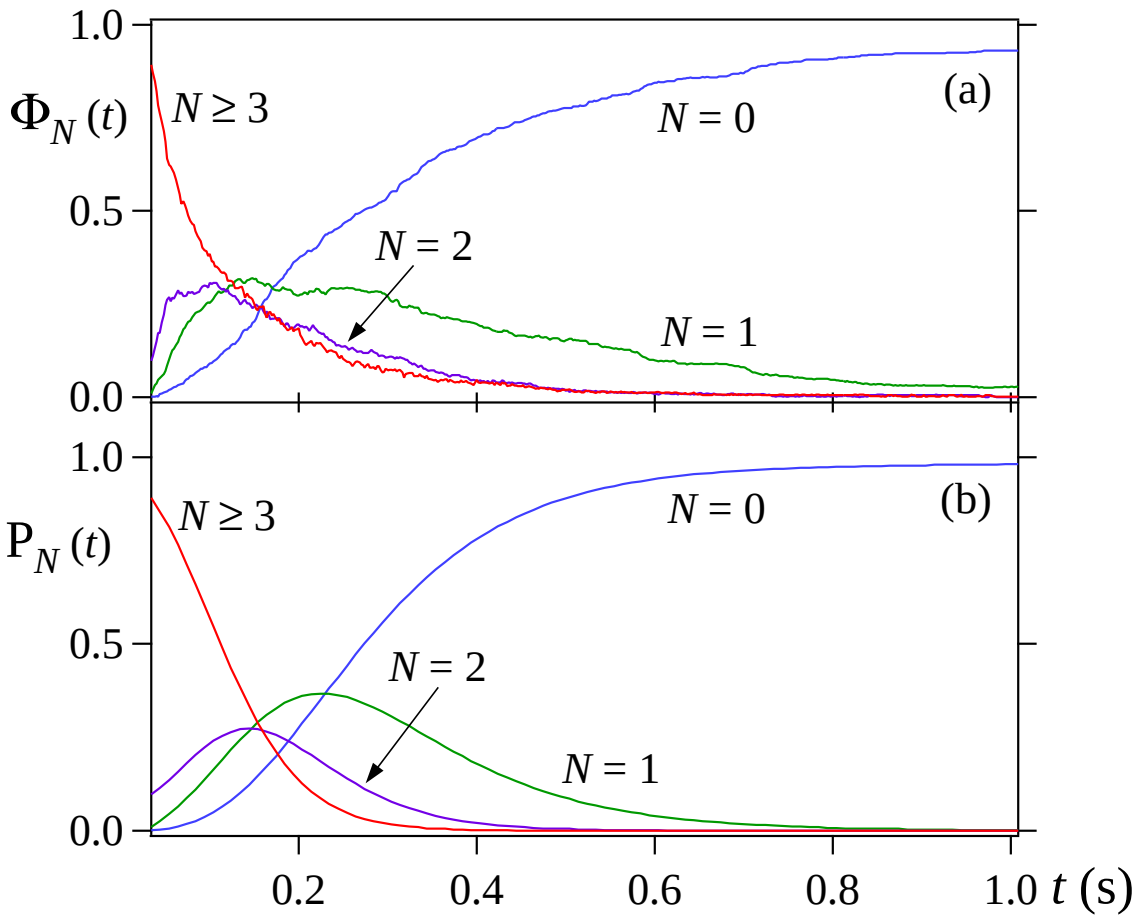

Figure 4.4: (a) Experimental results for the time evolution of the N-atom populations $\Phi_N(t)$, which are normalized such that their sum is approximately unity throughout the interval shown. (b) The results of a simple model calculation $P_N(t)$ are fit to the data $\Phi_N(t)$ with one free parameter, the single atom decay rate Γ.

Chapter 5

A One-Atom Laser in a Regime of Strong Coupling

This chapter is reproduced from Ref. [35].

Although conventional lasers operate with a large number of intracavity atoms, the lasing properties of a single atom in a resonant cavity have been theoretically investigated for more than a decade [75, 76, 77, 78, 79, 80, 81, 82, 83, 84, 85]. Recent advances in cavity quantum electrodynamics allow one atom to be isolated in an optical cavity in a regime for which one photon is sufficient to saturate the atomic transition [27]. Here we report the use of such a system for the experimental realization of a one-atom laser operated in a regime of strong coupling. The observed characteristics of the atom-cavity system in this regime are qualitatively different from those of the familiar many atom case. Specifically, we present measurements of intracavity photon number versus pump intensity that exhibit "thresholdless" behavior, and infer that the output flux from the cavity mode exceeds that from atomic fluorescence by more than tenfold. Observations of the second-order intensity correlation function $g^{(2)}(\tau)$ demonstrate that our one-atom laser generates manifestly quantum (i.e., nonclassical) light that exhibits both photon antibunching $g^{(2)}(0) < g^{(2)}(\tau)$ and sub-Poissonian photon statistics $g^{(2)}(0) < 1$.

Lasers are typically realized with large atom and photon number in a domain of *weak coupling* for which individual quanta have negligible impact on the system dynamics. Usual laser theories therefore rely on system-size expansions in inverse powers of critical atom and photon numbers $(N_0, n_0) \gg 1$, and arrive at a consistent form for the laser characteristics [86, 87, 69, 88, 89]. However, over the past twenty years, technical advances on various fronts have pushed laser operation to regimes of ever smaller atom and photon number, pressing toward the limit of *strong coupling* for which $(N_0, n_0) \ll 1$ [20]. Significant milestones include the realization of one- and two-photon *micromasers* [90, 91, 92], as well as novel microlasers in atomic and condensed matter systems [93, 94, 95].

In this march toward ever smaller systems, an intriguing possibility is that a laser might be

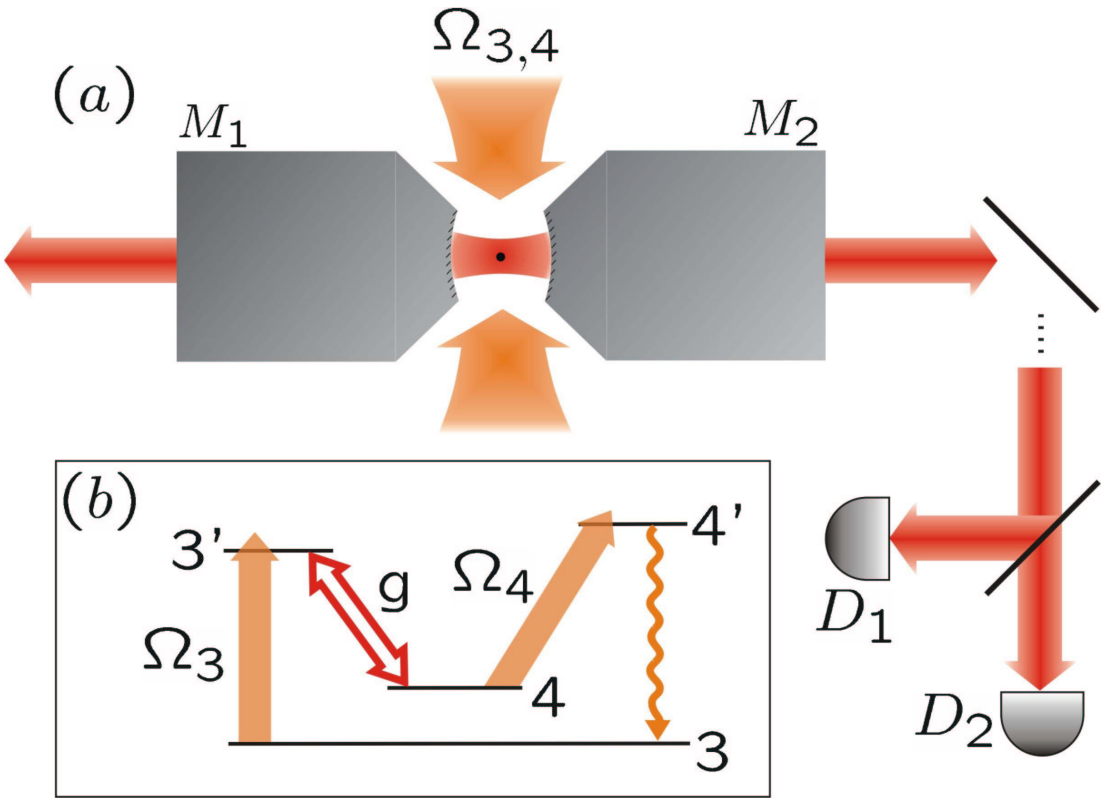

Figure 5.1: A simplified schematic of the experiment. (a) A Cesium atom (black dot) is trapped inside a high-finesse optical cavity formed by the curved, reflective surfaces of mirrors $M_{1,2}$. Light generated by the atom's interaction with the resonant cavity mode propagates as a Gaussian beam to single-photon detectors $D_{1,2}$. (b) The relevant transitions involve the $6S_{1/2}, F = 3, 4 \leftrightarrow 6P_{3/2}, F' = 3', 4'$ levels of the D_2 line at 852.4 nm in atomic Cesium. Strong coupling at rate g is achieved for the lasing transition $F' = 3' \rightarrow F = 4$ near a cavity resonance. Pumping of the upper level $F = 3'$ is provided by the field Ω_3, while recycling of the lower level $F = 4$ is achieved by way of the field Ω_4 $(4 \rightarrow 4')$ and spontaneous decay back to $F = 3$. Decay $(3', 4') \rightarrow (3, 4)$ is also included. Relevant cavity parameters are length $l_0 = 42.2$ μm, waist $w_0 = 23.6$ μm, and finesse $\mathcal{F} = 4.2 \times 10^5$ at $\lambda_{D_2} = 852$ nm.

obtained with a single atom in an optical cavity, as was considered in the seminal work of Mu and Savage [75] and has since been extensively analyzed [76, 77, 78, 79, 80, 81, 82, 83, 84, 85]. Here we report an important advance in this quest, namely, the operation of a one-atom laser in a regime for which $(N_0, n_0) \ll 1$. As illustrated in Fig. 5.1, our experiment consists of a single Cesium atom trapped within a high-finesse optical cavity [26, 25, 27]. The lasing transition $6P_{3/2}, F' = 3' \rightarrow 6S_{1/2}, F = 4$ is nearly resonant with and strongly coupled to a single mode of this cavity. The coupling is parameterized by the Rabi frequency $2g_0$ for a single quantum of excitation, and the atom and field have amplitude decay rates γ and κ, respectively. The upper level $F' = 3'$ is pumped by the external drive Ω_3, while effective decay of the lower level $F = 4$ takes place via the combination of the drive Ω_4 and decay γ_{34}, $4 \rightarrow 4' \rightarrow 3$. In essential character this system is analogous to a Raman scheme with pumping $3 \rightarrow 3'$, lasing $3' \rightarrow 4$, and decay $4 \rightarrow 3$. Of particular

relevance to our work are the detailed treatments of the ion-trap laser by Walther and colleagues [80, 81, 82, 83]. We also emphasize that a "one-and-the-same" atom laser as illustrated in Fig. 5.1 is quite distinct from "single-atom" micro-masers [90, 91, 92] and lasers [93] for which steady state is reached through the incremental contributions of many atoms that transit the cavity, even if one by one. Indeed, our pumped atom-cavity system is a continuous source of nonclassical light for the entire duration that an atom is trapped, typically lasting $50 - 100$ ms.

Because conventional lasers operate in the limit $(N_0, n_0) \gg 1$, there is a generic form associated with the laser threshold in the transition from nonlasing to lasing action that is independent of the model system [86, 96]. However, as the system size is reduced, the sharpness of the laser "turn on" is lost, with then no clear consensus about how to define the lasing threshold [96]. Well into the regime of strong coupling $(N_0, n_0) \ll 1$, even the familiar qualitative characteristics of a laser (e.g., the statistical properties of the output light) are profoundly altered, leaving open the question of how to recognize a laser in this new regime.

The perspective that we adopt here is to trace the lineage of our one-atom laser from a conventional regime continuously into the domain of strong coupling. We do this by considering a scenario where an atom is placed in a cavity which undergoes a transformation from very large to very small mode volume. The cavity length l is reduced such that the cross-sectional area of the cavity mode at the position of the atom and the mirror reflectivity are both held constant. Since $g_0 \propto l^{-1/2}$ and $\kappa \propto l^{-1}$, $N_0 = \frac{2\kappa\gamma}{g_0^2}$ remains constant independent of l. On the other hand, the saturation photon number $n_0 = \frac{\gamma^2}{2g_0^2} \propto l$ decreases, so that the electric field per photon $E_1 \propto \frac{1}{\sqrt{n_0}}$ increases. Hence the simple prescription of "shrinking" the cavity leads inevitably to a regime for which single-photon processes become dominant, and for which predictions from the conventional laser theory and the full quantum analysis should diverge.

For a four-state model based upon Fig. 5.1(b), it is straightforward to derive equations of motion for expectation values of atom and field operators. The conventional semiclassical theory is obtained from the factorization $\langle \hat{\sigma}_{ij}(t)\hat{a}(t)\rangle = \langle \hat{\sigma}_{ij}(t)\rangle\langle \hat{a}(t)\rangle$, where $\hat{\sigma}_{ij} = |i\rangle\langle j|$ are the atomic projection operators for the set of states (i, j) and $\hat{a}$ is the annihilation operator for the intracavity field. The steady-state solution $\alpha \equiv \langle \hat{a}\rangle_{ss}$ to these semiclassical equations is plotted in Fig. 5.2 for parameters relevant to our experiment (i.e., same values of (n_0, N_0) and of atomic decay rates) and exhibits a clearly defined laser threshold. Around this threshold, familiar characteristics for conventional lasers are found, including population inversion [74]. In these calculations, we used our experimental value for the cooperativity parameter $C_1 = 1/N_0 \simeq 12$. Indeed, the condition $C_1 \gg 1$ is required to observe threshold behavior for one atom pumped inside the resonator.

To obtain a fully quantum description for the four-state model based upon Fig. 5.1(b), we carry out numerical solutions of the master equation for the density operator $\hat{\rho}$ for atom and field [97, 74]. These solutions can then be employed to investigate the passage from the semiclassical

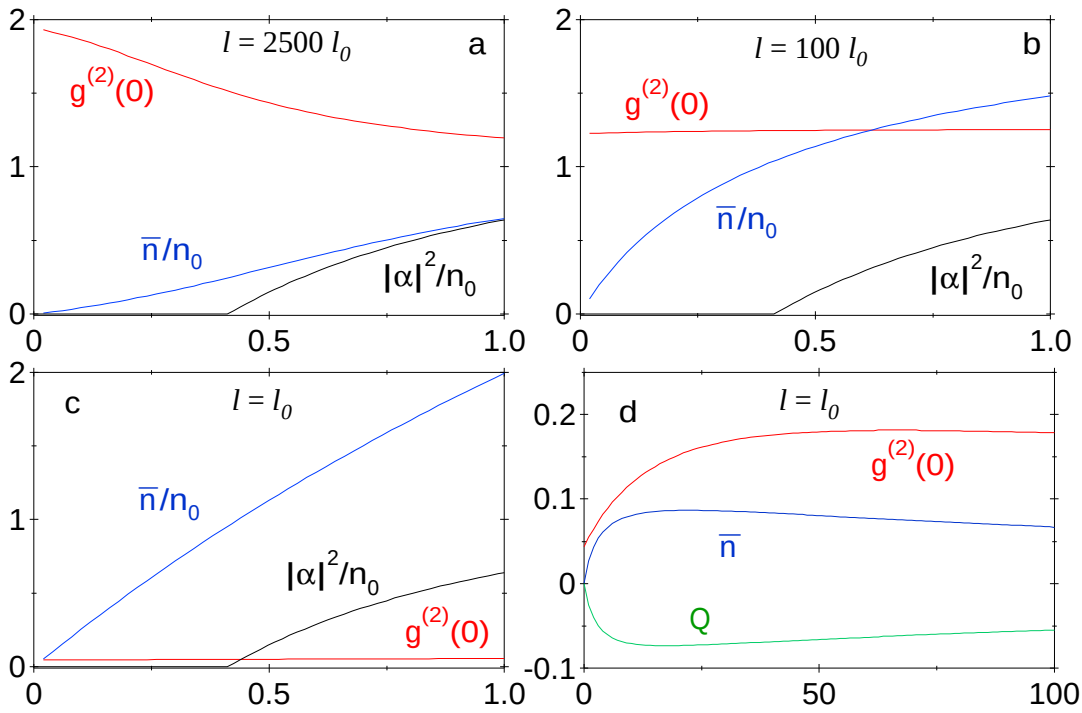

Figure 5.2: The mean intracavity photon number $\bar{n}/n_0$ (blue) and normalized intensity correlation function $g^{(2)}(0)$ (red) are plotted as functions of pump intensity $I_3 = (\Omega_3/2\gamma)^2$ in (a)-(d). In (a)-(c), the cavity length is made progressively shorter ($2500l_0$, $100l_0$, l_0), with l_0 representing our experiment. The corresponding saturation photon numbers are (33.0, 1.32, 0.013). $\bar{n}/n_0$ and $g^{(2)}(0)$ are calculated from the quantum theory for the four-state system in Fig. 5.1, while $|\alpha|^2/n_0$ given by the black curve is from the semiclassical theory. (d) $\bar{n}$ (blue), $g^{(2)}(0)$ (red), and the Mandel Q parameter (green) shown over an extended range of pump intensity I_3 for $l = l_0$. In all cases, $I_4 = (\Omega_4/2\gamma)^2 = 2$, the $3 \rightarrow 4'$ and $4 \rightarrow 4'$ transitions are driven on resonance, and the cavity detuning $\omega_{CA} = 0$. The partial decay rates for the $6P_{3/2} \rightarrow 6S_{1/2}$ Cs transitions shown in Fig. 5.1(b) are as follows: $(\gamma_{33}, \gamma_{43}, \gamma_{44}, \gamma_{34}) = (\frac{3}{4}, \frac{1}{4}, \frac{7}{12}, \frac{5}{12})\gamma$, where γ_{ij} is the decay rate from level i to level j. Other parameters are as given in the text.

regime to the quantum domain. An example relevant to our experiment is illustrated by the series of curves shown in Fig. 5.2 for decreasing cavity length $2500l_0 \rightarrow l_0$, where $l_0 = 42.2$ μm is the length of our actual cavity. Clearly, a large cavity volume with $l \gg l_0$ brings us closer to the domain of conventional lasers, as evidenced in Fig. 5.2(a) for $l = 2500l_0$. The laser output curve $\bar{n}/n_0$ versus pump intensity I_3 is to be compared to the semiclassical calculation $|\alpha|^2/n_0$. As for the normalized intensity correlation function $g^{(2)}(0)$ of Fig. 5.2(a), recall that a conventional laser generates an output with Gaussian statistics $g^{(2)}(0) = 2$ below threshold and passes smoothly to light that approximates a coherent state with $g^{(2)}(0) = 1$ as the pump increases through threshold [86, 87, 69, 88, 89]. Moreover, for large l the Mandel Q parameter exhibits two maxima as a function of I_3, one around the conventional threshold and one for large pump values [74, 96, 80, 83], which gradually develop into a single broad minimum with decreasing l. In all cases, $\bar{n}$, $g^{(2)}$, and Q, as well as the various atomic populations, display pronounced functional dependences on the pump level I_3

that require a self-consistent treatment of atom and cavity field, here in the fully quantum regime as opposed to the limit of large (N_0, n_0) in conventional laser theories.

Since N_0 remains constant independent of l and because the semiclassical solution $|\alpha|^2/n_0$ is independent of n_0, the increasing disparity between the functions shown in (a)-(c) in Fig. 5.2 for decreasing l indicates the continuous passage away from the domain of conventional laser operation and into a regime of strong coupling where various nonclassical features emerge (e.g., $g^{(2)}(0) < 1$), as predicted in prior treatments of one-atom lasers [75, 77, 78, 79, 80, 82, 83, 84, 85]. Figure 5.2(d) provides a global perspective of some of these characteristics over a wider range of the pump intensity I_3 for $l = l_0$ relevant to our experiment. The input-output relationship $\bar{n}$ versus I_3 has several key features to be compared with experimental results presented below, namely, the immediate onset of emission ("thresholdless" behavior), and the saturation and eventual quenching of the output. The saturation can be attributed to the recycling process being limited by the atomic decay rates, whereas the output reduction at high I_3 is possibly due to the splitting of the pumped excited state $F = 3'$ by the Autler-Townes effect, although this is still under investigation.

Our actual experiment is somewhat more complex than indicated by the simple drawing in Fig. 5.1, with many of the technical aspects described in more detail in Refs. [27, 26, 25]. The principal cQED parameters of our system are $g_0/2\pi = 16$ MHz, $\kappa/2\pi = 4.2$ MHz, and $\gamma/2\pi = 2.6$ MHz, where g_0 is based upon the reduced dipole moment for the $6S_{1/2}, F = 4 \leftrightarrow 6P_{3/2}, F' = 3'$ transition in atomic Cs. Strong coupling is thereby achieved ($g_0 \gg (\kappa, \gamma)$), resulting in critical photon and atom numbers $n_0 \equiv \gamma^2/(2g_0^2) \simeq 0.013$, $N_0 \equiv 2\kappa\gamma/g_0^2 \simeq 0.084$. The atom is trapped in the cavity with a far-off-resonance trap (FORT) [47], which is matched to a TEM_{00} mode along the cavity axis, with wavelength $\lambda_F = 935.6$ nm. For all experiments herein, the trap depth is $U_0/k_B = 2.3$ mK (47 MHz). The FORT has the additional feature that the potential for the atomic center-of-mass motion is only weakly dependent on the atom's internal state [27]. Another set of fields (designated by $\Omega_{3,4}$ in Fig. 5.1(b)) propagate in the plane transverse to the cavity axis and illuminate the region between the cavity mirrors, and are used not only for the pumping scheme described above, but also for cooling in the trap-loading phase. Each $\Omega_{3,4}$ beam consists of two orthogonal pairs of counter-propagating beams in a $\sigma^+ - \sigma^-$ configuration. In the pumping stage of the experiment, the fields are tuned 10 MHz blue of $F = 3 \rightarrow F' = 3'$ in the case of the Ω_3 beams and 17 MHz blue of $F = 4 \rightarrow F' = 4'$ in the case of the Ω_4 fields. The cavity length is actively stabilized with an auxiliary laser at wavelength $\lambda_C = 835.8$ nm that does not interfere with the trapping or the cavity QED (cQED) interactions. The detuning between the $3' \rightarrow 4$ transition at ω_{43} and the cavity resonance ω_C is $\Delta_{CA} \equiv \omega_C - \omega_{43} = 2\pi \cdot 9$ MHz. These detunings are chosen operationally in a trade-off between achieving a large cavity output flux from the $3' \rightarrow 4$ transition while maintaining a reasonable lifetime for the trapped atom despite heating from the various fields [67].

We start our experimental protocol by releasing a cloud of atoms from a magneto-optical trap

(MOT) above the cavity. The $\Omega_{3,4}$ beams are then used as cooling beams (with independent settings of intensity and detuning) to load an atom into the FORT [27]. About 10 atoms transit the cavity mode after each MOT drop, and the loading efficiency is set such that an atom is loaded into the FORT once every $3-10$ drops. We then switch the intensities and detunings of the transverse fields $\Omega_{3,4}$ to the pumping configuration and record the cavity output by way of the single-photon detectors $D_{1,2}$ shown in Fig. 5.1. Each photoelectric pulse from $D_{1,2}$ is stamped with its time of detection (1 ns resolution) and then stored for later analysis. Two examples of the resulting output counts versus time are shown in Fig. 5.3. By averaging traces such as these, we arrive at an average signal level versus time, as shown in the inset to Fig. 5.3(a). Typical lifetimes for a trapped atom in the presence of the driving $\Omega_{3,4}$ fields are $50-100$ ms, which should be compared to the lifetimes of $2-3$ s recorded in the absence of these fields [27]. Significantly, the approximately exponential decay of the signal with time does not result from a time-dependent diminution of the flux from single trapped atoms, but rather from the average of many events each of a variable duration. That is, for a given set of external control parameters, we observe a reasonably well-defined output flux over the time that an atom is trapped.

For a fixed set of operating conditions, we collect a set of $60-300$ traces as in Fig. 5.3, determine the average output flux for each trace, and find the mean and variance, as well as the trap lifetime for the set. From the known propagation and detection efficiency $\xi = 0.05$ (intracavity photon to registered TTL output pulse at $D_{1,2}$), we translate these measurements to an inference of intracavity photon number $\bar{n}$ and associated uncertainty σ. Figure 5.4 displays a collection of such measurements for the mean intracavity photon number $\bar{n}$ as a function of pump intensity Ω_3^2 for fixed recycling intensity Ω_4^2. Unfortunately, it is difficult to calibrate accurately the intensities $I_{3,4} \equiv (\Omega_{3,4}/2\gamma)^2$ for the $\Omega_{3,4}$ beams at the location of the atom in the region between the cavity mirrors; indeed, we estimate that our knowledge of either intensity for the data in Fig. 5.4 is uncertain by an overall scale factor $\simeq 2$. However, we do know the ratio of intensities, and therefore plot the data in Fig. 5.4 as a function of the quantity $x \equiv (7/9)(I_3/I_4)$, where the dimensionless factor is needed because the two transitions have different dipole moments. For these measurements, we estimate that the incoherent sum of intensities of the four Ω_4 beams is about 50 mW/cm^2, which corresponds to $I_4 \sim 13$.

To describe these data, we incorporate a more complete set of atom and field states than the four-state model employed for Fig. 5.2. As described in Ref. [74], we employ quantum jumps simulations [97] based upon the full set of Zeeman states for each of the levels $F = 3, 4$ and $F' = 3', 4'$ shown in Fig. 5.1, for a total of 32 atomic states. We also include two cavity modes, one for each of two orthogonal polarizations with three Fock states for each $\{|0\rangle, |1\rangle, |2\rangle\}$, leading to a total Hilbert space dimension of 288. We do not attempt to model atomic motion within the FORT potential. Rather, we fix the cavity coupling $g(\vec{r})$ to some constant value g, and incorporate a simple model to

describe the polarization gradients.

A result from these simulations is shown as the full black curve in Fig. 5.4. We make no claim for detailed quantitative agreement, as the simulations are sensitive to the parameters in our model for the $\Omega_{3,4}$ polarizations. However, as discussed in Ref. [74], this effective polarization state is the only adjustable parameter in the absolute comparison of theory and experiment in Fig. 5.4. The simulations do support the conclusions that the range of coupling values g that contribute to our results is restricted roughly to $0.5g_0 \lesssim g \lesssim g_0$. Furthermore, the simulations yield information about the atomic populations, from which we deduce that the rate of emission from the cavity $\kappa\bar{n}$ exceeds that by way of fluorescent decay $3' \rightarrow 4$, $\gamma_{43'}\langle\sigma_{3'3'}\rangle$, by roughly tenfold over the range of pump intensity I_3 shown in Fig. 5.4.

In addition to measurements of $\bar{n}$ versus pumping rate, we have also investigated the photon statistics of the light emitted by the TEM_{00} mode of the cavity by way of the two single-photon detectors $D_{1,2}$ illustrated in Fig. 5.1. From the cross-correlation of the resulting binned photon arrival times and the mean counting rates of the signals and the background, we construct the normalized intensity correlation function (see the *Supplementary Information*)

$$g^{(2)}(\tau) = \frac{\langle : \hat{I}(t)\hat{I}(t+\tau) : \rangle}{\langle : \hat{I}(t) : \rangle^2} \ , \tag{5.1}$$

where the colons denote normal and time ordering for the intensity operators $\hat{I}$ [69]. Over the duration of the trapping events, we find no evidence that $\langle : \hat{I}(t) : \rangle$ is a function of t, although we do not have sufficient data to confirm quantitatively stationarity of the underlying processes.

Examples of two measurements for $g^{(2)}(\tau)$ are given in Fig. 5.5(a-d). In Fig. 5.5(a,b), we again have $I_4 \simeq 13$ and the pump intensity I_3 is set for operation with $x \simeq 0.17$ near the "knee" in $\bar{n}$ versus x, while in (c,d), the pump level is increased to $x \simeq 0.83$. Significantly, in each case these measurements demonstrate that the light from the atom-cavity system is manifestly quantum (i.e., nonclassical) and exhibits photon antibunching $g^{(2)}(0) < g^{(2)}(\tau)$ and sub-Poissonian photon statistics $g^{(2)}(0) < 1$ [69]. In agreement with the trend predicted by the four-state model in Fig. 5.2(d) (as well as by the full quantum jumps simulation), $g^{(2)}(0)$ increases with increasing pump intensity, with a concomitant decrease in these nonclassical effects.

Theoretical results for $g^{(2)}(\tau)$ from the full quantum jumps simulation are given in Fig. 5.5(e,f) for $x = 0.17$. The excess fluctuations $g^{(2)}(\tau) \gtrsim 1$ extending over $\tau \simeq \pm 2$ μs appear to be related to the interplay of atomic motion and optical pumping into dark states [67], as well as Larmor precession that arises from residual ellipticity in polarization of the intracavity FORT [27, 64].

The realization of this strongly coupled one-atom laser is significant on several fronts. From the perspective of the dynamics of open quantum systems, our system demonstrates the radical departures from conventional laser operation wrought by strong coupling for the quantized light-

matter interaction. On a more practical level, over the course of the time that an atom is trapped (which is determined in real time), our system provides an approximately stationary source of nonclassical light in a collimated, Gaussian beam, as has been anticipated in the literature on one-atom lasers [75, 77, 78, 79, 80, 82, 83, 84, 85], and which has diverse applications. Remaining technical issues in our work are to improve the modelling and measurements related to atomic motion, both within the FORT potential and through the polarization gradients of the $\Omega_{3,4}$ fields. We have employed our quantum simulations to calculate the optical spectrum of the light output, and have devised a scheme for its measurement.

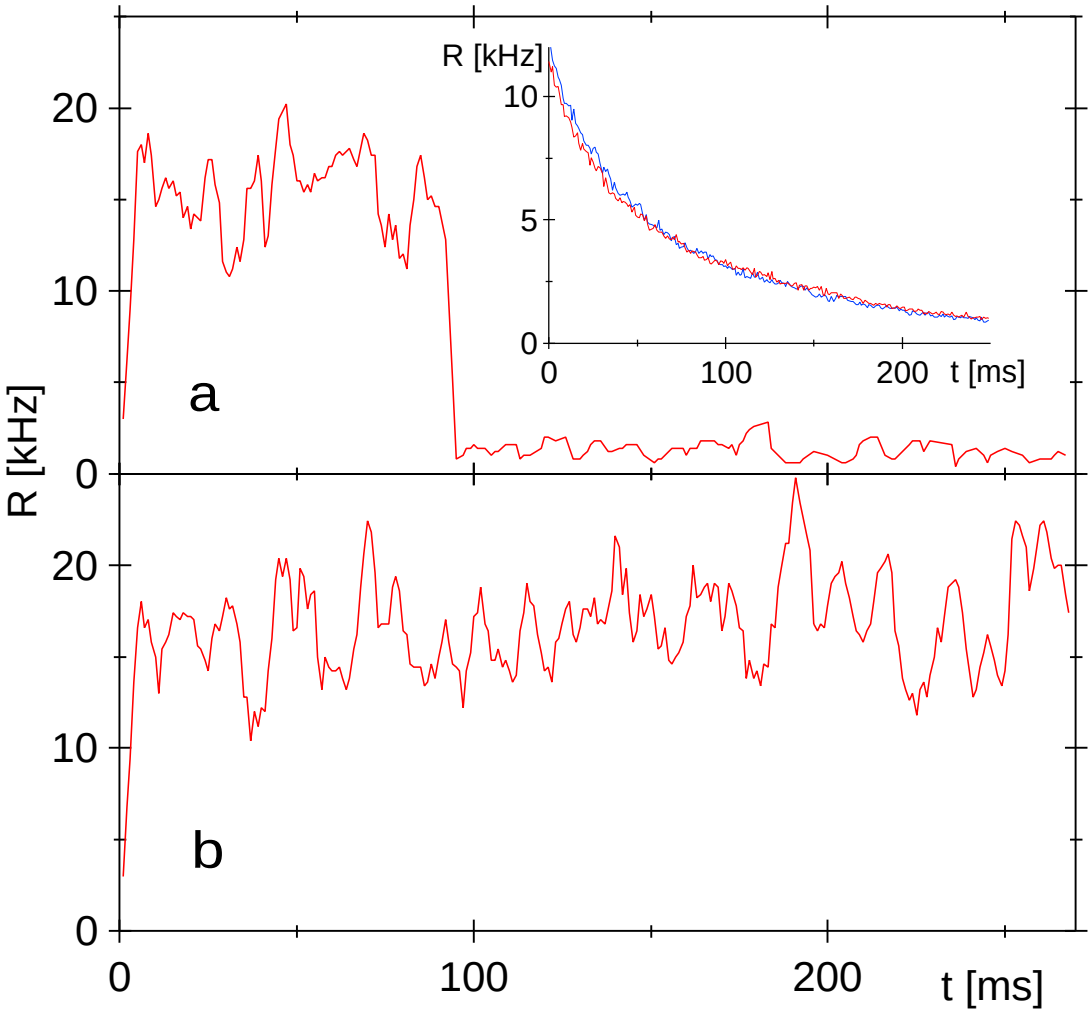

Figure 5.3: Total counting rate R recorded by detectors $D_{1,2}$ is displayed as a function of time for two separate trapped atoms, with the counts summed over 5 ms bins. At $t = 0$, the $\Omega_{3,4}$ fields are switched to predetermined values of intensity and detuning. In (a), the atom is trapped for $t \simeq 90$ ms before escaping, with then the background level due to scattered light from the $\Omega_{3,4}$ fields and detector dark counts shown as the residual. In (b), the atom (atypically) remains trapped for the entire observation cycle $\simeq 270$ ms and then is dumped. The inset in (a) displays R versus time obtained by averaging about 400 such traces. Two cases are shown; in one, the number of atoms delivered to the cavity mode has been diminished by about 2-fold. Since the curves are nearly identical, we conclude that cases with $N > 1$ atom play a negligible role. The overall detection efficiency $\xi = 0.05$ from intracavity photon to a detection event at $D_{1,2}$ is made up of the following factors: $\eta = 0.60$ cavity escape efficiency, $T = 0.50$ for only mirror M_2 output, $\zeta = 0.33$ propagation efficiency from M_2 to $D_{1,2}$, $\alpha = 0.5$ detection quantum efficiency at $D_{1,2}$.

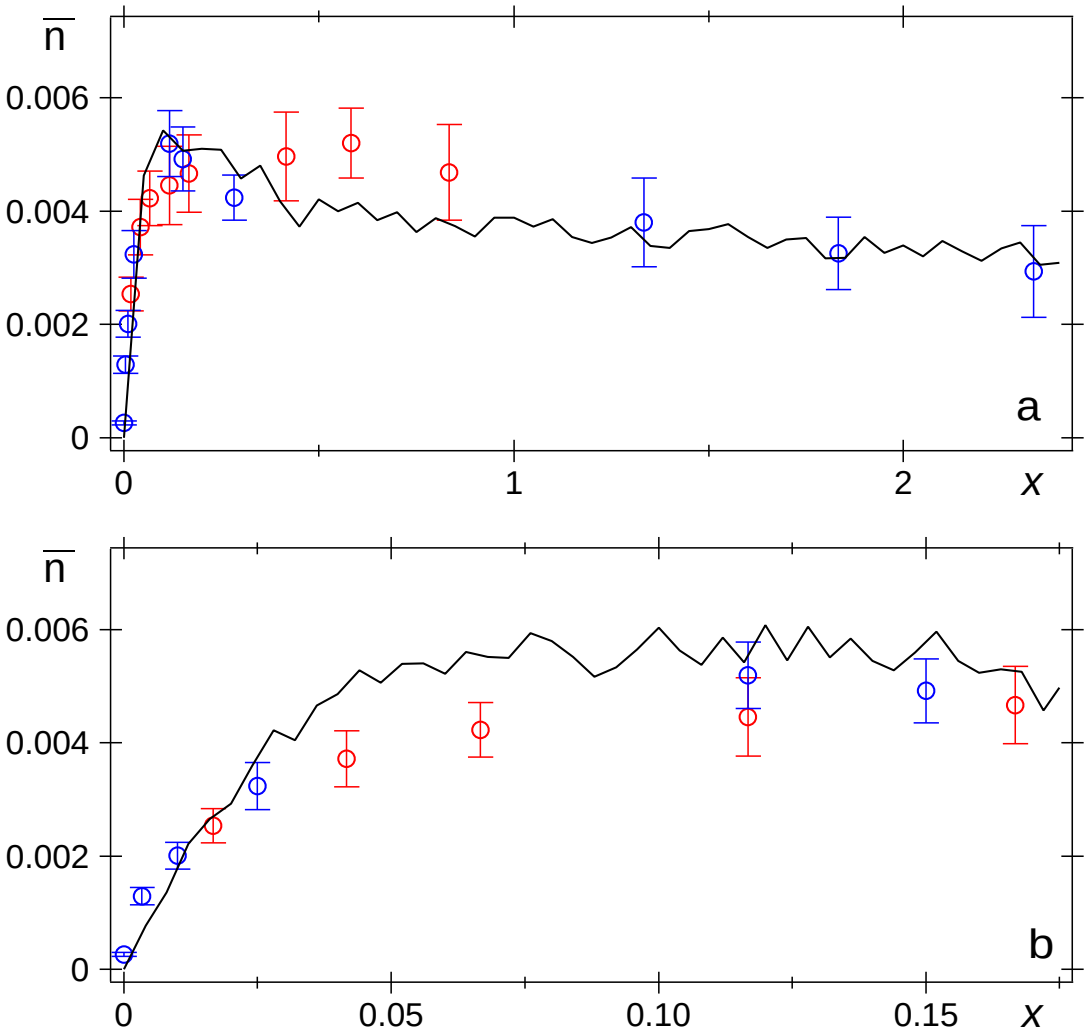

Figure 5.4: (a) The intracavity photon number $\bar{n} \pm \sigma_n$ inferred from measurements as in Fig. 5.3 is plotted as a function of pump intensity $x \equiv (7/9)(I_3/I_4)$ for fixed $I_4 = 13$. (b) An expanded scale displays $\bar{n}$ for small x. The immediate onset of emission supports the conclusion of "thresholdless" lasing. The two independent sets of measurements (red and blue points) agree reasonably well. The black trace in (a,b) is a theoretical result from a quantum jumps simulation of the experiment as described in the text.

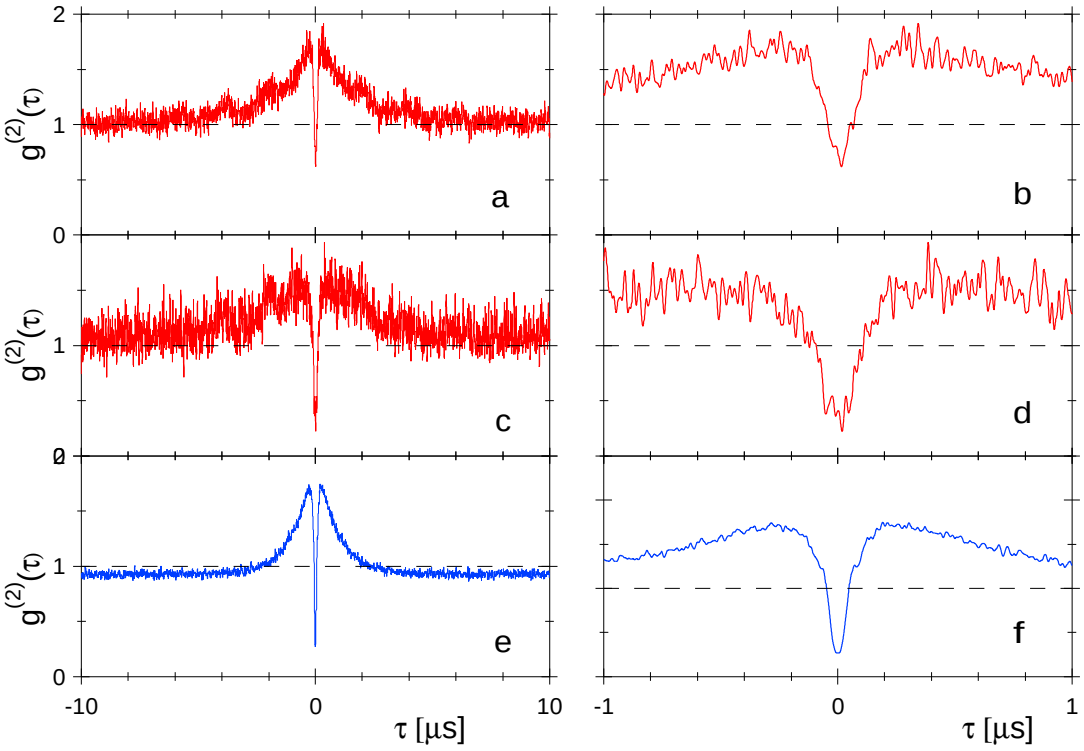

Figure 5.5: The intensity correlation function $g^{(2)}(\tau)$ is given for two operating conditions of the one-atom laser in (a-d), while (e,f) are theoretical results from a quantum jumps simulation. All traces have been "smoothed" by convolution with a Gaussian function of width $\sigma = 5$ ns.

Chapter 6

Deterministic Single-Photon Generation

This chapter is organized with the first section reproduced from the paper "Deterministic Generation of Single Photons from One Atom Trapped in a Cavity," (Ref. [36]). The remaining sections contain various additional details, including the contents of the Supporting Online Material from Ref. [36].

6.1 Main results

A crucial building-block for quantum information science is a deterministic source of single photons that generates one-quantum wavepackets in a well controlled spatiotemporal mode of the electromagnetic field. For example, protocols for the implementation of quantum cryptography [98] and of distributed quantum networks rely on this capability [22], as do models for scalable quantum computation with single-photon pulses as flying qubits [99, 18, 100, 101].

The earliest observations of single-photon emission used the fluorescent light from single atoms in two- and three-level configurations [102, 103, 104], and thereby produced light with manifestly quantum or nonclassical character. Fluctuations in the number of atoms provided inherent limitations to these original schemes, and have since been mitigated by isolating single ions [105] and molecules [106, 107], and by employing individual quantum dots [108, 109] and color centers [110, 111].

With a single dipole, pulsed excitation allows for "triggered" emission of a single photon within a prescribed interval, albeit into 4π steradians. To achieve emission as a directed output with high efficiency, the dipole emitter can be placed inside an optical resonator, as by coupling single quantum dots to microcavities [112, 113, 114]. These experiments employ the Purcell effect to enhance radiative decay into a cavity mode of interest and thereby achieve a deterministic bit stream of single photon pulses [115] in a regime of weak coupling in cavity quantum electrodynamics (cQED).

By contrast, the generation of single photons within the domain of strong coupling in cQED

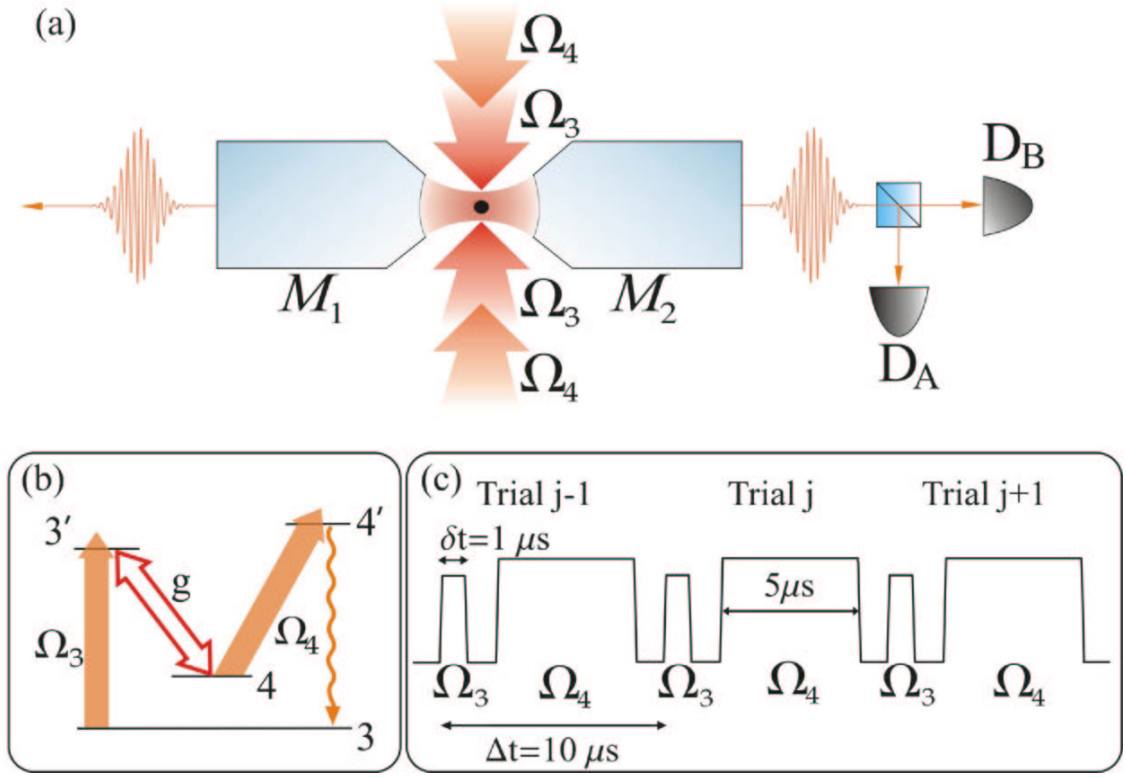

Figure 6.1: Illustration of the generation of single photons by one atom trapped in an optical cavity. (a) A single Cs atom is trapped in a cavity formed by the reflective surfaces of mirrors (M_1, M_2) and is pumped by the external fields (Ω_3, Ω_4) [27]. (b) The relevant atomic levels of the Cs D_2 line at 852.4 nm. Strong coupling at rate g is achieved for the transition $F' = 3' \rightarrow F = 4$ near a cavity resonance. (c) The timing sequence for the generation of successive single-photons by way of the $\Omega_{3,4}$ fields.

[66, 116] enables diverse new capabilities, including the reversible transfer of quantum states between atoms and photons as a fundamental primitive for the realization of quantum networks [22]. A single-photon source consisting of a trapped atom strongly coupled to an optical cavity represents an ideal node for such a network, in which long-lived internal atomic states can be mapped to quantum states of the electromagnetic field by way of "dark" eigenstates of the atom-cavity system [117]. By way of a quantum repeater architecture, converting stationary qubits to flying qubits in this way enables distributed quantum entanglement over long distances [22].

We report on the deterministic generation of single-photon pulses by a single atom strongly coupled to an optical cavity in a configuration suitable for quantum network protocols. Single Cesium atoms are cooled and loaded into an optical trap (Fig. 6.1A) which localizes them within the mode of a high-finesse optical cavity[26, 27, 25]. The atom is then illuminated by a sequence of laser pulses $\{\Omega_3^j(t), \Omega_4^j(t)\}$, the first of which $\Omega_3(t)$ drives a "dark-state" transfer between hyperfine ground states, $F = 3 \rightarrow 4$ (Fig. 6.1B, C). In this process, one photon is created in the cavity mode because the atomic transition $F' = 3' \rightarrow F = 4$ is strongly coupled to the cavity field with

rate g [117, 22]. The emitted photon leaves the cavity as a freely propagating, spatially Gaussian wavepacket whose temporal profile is determined by the external field $\Omega_3(t)$ [117, 115, 22]. The atom is then recycled back to the original ground state by a second laser pulse $\Omega_4(t)$, and the protocol repeated for subsequent single-photon generations.

The lifetime for a trapped atom in the presence of the driving $\Omega_{3,4}$ fields is $\tau_{trap} \simeq 0.14$ s, which should be compared to the repetition period $\Delta t = 10$ μs for single-photon generation and to the lifetime of 3 s recorded in the absence of the $\Omega_{3,4}$ fields [27]. Given our measured overall efficiency $\alpha = (2.4 \pm 0.4)\%$ for escape from the cavity, for propagation, and for photodetection, this means that on average, we generate (detect) about 1.4×10^4 (350) single-photon pulses from each trapped atom (see Section 6.2.6.3 below for additional details).

The Gaussian beam emerging from the cavity mirror M_2 is directed to a beam splitter and then to two photon-counting detectors (D_A, D_B). For each atom k, photoelectric pulses from $D_{A,B}$ which occur during the trapping interval are stamped with their time of detection (with $\delta = 2$ ns time resolution) and recorded for later analysis. An example of the pulse shape for single-photon generation is shown (Fig. 6.2A) over the detection window $[t_0^j, t_0^j + \delta t]$ within which the control field $\Omega_3^j(t)$ is ON, where $\delta t = 1$ μs, and t_0^j is the onset of $\Omega_3^j(t)$. The histogram of the total counts $n(t)$ from both detectors $D_{A,B}$, binned according to their delay with respect to t_0^j, is a sum over all repeated trials $\{j\}$ of the generation process from all atomic trapping events $\{k\}$. For the particular choice of $\Omega_3(t)$ employed here, single-photon pulses have duration $\tau \simeq 120$ ns (FWHM). The extended tail for $n(t)$ likely arises from generation attempts for which the atom resides in Zeeman sublevels that are weakly coupled to the control field at the beginning of the $\Omega_3(t)$ pulse [35, 74], as well as from roughly twofold variations in the coupling coefficient $g(\vec{r})$ [118]. Qualitative agreement of this measured pulse shape has been obtained with multi-level quantum Monte Carlo simulations [74].

To investigate the quantum character of the emitted field, we calculate the function $C(\tau)$ obtained by cross-correlating the photoelectric counting events from the detectors $D_{A,B}$ as a function of time separation τ (Fig. 6.3, also see Sections 6.2.4 and 6.3.2) . The large suppression of $C(\tau)$ around $\tau = 0$ strongly supports the nonclassical character of the light pulses emitted by the atom-cavity system. The likelihood of two photons being detected within the same trial is greatly reduced relative to that for detection events in different trials.

Suppression of two-photon events is also quantified by the time dependence of the photon statistics over the course of the pulse (Fig. 6.2B, C). Fig. 6.2B displays the integrated probabilities for single $P_1(t)$ and joint $P_2(t)$ detection events for times t after the onset t_0^j of the control pulse $\Omega_3^j(t)$, with $P_2(t)$ normalized to $P_1(t)/2$. We calculate $P_1(t)$ and $P_2(t)$ for an effective single detector without dead time or after-pulsing, and define $P_{1,2} \equiv P_{1,2}(\delta t)$. Over the duration of the control pulse $0 \leq t \leq \delta t$, $P_1(t)$ rises to a final value $P_1 = 0.0284$; that is, the probability to register a single photoelectric event in a trial is 2.84%. The lower trace in Fig. 6.2B quantifies the suppres-

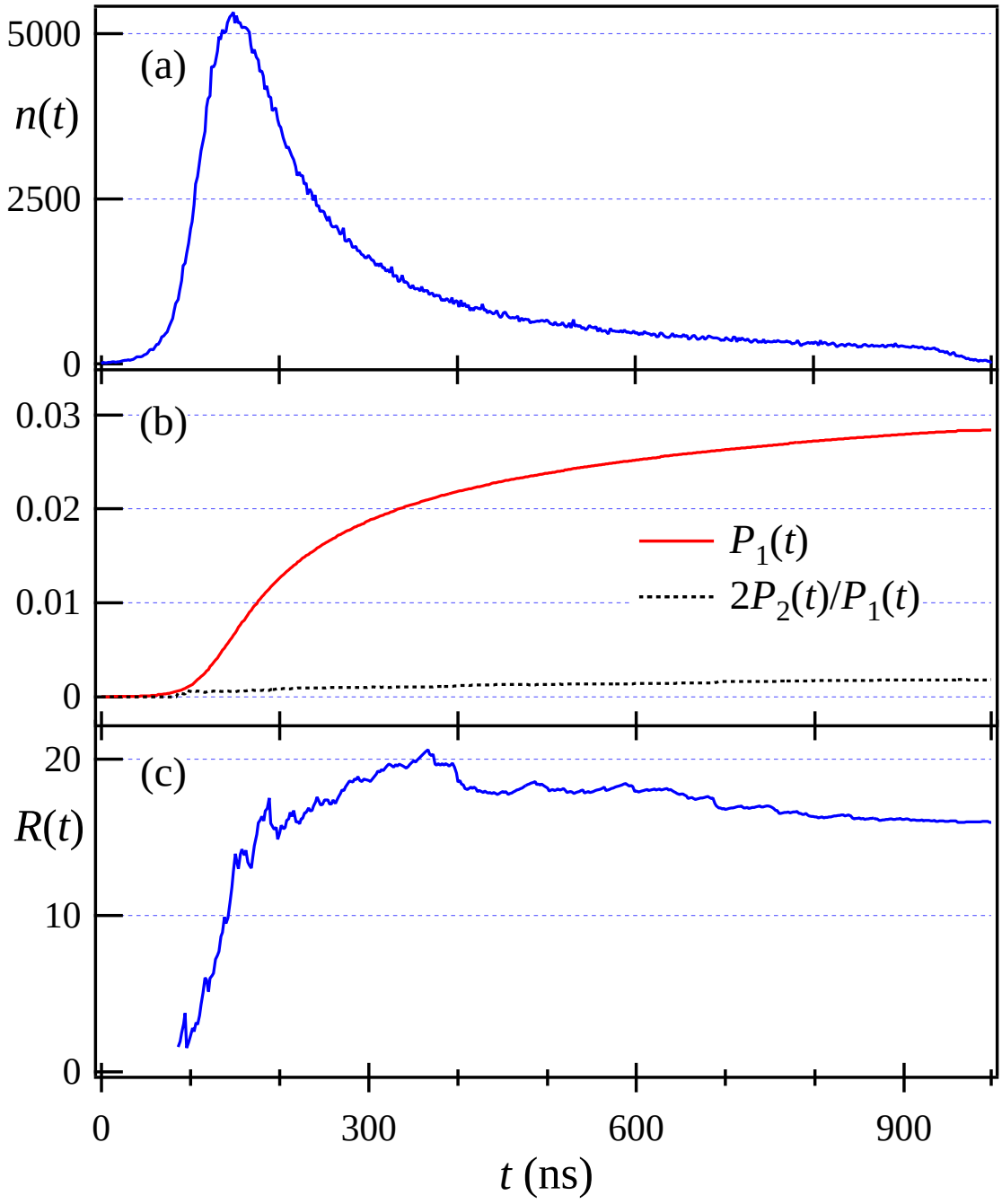

Figure 6.2: (a) Total histogram of photoelectric detection events $n(t)$ from both detectors $D_{A,B}$. In all cases, the control field $\Omega_3(t)$ is initiated at time $t = 0$ with rise time 100 ns. (b) The integrated probability $P_1(t)$ for a single photoelectric event and ratio $2P_2(t)/P_1(t)$, where $P_2(t)$ is proportional to the integrated coincidence probability for joint detections from $D_{A,B}$. Note for a coherent state, the two traces would overlap. (c) The ratio $R(t) = \frac{P_1^2(t)}{2P_2(t)}$ versus time, which indicates as high as 20-fold suppression of coincidences relative to a Poisson process.

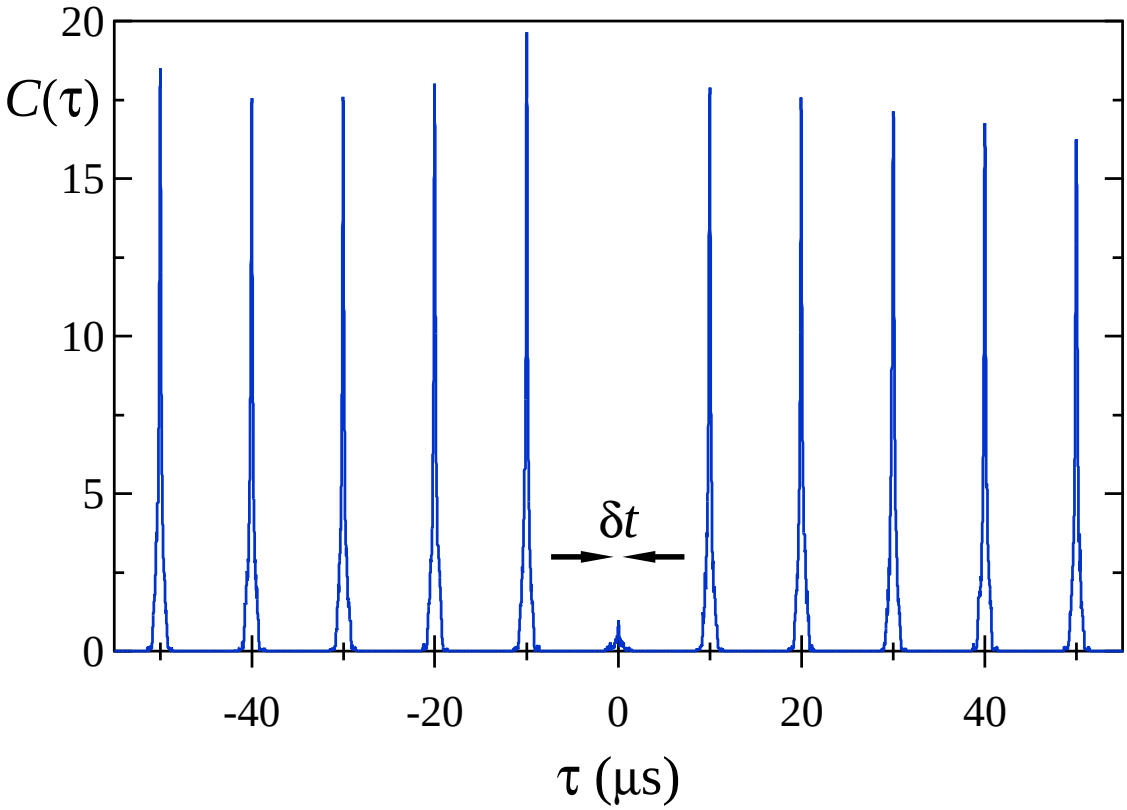

Figure 6.3: Time-resolved coincidences $C(\tau)$ as a function of delay τ between detections at $D_{A,B}$. Around $\tau = 0$, $C(\tau)$ is suppressed for two events from the same trial relative to its values for $\tau = j\Delta t$ for two events from different trials, where $j = \pm 1, 2, \ldots$. As indicated in Fig. 6.1(c), $\Delta t = 10$ μs is the repetition interval for the generation of single photons and $\delta t = 1$ μs is the duration of our control pulse $\Omega_3(t)$.

sion of joint detection events relative to that expected for a weak coherent state, which would have $2P_2(t)/P_1(t) \approx P_1(t)$ (as we have confirmed in separate measurements). By the end of the control pulse, $2P_2/P_1$ has reached the value 1.8×10^{-3}, which represents a 16-fold suppression of joint detection events relative to a Poisson process.

Fig. 6.2C examines the ratio $R(t) \equiv \frac{P_1^2(t)}{2P_2(t)}$, where $R \approx 1$ for a weak coherent state and increases with suppression of two-photon events. Significantly, R is independent of propagation and detection losses for $P_1 \gg P_2$. The trace in Fig. 6.2C restates the result that two-photon events are greatly suppressed relative to a coherent state, namely, $R \equiv R(\delta t) = 15.9 \pm 1.0$. Also note that in Fig. 6.3, the average area of the large peaks in $C(\tau)$ around $\tau = j\Delta t$ should exceed that of the central peak around $\tau = 0$ by a factor of about R, which we have confirmed.

The background rate during the Ω_3 drive pulses is time-independent, and can be obtained from the record of photoelectric detections when no atom is trapped. The measured background count probability is $P_B = 2.7 \times 10^{-4}$ for the entire window, of which $P_D = 0.82P_B$ comes from detector dark counts, and the rest from various sources of scattered light. For an ideal single-photon source,

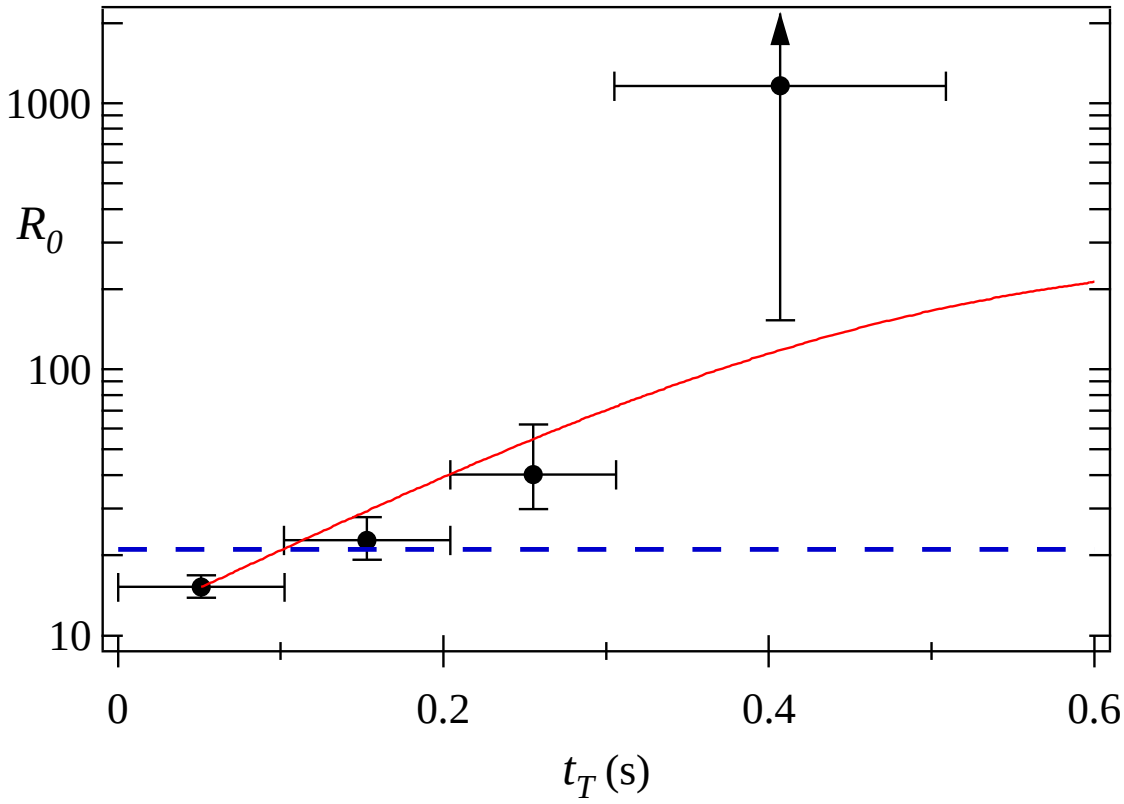

Figure 6.4: Evolution of the ratio $R_0 \equiv \frac{P_1^2}{2P_2}$ versus trapping time t_T, here corrected for detector dark counts. The data points are experimentally determined as discussed in the text, with horizontal error bars indicating the bin widths in t_T, and vertical bars based on counting statistics of coincidence events. The full curve is the prediction from our model calculation that includes (rare) two-atom events. The dashed line represents the measured overall average of R_0 for all t_T.

coincidence events at $D_{A,B}$ in the same trial would arise only because of background counts, since the source never emits two photons in one trial. Using the known values of $P_1(t)$ and P_B, the background-limited value $R_B(t)$ for this idealized scenario can be predicted. Our measured values are actually lower than this prediction ($R_B \equiv R_B(\delta t) = 52.5$), indicating a significant rate of excess coincidences.

These excess coincidences most likely arise from rare events with two atoms trapped within the cavity. We test this hypothesis in Fig. 6.4 by noting that the two-atom population should decay at roughly twice the rate of the single-atom population (as we have confirmed in other measurements related to Fig. 4 in Ref. [27]). The probability P_2 for joint detection should therefore diminish as a function of duration of the trapping interval, with a corresponding increase in the ratio R, which is precisely the behavior evidenced in Fig. 6.4.

Operationally, we bin all our detection time-stamps according to their delay with respect to the trap-loading time ($t_T = 0$), and then compute photon statistics separately for each bin. Only 4 intervals in t_T are employed due to poor statistics for the coincidence counts, especially for large

t_T. The analysis is the same as for Fig. 6.2, but we concentrate on the value $R \equiv R(\delta t)$, at the end of the $\Omega_3(t)$ pulse window. Furthermore, the ratio R_0 plotted in Fig. 6.4 is obtained from R with the contribution from the measured dark-count probability P_D removed, thereby providing a characterization of the atom-cavity source that is independent of the dark counts for our particular detectors. The results clearly support the hypothesis that rare two-atom events are responsible for our excess of coincidences.

Also shown in Fig. 6.4 as the full curve is the result for R_0 from a model calculation that assumes that a fraction η_I of our data is acquired with a single trapped atom, and that a fraction $\eta_{II} = 1-\eta_I$ has two atoms trapped, with η_I, η_{II} functions of the time t_T within the trapping interval. The correspondence between the model and our measurements supports the conclusion that excess coincidences arise from rare events with two atoms loaded into the trap. From this model, we infer that (i) approximately 3% of the trials are taken with two trapped atoms, and (ii) the generation of single photons succeeds with probability consistent with unity, $\phi_G = 1.15 \pm 0.18$ as constrained by our absolute knowledge of the various efficiencies. Further discussion of this model can be found in Section 6.2.6 below.

Given our ability to distinguish multi-atom trap loading events in real time (as demonstrated in Fig. 4 of Ref. [27]), events with $N \geq 2$ atoms trapped in the cavity could be actively discarded, or alternatively the extra atoms could be heated out of the trap, before even attempting single-photon generation. Moreover, in its current implementation, our atom-cavity system generates unpolarized single photons, with then a well defined polarization subsequently selected with 50% efficiency. This efficiency could be greatly improved by separating the functions of cooling and of single-photon generation for the Ω_3 control field, with the atom optically pumped into a known Zeeman sublevel before excitation. This separation of function would allow the interaction configuration of Ref. [118] to be implemented, making the pulse shape and phase for the photon wavepackets insensitive to randomness of the atomic position.

We have employed a single atom trapped within a high-finesse optical cavity as an efficient source for the generation of single photons on demand. The photons are emitted as a Gaussian beam with user-controlled pulse shapes. As documented in Fig. 6.4, two-photon events are suppressed by a factor $R_0 = 20.8 \pm 1.8$ relative to a weak coherent state, while $R_0 \geq 150$ for single-photon generation at long trapping times $t_T \simeq 0.4$ s. With this large suppression of two-photon probability, the Mandel-Q parameter is determined almost exclusively by propagation efficiency. For example, for polarized (unpolarized) photon wavepackets, $Q = -0.34 \pm 0.05$ ($Q = -0.68 \pm 0.10$) referenced to the total cavity output from (M_1, M_2). Absent passive losses from the cavity boundaries, the generation of single photons succeeds with probability close to unity, where this high success probability derives from the near ideal nature of the atom-cavity interaction in a regime of strong coupling.

6.2 Additional details

6.2.1 Experimental configuration

Our experimental setup is depicted by the simple drawing in Fig. 6.1A, with many of the technical aspects described in more detail in Refs. [26, 27]. After releasing a cloud of atoms from a magneto-optical trap (MOT) above the cavity, transverse cooling beams illuminate the cavity region, at which point an atom can be loaded into the intracavity far-off resonance trap (FORT), which is matched to a standing-wave, TEM_{00} mode along the cavity axis. The trap depth is $U_0/k_B = 2.3$ mK (47 MHz), and because its wavelength is $\lambda_F = 935.6$ nm, the potential for the atomic center-of-mass motion is only weakly dependent on the atom's internal state [27]. The cavity length is actively stabilized with an auxiliary laser at wavelength $\lambda_C = 835.8$ nm that does not interfere with the trapping or the cQED interactions. Relevant cavity parameters are length $l_0 = 42.2$ μm, waist $w_0 = 23.6$ μm, and finesse $\mathcal{F} = 4.2 \times 10^5$ at 852 nm.

For our system, the Rabi frequency $2g_0$ for a single quantum of excitation is given by $g_0/2\pi = 16$ MHz, where g_0 is based upon the reduced dipole moment for the $6S_{1/2}, F = 4 \leftrightarrow 6P_{3/2}, F' = 3'$ transition in atomic Cs (Fig 1B). The amplitude decay rates (κ, γ) due to cavity losses and atomic spontaneous emission are $\kappa/2\pi = 4.2$ MHz, and $\gamma/2\pi = 2.6$ MHz. Since $g_0 \gg (\kappa, \gamma)$, strong coupling is achieved, resulting in critical photon and atom numbers $n_0 \equiv \gamma^2/(2g_0^2) \simeq 0.013$, $N_0 \equiv 2\kappa\gamma/g_0^2 \simeq 0.084$.

With an atom loaded into the intracavity FORT, our protocol for the generation of single-photon pulses consists in illuminating the atom with a sequence of laser pulses according to the timing diagram shown in Fig. 6.1C of the paper. Within each trial, the first pulse $\Omega_3(t)$ contains light tuned 10 MHz blue of $F = 3 \rightarrow F' = 3'$, which initiates the adiabatic transfer $F = 3 \rightarrow 4$ between the ground hyperfine levels, with the emission of a photon into the cavity mode. This transformation is principally accomplished via "dark" eigenstates of the atom-cavity system, with no contribution from the excited level $F' = 3'$, and hence with a concomitant reduction of fluorescent loss [117, 21, 119]. The second pulse $\Omega_4(t)$ is tuned 17 MHz blue of $F = 4 \rightarrow F' = 4'$ and recycles the atom back to the $F = 3$ ground state through spontaneous decay $F' = 4' \rightarrow F = 3$. Each $\Omega_{3,4}$ field consists of two orthogonal pairs of counter-propagating beams in a $\sigma^+ - \sigma^-$ configuration. The detuning between the $3' \rightarrow 4$ transition at ω_{43} and the cavity resonance ω_C is $\Delta_{CA} \equiv \omega_C - \omega_{43} = 2\pi \times 9$ MHz [35].

We now provide some additional details on the optical path from the cavity to the detectors. After emerging from the vacuum chamber window, the path includes a polarizing beam splitter (PBS), an optically pumped Cs cell that filters out scattered Ω_3 light, several dichroic mirrors and two interference filters. The light is next coupled into a single-mode fiber, and then split using a 50/50 fiber coupler. The two output fibers of the coupler are connected to fiber-coupled avalanche photodiodes (APD), labelled D_A and D_B.

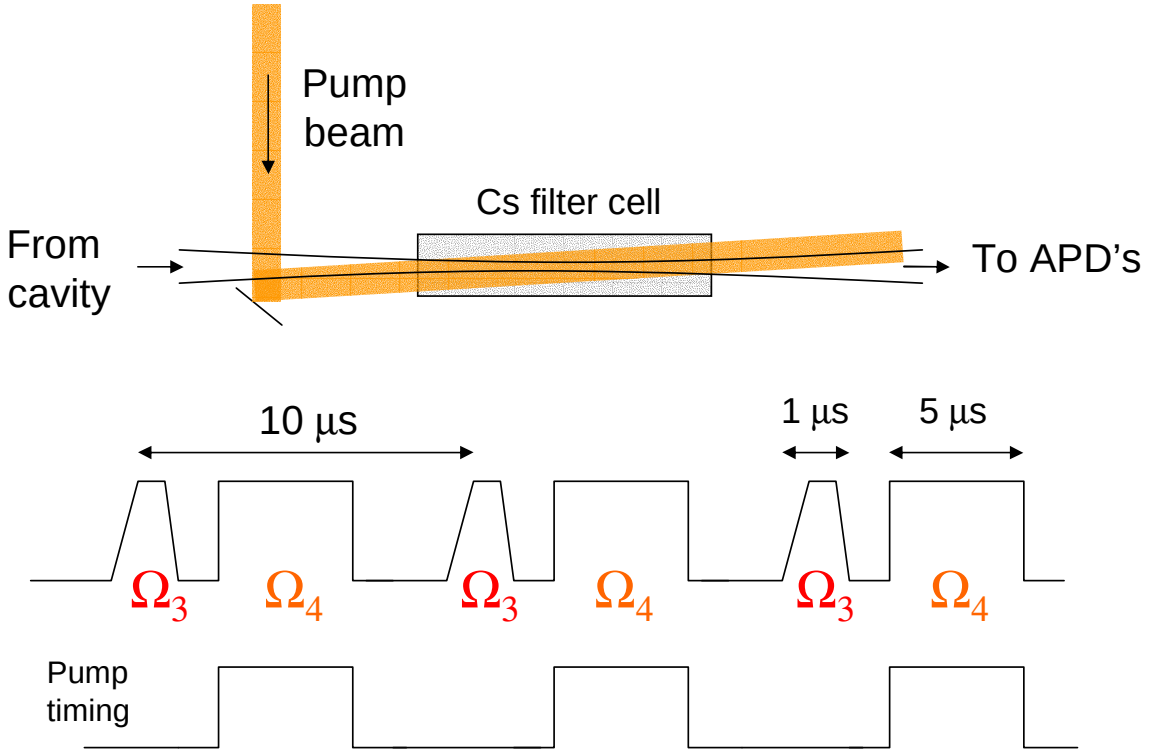

Figure 6.5: Configuration and timing diagram for the Cs filter cell used in the experiments on single-photon generation. The pump beam, near resonance with the Doppler broadened $6S_{1/2} \rightarrow 6P_{3/2}$, $F = 4 \rightarrow F'$ transition in Cs, typically had 5 to 10 mW of power, in a beam of ≈ 1 cm diameter, directed through the cell tilted a few degrees from its axis. The timing diagram (lower part) illustrates how the optical pumping of the cell took place simultaneously with the Ω_4 recycling light being delivered to the cavity mode region.

Most of the optical elements along the path just described require no further explanation, but the optically pumped Cs cell does warrant a brief additional discussion[1]. As has been extensively documented in this chapter, one of our main experimental challenges in the generation of single photons was the elimination of background light on the detectors. When we first started this experiment without the filter cell, one of our main sources of background counts was Ω_3 pump light presumably scattering off the mirror substrates and into the cavity output path. The reason we concentrated on reducing counts from the Ω_3 beams is that this light is on during the production window for single photons. Although the rate of background counts from Ω_3 would fluctuate, and of course depended on the Ω_3 power, we would typically observe rates giving probabilities $P_B \approx 7\times10^{-4}$ in the 1 μs window (this was reduced to $P_B = 2.7 \times 10^{-4}$ in the published experiment).

The basic principle of using a Cs vapor cell is that by optically pumping all the atoms into one hyperfine ground state (in our case $F = 3$) the cell is a very strong absorber of light near resonance with the $F = 3 \rightarrow F'$ transitions (within the Doppler broadened profile). Additionally, and crucially,

[1] Within the Quantum Optics group, these Cs filter cells were first used in the experiments of Kuzmich *et al.* [120]

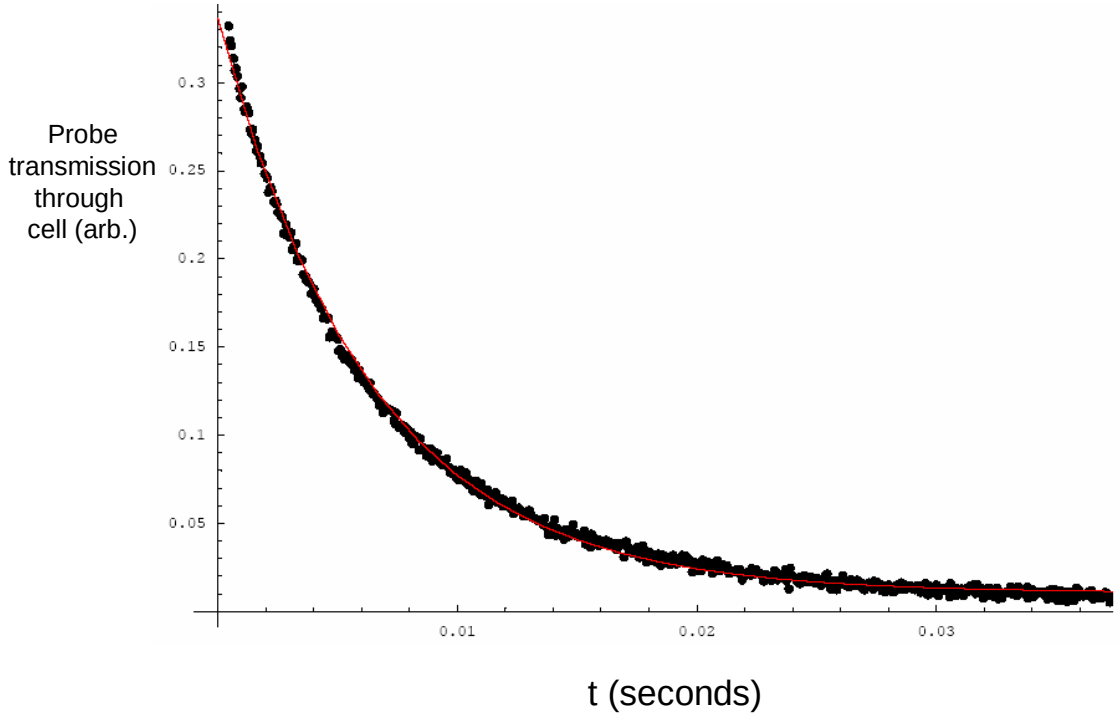

Figure 6.6: A measurement of the depolarization time of the coated Cs filter cell. The pump beam is switched off at $t = 0$. As the atoms depump via collisions with the walls, the transmission of the probe beam (plotted points) decreases. A fit to the data (curve) gives an exponential time constant $\tau_{cell} = 6.3$ ms.

light near resonance with the $F = 4 \rightarrow F'$ transitions transmits with high efficiency (in our case around 90%). The cell can thus be configured as an absorptive filter for light on either the trapping or repumping transition in Cs, with a "stop-band" of width roughly set by the Doppler profile. Once optical pumping is performed however, the hyperfine states do depolarize on some timescale due to collisions with the walls of the cell. For this reason the walls of the cell are coated such that the hyperfine relaxation time is extended to about 6 ms (as documented by our own measurements, see Fig. 6.6). The approach to be taken was to pump the cell once per 10 μs cycle, outside the Ω_3 window. Therefore the 6 ms relaxation timescale was adequate for our purposes.

Our implementation of the filter cell is depicted in Fig. 6.5. A few technical considerations are worth mentioning since it took some time and effort to converge on an acceptable configuration. One issue we had to confront was the question of propagation direction for the pump beam. The choice of pump co-propagating with cavity output presented the possibility of large count rates at the APD's, possibly dangerously high levels for the detectors. Alternatively, a counter-propagating geometry meant having this bright pump beam directed toward the physics cavity (although not exactly aligned, small amounts of power can cause problems if coupled into the cavity mode). As it turned out (and as illustrated in Fig. 6.5) we decided on the co-propagating option. We managed

to reduce the detector count rates to around 50×10^3 s^{-1}, well below saturation and damage threshold levels of the APD's. Although it may seem that this level of detector counts was well below tolerable thresholds, it was important to get it down to this level or lower for the following reason. The switching was done with an acousto-optic modulator (AOM) whose extinction ratios are typically $10^3 - 10^4$. Since we needed well below 100 s^{-1} per detector when the pump was off, the requirements became much stricter. In order to deal with this problem we optimized the setup using the alignment of the pump, in addition to changing its polarization, taking advantage of a polarizer in the path to the detectors which then directed most of the pump light elsewhere. In addition to reducing the count rate via the direction of the pump beam, the timing of the pump pulse also had an impact on the background rates. Since the extinction ratio of an AOM is time-dependent, we also had to maximize the delay between the pump pulse and the Ω_3 pulse. After all these measures were taken to reduce residual pump-related counts while the AOM was switched off, we finally had low enough background to proceed with the experiment.

One other change had to be made to the setup as a result of the filter cell. The cavity output beam for all experiments in this lab prior to these ones was collimated at a very large diameter. Although I have no record of a documented quantitative measurement of this, its diameter was somewhere in the range of 5 to 10 mm. When the filter cell was first placed in the path of this large beam, it proved very difficult to achieve reasonable fiber coupling efficiency downstream. Presumably this was due to severe phase front and beam profile distortions caused by the faces of the cell. Implementing a telescope in the path such that the beam was much smaller ($\approx$ 1 mm) at the position of the cell greatly improved the fiber coupling.

6.2.2 Losses and efficiencies

Photons generated in the cavity are subject to various types of loss along their path to the detectors. These are summarized in Table 6.1.

Independent diagnostic measurements reveal the ratio of scattering/absorption losses to transmission of our cavity mirrors [59]. From this we infer the cavity escape efficiency α_e. Our cavity is also symmetric (nominally identical mirrors) meaning that 1/2 of the generated photons leave through the mirror M_1 and are not detected (α_{2s}). Once the light exits the vacuum chamber, the unpolarized stream of output photons is first reflected from the PBS, resulting in a 50% loss (α_{PBS}). The remaining optics, including the fiber coupling efficiency, on the way to the APD's gives the quantity α_P. The quantum efficiency α_{APD} of the APD's is also independently measured.

The uncertainty in α_e comes from the difficulties related to mode matching and scattering in the reflection dip measurement we used [59]. The efficiencies α_P and α_{APD} are obtained using measurements of the fiber transmission, which has fluctuations in our system of around $\pm$ 10%. The values and uncertainties enumerated in Table 6.1 combine to give a total efficiency of escape,

propagation and detection

$$\alpha = \alpha_e \times \alpha_{2s} \times \alpha_{PBS} \times \alpha_P \times \alpha_{APD} = 0.024 \pm 0.004. \tag{6.1}$$

From these efficiencies, their associated uncertainties and our measurements of photon statistics of the emitted light, we infer that each generation attempt succeeds with probability $\phi_G = 1.15 \pm 0.18$. The fact that we succeed with efficiency consistent with unity (within error) derives from the strong coupling of atom and cavity field.

Description	Symbol	Value	Error
Cavity escape	α_e	0.6	0.1
Two-sided cavity	α_{2s}	0.50	N/A
Polarizer	α_{PBS}	0.50	N/A
Propagation	α_P	0.32	0.03
Detection	α_{APD}	0.49	0.05
Total	α	0.024	0.004

Table 6.1: List of efficiencies associated with photon propagation and detection.

6.2.3 Determination of the presence of a trapped atom

For each attempt to load an atom into the FORT, we obtain an output stream of photoelectric events. The first step in the analysis of such an output stream is to determine whether an atom was indeed loaded into the trap. The procedure is as follows: we assume an atom is present at time t if more than n_p photons total were recorded during the W_d detection windows immediately prior to t. The result is not sensitive to the exact values of n_p and W_d; typical values are $n_p = 1 - 5$, $W_d = 500$ (i.e., 5 ms).

6.2.4 Calculation of $C(\tau)$

Counts recorded outside the gating intervals $[t_0^j - \frac{1}{2}\delta t, t_0^j + \frac{3}{2}\delta t]$ are removed from the record due to an excess of stray light between trials $\{j\}$. This occurs because of our use of an optically pumped Cs cell in the output path for the purposes of filtering residual scattered Ω_3 light (see Section 6.2.1). These records are then converted into a pair of lists $(a_1^k, \cdots, a_N^k)$ and $(b_1^k, \cdots, b_N^k)$ for detectors D_A and D_B, respectively. The n^{th} entry in each list is 1 if a photoelectric event was recorded in the time interval $[n\delta, (n+1)\delta]$, and zero otherwise, where δ is the time resolution of our data acquisition system. The correlation function is obtained by convolving the two lists against each other, and then convolving the result against a smoothing function $f(t) = (2\pi\sigma^2)^{-1/2} e^{-t^2/2\sigma^2}$, with $\sigma = 20$ ns:

$$C(\tau) = \sum_m f(\tau - m\delta) \sum_k \sum_n a_n^k b_{n+m}^k. \tag{6.2}$$

6.2.5 Photon statistics

Although in these experiments our desired state of the electromagnetic field was a fairly simple one (the single photon), it turned out that there were many counterintuitive and subtle issues to be considered when analyzing the data. The first issue at hand is that the statistics of photoelectric events do not necessarily allow us to deduce the state of the field in a straightforward fashion. The next task is to infer the properties of the cavity output field (and even the field generated inside the cavity) from the combination of photodetection data (measured "downstream") and known efficiencies along the optical path. This requires calculations of the effect of losses on the field state. Another consideration in our analysis was to infer what our statistics would have been in the hypothetical case of an idealized single detector (rather than our two imperfect detectors in the experiment). Dark counts are another concern in any photon counting experiment, so we developed the formalism to apply a correction to the data based on the independently measured dark count rate. Finally, we also considered what the possible impact could have been of neglecting three-event processes in our analysis, since our detection setup was only marginally able to detect such events.

6.2.5.1 Some basics of photoelectric detection

The data analysis for our experiment on single-photon generation presented an interesting challenge regarding the photon statistics. The measured quantities in the laboratory are photoelectric events recorded on two detectors after a nominal 50/50 beam splitter. The question is how to translate these data into information about the field at the input to the beam splitter (inference about the field further upstream is discussed below in Section 6.2.5.3). There are two issues at hand here: the first is how does the field state at a given point in space $\vec{r}$ relate to the photoelectric statistics from a detector at $\vec{r}$. The second issue relates to inferring properties of the field before the beam splitter from the data recorded on the two detectors.

As it turns out, there is no need to make statements about the state of the field itself in evaluating the data. The reason for this is that we can compare properties of the measured statistics (such as the quantity R) to their hypothetical values if our output field were a coherent state. The main characteristics of interest for a single-photon source are the efficiency and the suppression of two-photon events relative to that of a coherent state. Consequently for these evaluations it is possible to stay in the realm of photoelectric statistics without venturing into the somewhat subtle territory of inferring the field state.

In spite of this fact it is still crucial to write down a fundamental expression for the probability of photoelectric detection. For one detector, Equation (14.8-7) of Mandel and Wolf [69] tells us that

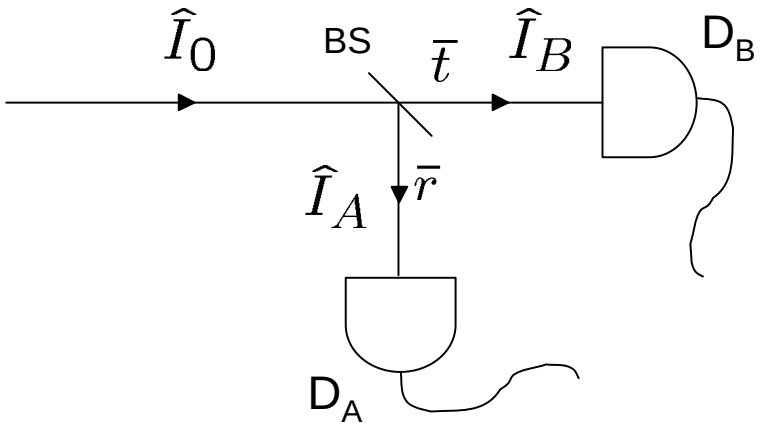

Figure 6.7: Schematic depiction of a field being split at a beam splitter (BS) and illuminating detectors $D_{A,B}$. The beam splitter has intensity reflection and transmission coefficients $\bar{r}$ and $\bar{t}$, respectively. The field modes are labelled by their respective intensity operators $\hat{I}_{0,A,B}$.

the probability of registering n photoelectric events in an interval $[t, t+T]$ is

$$p(n,t,t+T) = \left\langle \mathcal{T} : \frac{\hat{W}^n \exp\left(-\hat{W}\right)}{n!} : \right\rangle, \tag{6.3}$$

where $\hat{W} \equiv \int_t^{t+T} \alpha c S \hat{I}(t')dt'$, α is the detector quantum efficiency, S is its photosensitive area, $\hat{I}$ is proportional to a photon number operator of the form $a^\dagger a$, and the $\mathcal{T}$ and :: represent time and normal ordering, respectively. As the operator quantity is a Poisson distribution, it is not surprising that this formal expression leads to the well known fact that coherent states give Poisson-distributed photoelectric counting statistics. In the discussion that follows, however, we mostly assume that the intensities are low, such that the probability to register a single event at either detector $p(n,t,t+T) \ll 1$. In this limit, we can take the limit $\exp\left(-\hat{W}\right) \to 1$, and the expressions simplify. For many of our purposes this approximation is a good one, but in some cases the full expression is necessary.

6.2.5.2 Comparison of the data to a coherent state

I will first illustrate what I consider to be the simplest way to compare our data to coherent state properties. Specifically, we consider the hypothetical case of our cavity output field being a coherent state. This means that all we have to understand is how a coherent state is divided at a beam splitter, and the ensuing photoelectric statistics at the two detectors.

It is a well known result that the outputs of a beam splitter illuminated by coherent states are also coherent states (see Ref. [69], Section 12.12). Specifically, the coherent amplitudes of the output modes (A, B) in Fig. 6.7 are given by $|v_A|^2 = r|v|^2$ and $|v_B|^2 = t|v|^2$, where the input state has

amplitude v. For the purposes of this discussion the square moduli of these amplitudes are relevant because we are interested in photon counting rather than any phase-sensitive detection. Another useful and fundamental property of coherent states and this beam splitter transformation is that these output modes are completely uncorrelated [69]. In other words, the detection statistics at $D_{A,B}$ are independent of each other and dictated solely by the coherent amplitudes $v_{A,B}$. With the assumption of weak fields such that the probability of any photoelectric event is very small, the following simple result ensues (special case of weak coherent states):

$$P_c = P_1^{(A)} P_1^{(B)}. \tag{6.4}$$

Here, P_c is the probability to register an event at both detectors in the time window of interest, and $P_1^{(A,B)}$ are as usual the single event probabilities at $D_{A,B}$ in the same window of time. It is interesting to note that this expression is independent of the beam splitter ratio. We use the notation P_c for the *coincidence* probability rather than P_2 since the latter is reserved for the hypothetical case of an ideal single detector. These quantities also differ in value, as will be discussed below.

At this point it is already possible to do comparisons with single-photon data. By computing experimental single-photon and coincidence probabilities, strong violations of Equation 6.4 will indicate the quality of the photon source. More specifically, the signature is a strong suppression of coincidence probability relative to the product $P_1^{(A)} P_1^{(B)}$. The quantity R introduced earlier quantifies this very suppression, and can be equivalently written as $R = \frac{P_1^{(A)} P_1^{(B)}}{P_c}$.

The approach we decided to take for Ref. [36] was to consider the hypothetical case of an ideal single detector before the beam splitter. This allowed us to define quantities P_1 and P_2 (probabilities to register one and two events, respectively, on this fictitious detector) that seem intuitively closer to field properties than our two-detector data. The tasks then are to translate the data into this hypothetical scenario, and also to compute one- and two-event probabilities for a weak coherent state on one detector. This approach is slightly more involved than the previous analysis and the expressions are more complicated, since the results do depend on the beam splitter ratio.

The case of the coherent state illuminating a single detector (without dead time or afterpulsing) has a well-known solution, namely, that the photoelectric counting statistics are given by a Poisson distribution. There are several ways to derive this result, and different ways to physically interpret it, which we do not explore here in detail. Instead we refer again to chapter 14 of Mandel and Wolf [69], in particular Equation 14.8-14. Explicitly, for a coherent state the counting statistics in the interval of duration T are given by

$$p(n, t, t+T) = \frac{W^n e^{-W}}{n!}, \tag{6.5}$$

where $W = \alpha c S \int_t^{t+T} I(t')dt'$ and $I(t)$ is proportional to the square of the coherent amplitude

(allowed to vary in time). This expression directly gives the value of the ubiquitous ratio R (special case of the coherent state)

$$R = \frac{P_1^2}{2P_2} = e^{-W}, \tag{6.6}$$

where we have reverted to the more compact notation $P_n \equiv p(n, t, t+T)$. The weak field, low probability result of $R \to 1$ follows trivially.

The next step is to infer what happens at the ideal single detector in terms of the two-detector statistics. This must be done for an arbitrary state of the field, since we are applying it to our experimental situation. The singles rates are obtained quite trivially starting from Equation 6.3 (in the weak field limit $\exp(-\hat{W}) \to 1$) and are

$$P_1^{(A)} = \alpha c S \bar{t} \int_t^{t+T} dt' \langle : \hat{I}_0(t') : \rangle dt' \tag{6.7}$$

$$P_1^{(B)} = \alpha c S \bar{r} \int_t^{t+T} dt' \langle : \hat{I}_0(t') : \rangle dt'. \tag{6.8}$$

At this point we must write down the coincidence probability in the two-detector case in terms of the input mode $\hat{I}_0$, as well as the two-event probability for the fictitious single detector directly measuring $\hat{I}_0$. We now express the one-detector, two-event probability as follows:

$$P_2 = \frac{(\alpha c S)^2}{2} \int_t^{t+T} \int_t^{t+T} \langle : \hat{I}_0(t') \hat{I}_0(t'') : \rangle dt' dt''. \tag{6.9}$$

This is also derived from the general expression Equation 6.3, and we have again invoked the weak field limit. In the case of two detectors, we have

$$P_c = (\alpha c S)^2 \bar{r}\bar{t} \int_t^{t+T} \int_t^{t+T} \langle : \hat{I}_0(t') \hat{I}_0(t'') : \rangle dt' dt'', \tag{6.10}$$

since the operators inside the normal ordered expectation values transform in this case like $\hat{I}_A \to \bar{t}\hat{I}_0$, $\hat{I}_B \to \bar{r}\hat{I}_0$, where again $\bar{r}$ and $\bar{t}$ are the reflection and transmission coefficients of the beam splitter. Comparing Equations 6.9 and 6.10, we get the following expression relating the one- and two-detector cases:

$$P_2 = \frac{P_c}{2\bar{r}\bar{t}}\ . \tag{6.11}$$

This reduces to $P_2 = 2P_c$ for the case $\bar{r} = \bar{t} = \frac{1}{2}$. The next question though is how to determine $\bar{r}$ and $\bar{t}$ experimentally, since we did observe slightly unbalanced singles rates at $D_{A,B}$. The approach we took for the analysis in Ref. [36] was to infer $\bar{r}$ and $\bar{t}$ from the singles rates themselves. This seemed like a good way to obtain the relevant values, since it is effectively a measure of the ratio averaged over the actual time data was being taken. An independent measurement may have been desirable, but various count-rate observations over long periods of time (months) suggested that

deviations from 50/50 were consistently small, but did have some fluctuations ($|\bar{r}/\bar{t} - 1| < 10\%$). Defining $P_1^{(T)} \equiv P_1^{(A)} + P_1^{(B)}$, we obtain

$$P_2 = \frac{P_c \left(P_1^{(T)}\right)^2}{2P_1^{(A)} P_1^{(B)}} \tag{6.12}$$

assuming a lossless beam splitter $\bar{r} + \bar{t} = 1$. This was the formula used ("behind the scenes") to define P_2 for Ref. [36]. Although the two-detector analysis involves the quantity P_c (which differs by a factor of 2 from the possibly more intuitively accessible P_2) and also requires the individual singles rates at $D_{A,B}$, it does seem simpler than this one-detector fiction in hindsight, especially since the beam splitter ratio does not enter the calculation.

6.2.5.3 Effect of attenuation

One of the main data analysis tasks of our experiment on single-photon generation is to infer the properties of our source in the absence of the scattering and absorption losses the light suffers along the output path. In other words, we want to determine the quality of the photon gun "upstream" having independently measured the various efficiencies involved. These diverse loss mechanisms are described in detail in Section 6.2.2.

As shown in Fig. 6.8, propagation through a lossy medium with efficiency α (represented by the "blob" in part (a)) can be considered formally equivalent to a beam splitter with transmission coefficient α (part (b)). The other input mode of this fictitious beam splitter is in the vacuum state. Although it is of course possible to determine the full state of the electromagnetic field as it transmits through such a medium, our approach is somewhat simplified.

First of all, we are concentrating here on the photon statistics only, namely, the diagonal components of the density matrix written in the number state basis. Second, we are dealing with very weak fields and for the most part neglect photon numbers higher than 2. Consequently, the approach we take is to examine how moments of the photon number operator $\hat{n} = \hat{a}^\dagger \hat{a}$ (such as $\langle \hat{n} \rangle$, $\langle \hat{n}^2 \rangle$,...) transform upon transmission through a beam splitter. These moments relate trivially to the n-photon probabilities P_n, which are experimentally accessible:

$$\langle \hat{n}^q \rangle = \sum_n n^q P_n. \tag{6.13}$$

The fundamental starting point for this exercise is of course the beam splitter relation

$$\hat{a}_o = \sqrt{\alpha}\hat{a}_i + \sqrt{1-\alpha}\hat{a}_v \ , \tag{6.14}$$

where a_v is the "fictitious" vacuum input, α is the transmission coefficient for intensity/power, and

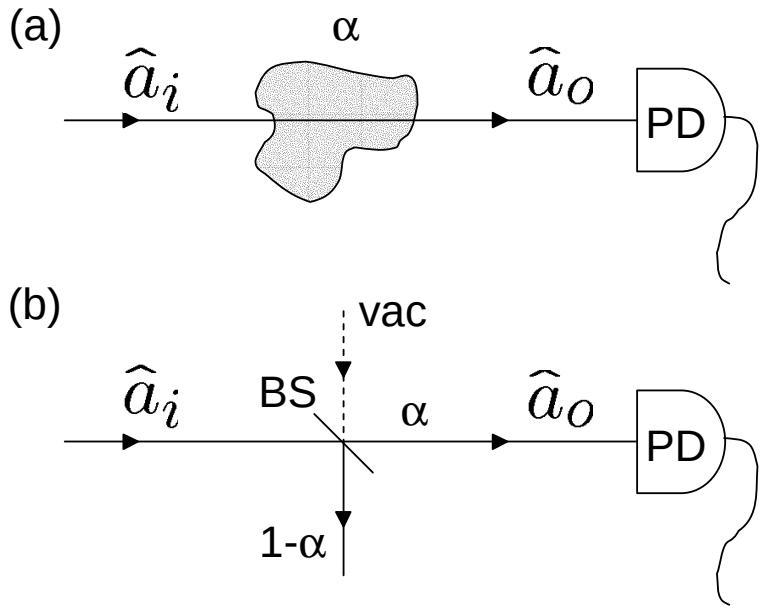

Figure 6.8: Schematic diagram illustrating the equivalence of propagation through a lossy medium (a) to transmission through a beam splitter (b). Input and output fields are symbolized by the annihilation operators $\hat{a}_i$ and $\hat{a}_o$, respectively. Output fields illuminate photodetectors (PD). The intensity transmission coefficient α applies to the lossy medium in (a) and to the beam splitter (BS) in (b).

we have only written the expression for one output mode. Using this expression for the output field in terms of the input, it is possible to compute the expectation values of any operator made up of $\hat{a}$'s and $\hat{a}^\dagger$'s, including of course the moments of $\hat{n}$ that interest us for photon statistics. At this stage, the idea is to obtain the output moments as a function of the input moments. This might seem to be a somewhat daunting task for higher powers of $\hat{n}$, since the full expression for $\hat{n}_o^2$ for example contains 16 terms. However, this amount of algebra is unnecessary: the fact that one input is in the vacuum state simplifies things greatly. The fact is that all normal ordered expressions are trivial to compute. Since the annihilation operator is always on the right, any terms that include the vacuum mode vanish, so that we have

$$\langle : \hat{n}_o^q : \rangle = \alpha^q \langle \hat{n}_i^q \rangle. \tag{6.15}$$

Using this fact in combination with the standard commutation relation $[a, a^\dagger] = 1$ (allowing us to express powers of $\hat{n}$ in terms of normally ordered terms), we can now obtain any moment of $\hat{n}_o$ in terms of the input field.

Although for most purposes we only need to consider photon numbers up to $n = 2$, we will include $n = 3$ in the following expressions for the purpose of evaluating their importance. For any

mode of the field, the following expressions can be obtained from the commutation relation:

$$\begin{aligned} \hat{n} &= :\hat{n}: \\ \hat{n}^2 &= :\hat{n}^2: + :\hat{n}: \\ \hat{n}^3 &= :\hat{n}^3: + 3:\hat{n}^2: + :\hat{n}:. \end{aligned} \tag{6.16}$$

Applying these to the output mode and using Equation 6.15 on the right hand side, we can then write

$$\begin{aligned} \langle \hat{n}_o \rangle &= \alpha \langle : \hat{n}_i : \rangle \\ \langle \hat{n}_o^2 \rangle &= \alpha^2 \langle : \hat{n}_i^2 : \rangle + \alpha \langle : \hat{n}_i : \rangle \\ \langle \hat{n}_o^3 \rangle &= \alpha^3 \langle : \hat{n}_i^3 : \rangle + 3\alpha^2 \langle : \hat{n}_i^2 : \rangle + \alpha \langle : \hat{n}_i : \rangle. \end{aligned} \tag{6.17}$$

Next we have to invert Equations 6.16 so that we can replace the normal ordered terms involving the input mode $\hat{a}_i$. This yields the following expressions:

$$\begin{aligned} \langle \hat{n}_o \rangle &= \alpha \langle \hat{n}_i \rangle \\ \langle \hat{n}_o^2 \rangle &= \alpha^2 \langle \hat{n}_i^2 \rangle + \alpha(1-\alpha) \langle \hat{n}_i \rangle \\ \langle \hat{n}_o^3 \rangle &= \alpha^3 \langle \hat{n}_i^3 \rangle + 3\alpha^2(1-\alpha) \langle \hat{n}_i^2 \rangle + \alpha(1-2\alpha)(1-\alpha) \langle \hat{n}_i \rangle. \end{aligned} \tag{6.18}$$

The next step is to convert these expressions into equivalent ones involving probabilities P_n using Equation 6.13, where the sum over n runs from 0 to 3. The use of this truncated number basis is equivalent to the assumption that the field state has zero amplitude for $n \geq 4$. We adopt the convention of lower case p's for the inputs and upper case P's for the outputs. Explicitly writing out Equation 6.13 for the inputs, we have

$$\begin{aligned} \langle \hat{n}_i \rangle &= p_1 + 2p_2 + 3p_3 \\ \langle \hat{n}_i^2 \rangle &= p_1 + 4p_2 + 9p_3 \\ \langle \hat{n}_i^3 \rangle &= p_1 + 8p_2 + 27p_3. \end{aligned} \tag{6.19}$$

After some algebra, Equations 6.18 then become

$$\begin{aligned} P_1 + 8P_2 + 27P_3 &= \alpha p_1 + 2\alpha p_2 + 3\alpha(2\alpha^2 + 6\alpha + 1)p_3 \\ P_1 + 4P_2 + 9P_3 &= \alpha p_1 + 2\alpha(\alpha+1)p_2 + 3\alpha(2\alpha+1)p_3 \\ P_1 + 2P_2 + 3P_3 &= \alpha(p_1 + 2p_2 + 3p_3). \end{aligned} \tag{6.20}$$

These equations can then be solved for inputs in terms of outputs, or vice versa. Since both can be useful depending on the particular analysis being done, we provide both sets of expressions, beginning with **inputs in terms of outputs:**

$$\begin{aligned} p_1 &= \frac{P_1}{\alpha} - \frac{2P_2(1-\alpha)}{\alpha^2} + \frac{3P_3(\alpha-1)^2}{\alpha^3} \approx \frac{P_1}{\alpha} - \frac{2P_2(1-\alpha)}{\alpha^2} \\ p_2 &= \frac{P_2}{\alpha^2} - \frac{3P_3(1-\alpha)}{\alpha^3} \approx \frac{P_2}{\alpha^2} \\ p_3 &= \frac{P_3}{\alpha^3} \approx 0, \end{aligned} \tag{6.21}$$

and followed by **outputs in terms of inputs:**

$$\begin{aligned} P_1 &= \alpha p_1 + 2\alpha(1-\alpha)p_2 + 3\alpha(1-\alpha)^2 p_3 \approx \alpha p_1 + 2\alpha(1-\alpha)p_2 \\ P_2 &= \alpha^2 p_2 + 3\alpha^2(1-\alpha)p_3 \approx \alpha^2 p_2 \\ P_3 &= \alpha^2 p_3 \approx 0. \end{aligned} \tag{6.22}$$

The approximate expressions on the right are for the case of $P_3 = p_3 = 0$, and would have been the results had we used a basis of $n \leq 2$ from the beginning. The expressions 6.21 are the most important result here, as they give the "upstream" input probabilities in terms of the experimentally accessible output statistics.

6.2.5.4 Correction for known rate of dark counts

When analyzing photodetection statistics it is important to distinguish the behavior of the detector from the properties of the field impinging on it. Since we are interested in evaluating the character of the light emitted from the cavity, corrections need to be made based on known detector properties that affect the data in a measurable way. The two avalanche photodiodes we used had dark count rates of about 160 s^{-1} and 60 s^{-1}, respectively. These are the independently measured rates occurring in the absence of any illumination. The purpose of this section is to outline how we applied corrections to the measured photon statistics due to the contributions of these spurious counts.

Consider the situation depicted in Fig. 6.7, in which we are interested in photoelectric counting statistics at the detectors $D_{A,B}$. For our analysis we will use P's for the total probabilities including dark counts and Q's for corrected probabilities in the absence thereof (equivalently the detector counts arising from the light alone). The notation $P(T)$, $Q(T)$ signifies that the probabilities are for intervals of duration T. The dark count rates at $D_{A,B}$ are the time independent quantities $r_B^{(A,B)}$, yielding single dark count probabilities $b_1^{(A,B)}(T) = r_B^{(A,B)}T$. In the weak field approximation and assuming the dark count rates are also low, singles probabilities can be written as follows:

$$P_1^{A,B}(T) = Q_1^{(A,B)}(T) + b_1^{(A,B)}(T). \tag{6.23}$$

Since the dark counts and the light-related counts are statistically independent, we can write the following simple expression for the probability of registering a coincidence event (one event at each detector):

$$P_c(T) = Q_c(T) + Q_1^{(A)}(T)b_1^{(B)}(T) + Q_1^{(B)}(T)b_1^{(A)}(T) + b_1^{(A)}(T)b_1^{(B)}(T). \tag{6.24}$$

From now on we will drop the dependence on T for compactness. Combining Equations 6.23 and 6.24, we can write the corrected (light-related) coincidence probability Q_c in terms of the experimentally accessible quantities:

$$\begin{aligned} Q_c &= P_c - P_1^{(A)}P_1^{(B)} + \left[P_1^{(A)} - b_1^{(A)}\right]\left[P_1^{(B)} - b_1^{(B)}\right] \\ &= P_c - P_1^{(A)}b_1^{(B)} - P_1^{(B)}b_1^{(A)} + b_1^{(A)}b_1^{(B)}. \end{aligned} \tag{6.25}$$

Equation 6.23 for the singles and 6.25 for the coincidence probabilities were used in our analysis for dark count corrections.

6.2.6 Two-event processes: A model for inferring the two-atom probability

One of the main ways of characterizing the quality of a single-photon source is by measuring the suppression of higher photon numbers. For an ideal source and ideal detectors, one would never register more than one photoelectric event per trial. In a real experimental setting, however, there are always sources of background counts. This background is typically composed of detector dark counts and events from scattered light, and the rate of these counts is easy to measure. Background counts and legitimately detected single photons combine to make coincidence events. However, knowing the probabilities of each of these statistically independent processes allows us to predict the probability of these background-related coincdiences.

In our experiment, we observed a rate of coincidences that exceeded even this prediction. This is illustrated in Fig. 6.9 which compares the data to the predicted suppression factor $R_{BP}(t)$ in the hypothetical case that coincidences only arise from background counts. The predicted trace has a pronounced peak around 240 ns, and decays from there to be $R_B(\delta t) = 52.5$ at the end of the Ω_3 window. The maximum occurs near the peak of the average single-photon pulse (see Fig. 6.2(a)), and the purity of the single-photon data begins to degrade as more and more background counts are allowed to accumulate. Clearly if our photon pulse were shorter, the peak would reach a higher value since fewer background counts (and hence fewer coincidences) would occur during the pulse. Additionally, the rate at which $R_{PB}(t)$ decays increases with background count rate.

What follows is a discussion of the discrepancy between the two traces in Fig. 6.9, and the analysis we performed to explain it. We investigated several optical processes that might yield more

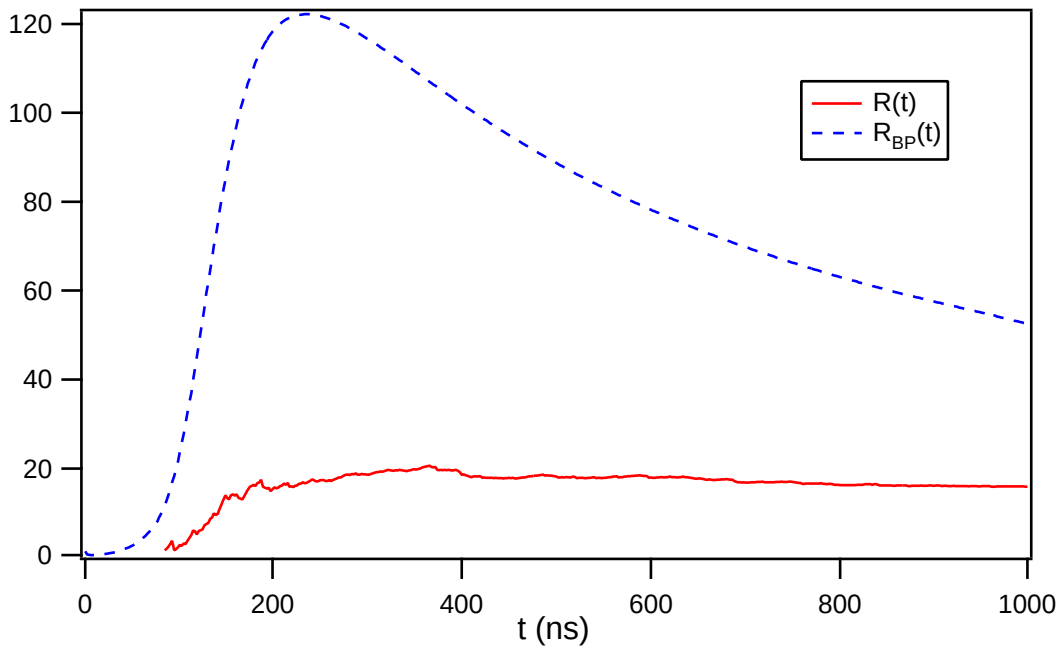

Figure 6.9: Plotted are the data $R(t)$ quantifying the suppression of two-photon events relative to a weak coherent state, and the theoretical prediction $R_{BP}(t)$ based on the known rate of background counts in our experiment. The experimental trace $R(t)$ is the same as the one plotted in Fig. 6.2(c). See text for a discussion of the discrepancy between these curves.

than one photon per trial, including the atom's recycling by stray light from the Ω_4 beam or by diverse off-resonant excitation mechanisms, including from the FORT itself. We conclude that none of these are responsible for the observed disparity between R and R_B. Instead, as demonstrated by Fig. 6.4, the excess coincidences likely arise from infrequent events in which two atoms are trapped within the cavity, each atom contributing one photon during the detection window. This section describes the model we used for the theoretical curve in Fig. 6.4, which tries to predict the time dependence of the photon statistics of our cavity output during single-photon generation. The model is based on the hypothesis that we sometimes load two atoms into the cavity.

The basic approach taken for this calculation is to use experimental data for the two-photon probability at early trapping times to estimate the initial two-atom probability. From there, we predict the time evolution of the two-atom fraction and compute the resulting photon statistics vs. trapping time, and finally compare it to the full data set, as in Fig. 6.4.

6.2.6.1 Photon statistics vs. atom number

The first step then is to develop a model for how two atoms in the cavity impact the photon statistics in our experiment. We begin by considering the one-atom and two-atom cases separately, and later consider a statistical mixture of these. In this model we make two major assumptions:

first that two atoms act independently inside the cavity (both with respect to the trap decay and photon generation). Second, we assume that there are at most two atoms in the cavity and neglect three-or-more-photon events.

The starting point is the model for what happens inside the cavity (or equivalently at the output of an ideal, single-sided cavity with our finesse) for one atom and two atoms. Let the probability of one atom to generate one photon be denoted ϕ_G. We'll use lower case p's for statistics "inside the cavity" and upper case P's for photodetection statistics after our losses (overall efficiency $\alpha \approx 2.4\%$, see Table 6.1). We will also consider the quantities corrected for dark counts, indicated by the tilde: $\tilde{P}_{1,2}$. For **one atom**, we have

$$p_1^I = \phi_G \tag{6.26}$$

$$p_2^I = 0 \tag{6.27}$$

$$P_1^I = \alpha\phi_G + P_B \tag{6.28}$$

$$P_2^I = P_B P_1^I = P_B(\alpha P_G + P_B), \tag{6.29}$$

where P_B is the total background count rate (both detectors). The derivations of these are trivial: inside the cavity one photon is generated with likelihood ϕ_G, and we never make two photons. At the detectors, we have attenuated single photons, background singles, coincidences from one signal and one background click, and pairs of background clicks. For **two atoms**, we have

$$p_1^{II} = 2\phi_G(1-\phi_G) \tag{6.30}$$

$$p_2^{II} = \phi_G^2 \tag{6.31}$$

$$P_1^{II} = \alpha(p_1^{II} + 2p_2^{II}(1-\alpha)) + P_B = 2\alpha\phi_G(1-\alpha\phi_G) + P_B \tag{6.32}$$

$$P_2^{II} = \alpha^2\phi_G^2 + P_B P_1^{II} + P_B^2 = \alpha^2\phi_G^2 + 2\alpha\phi_G P_B(1-\alpha\phi_G) + P_B^2. \tag{6.33}$$

These derivations are slightly more nontrivial, as they include the formalism for propagating photon statistics across losses (Section 6.8), and a simple use of the binomial distribution. Equation 6.30 is based on the fact that there are two ways of getting one photon: atom 1 succeeds and atom 2 fails, and vice versa. Equation 6.31 is trivial. The next two also use the equations of Section 6.8. We've incorporated background contributions in Equations 6.32 and 6.33 in the same way as we did in Equations 6.28 and 6.29.

6.2.6.2 Statistical mixture of atom numbers

The next step is to write down the average statistics when we have a data set which is a mix of one-atom and two-atom data. The way our statistics are compiled is that (to a good approximation)

there is always at least one atom. We'll therefore parameterize the fraction of the data with two atoms as η_{II}, with the one-atom fraction then $\eta_I = (1 - \eta_{II})$. These fractions are percentages of the single-photon-generation (SPG) *attempts*, and will lead to the one- and two-atom "populations" that we're interested in (and for which we know how to model the time dependence). Let's denote the total number of SPG attempts in the data set N_A, the number of single detection events N_1, and define $N_2 \equiv 2N_c$ where N_c is the number of coincidence events. Our overall measured statistics should then be given by

$$N_1 = \eta_I N_A P_1^I + \eta_{II} N_A P_1^{II} \tag{6.34}$$

$$N_2 = \eta_I N_A P_2^I + \eta_{II} N_A P_2^{II}. \tag{6.35}$$

Note that these formulas hold for any "part" of the data set, if it were divided by time. Resulting photodetection probabilities $P_{1,2}^e$ can then be written (see Equations 6.32 and 6.33)

$$P_1^e = \eta_I P_1^I + \eta_{II} P_1^{II} = (1 - \eta_{II})\alpha\phi_G + 2\eta_{II}\alpha\phi_G(1 - \alpha\phi_G) + P_B \tag{6.36}$$

$$P_2^e = \eta_I P_2^I + \eta_{II} P_2^{II} = (1 - \eta_{II})\alpha\phi_G P_B + \eta_{II}\alpha\phi_G(\alpha\phi_G + 2P_B(1 - \alpha\phi_G)) + P_B^2. \tag{6.37}$$

Similarly, in the absence of dark counts, we have

$$\tilde{P}_1 = \eta_I\alpha\phi_G + 2\eta_{II}\alpha\phi_G(1 - \alpha\phi_G) + P_S \tag{6.38}$$

$$\tilde{P}_2 = \eta_I\alpha\phi_G P_S + \eta_{II}\alpha\phi_G(\alpha\phi_G + 2P_S(1 - \alpha\phi_G)) + P_S^2 \ .$$

Here $P_S = P_B - P_D$ is the probability of a background event other than from detector dark counts in the detection window $[t_0^j, t_0^j + \delta t]$ (i.e., scattered light). From the measured photoelectric counting statistics, the known probability $P_S = 4.9 \times 10^{-5}$, and the overall efficiency α, we can solve this pair of equations for the two unknowns ϕ_G and η_{II}. Actually the product $\alpha\phi_G$ always appears together in these equations, so that it can be considered one of the independent variables. This means that η_{II} is determined directly from measured statistics, and is independent of α. ϕ_G on the other hand is inversely proportional to α, given fixed detection statistics.

For the first bin of Fig. 6.4 (with the values $\tilde{P}_1 = 0.0285, \tilde{P}_2 = 2.68 \times 10^{-5}$ derived from P_1, P_2 by correcting for dark counts), we find $\alpha\phi_G = 0.0276$ and $\eta_{II} = 0.033$.

6.2.6.3 Photon statistics vs. time

The full curve in Fig. 6.4 is obtained by employing these values for $\alpha\phi_G$ and η_{II} as initial conditions to deduce the time dependence of the photon statistics over the duration of the trapping interval. The time dependence of η_I, η_{II} is modelled by simple rate equations with initial conditions

$(\eta_I^0, \eta_{II}^0) = (0.967, 0.033)$. We also use the experimentally determined decay rate $\Gamma_1 = 1/0.14$ s, and the assumption $\Gamma_2 = 2\Gamma_1$.

More explicitly, we have the following relationships:

$$\eta_I = \frac{p_I}{p_I + p_{II}} \tag{6.39}$$

$$\eta_{II} = \frac{p_{II}}{p_I + p_{II}}, \tag{6.40}$$

where $p_{I,II}$ are the overall one- and two-atom fractions, whereas the η's just quantify one vs. two without allowing for zero. The population dynamics are driven by the following birth-death equations:

$$\begin{aligned} \dot{p}_0 &= \Gamma_1 p_I \\ \dot{p}_I &= -\Gamma_1 p_I + 2\Gamma_1 p_{II} \\ \dot{p}_{II} &= -2\Gamma_1 p_{II} \ , \end{aligned} \tag{6.41}$$

where the zero-atom fraction $p_0 \equiv 1 - p_I - p_{II}$. In order to proceed, we need to know the loading efficiency (which includes both one- and two-atom events). This can be extracted from the data, which gives a loading rate of 9.2%. Using this number along with the inferred initial value of η_{II}, we can trivially solve for $p_{I,II}$ at $t = 0$. The Equations 6.41 are then solved using these initial values, and the results are displayed in Fig. 6.10. This figure also includes resulting predictions for the photon statistics (corrected for dark counts).

We now turn to some discussion of the qualitative characteristics of Figs. 6.10 (a-d). In panel (a), we can clearly see that the two-atom decay rate is twice that of the one-atom rate Γ_1, as expected from this independent, single-exponential decay model. Panel (b) plotting the singles probability vs. trapping time shows a slightly higher production rate of single photons at early times than at late times. This can be explained by the higher fraction of two-atom data at early trapping times, combined with the fact that sometimes two photons produced in the cavity lead to only one photoelectric event at the detectors. Fig. 6.10(c) shows the drastic reduction of coincidence probability late in the trapping interval when the two-atom probability is reduced relative to that of one atom. This clearly shows the near-ideal nature of our single-photon source if the two-atom contribution is no longer a factor. We also note that panel (d) contains the same plot of R_0 as Fig. 6.4, but here plotted on a linear scale and out to much longer trapping times. The asymptotic value of $R_0 \approx 294$ quantifies how much the residual scattered light contaminates the single-photon source (when the two-atom probability is greatly suppressed).

In order to compare the theoretical curve in Fig. 6.10 to the data, the lifetime Γ_1 must be determined. The approach we took was to look at the distribution of trapping event durations in

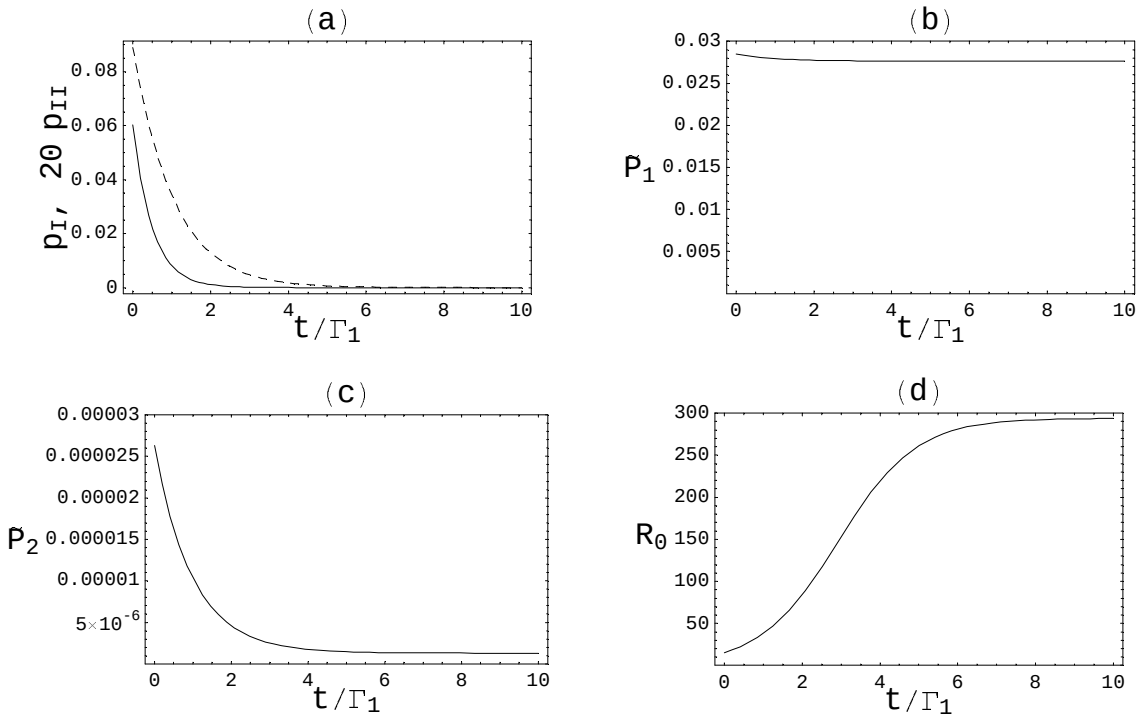

Figure 6.10: Results of the simple model described in the text to predict the time evolution of two-atom and two-photon probabilities. The quantities $\tilde{P}_1$, $\tilde{P}_2$ and R_0 related to photoelectric statistics are all corrected for dark count contributions. Panel (a) contains the one- and two-atom populations $p_{I,II}$, where the dashed trace is p_I and the solid trace is $20p_{II}$. Panel (b), (c) and (d) display the quantities $\tilde{P}_1$, $\tilde{P}_2$ and R_0, respectively. The scaling of the time axes is with respect to the single atom trap decay rate Γ_1. These results correspond to the same data set as was used for Fig. 6.4.

the data and perform an exponential fit. As it turns out, the trap decay behavior does not seem to be exponential, so it is important to explore the deviations from this. Clearly this is a major limitation of our simple model and will have to be taken into account in future any attempt to obtain better quantitative agreement with the data.

Figure 6.11 illustrates an attempt to better understand and quantify the decay dynamics. The data traces are all histograms of the number of single-photon attempts in each time bin. Our data analysis program automatically truncates each record of photoelectric events when it determines that the atom has left the trap (see Section 6.2.3). Although we could have plotted the number of photons detected vs. trapping time, this would have included possible fluctuations in the rate of photon production. In any case, plotting attempts vs. trapping time t_T seemed to be the most direct way to access the distribution of event durations.

Panel (a) of Fig. 6.11 illustrates a truncation procedure we used to eliminate the earliest times after trap loading for the purposes of obtaining the lifetime. Only the indicated truncated section of the trace was used for the fits. The reason for this is that at early times t_T, there are many events where only one photon is detected in the first ≈ 5 ms (500 attempts). Since this is well below

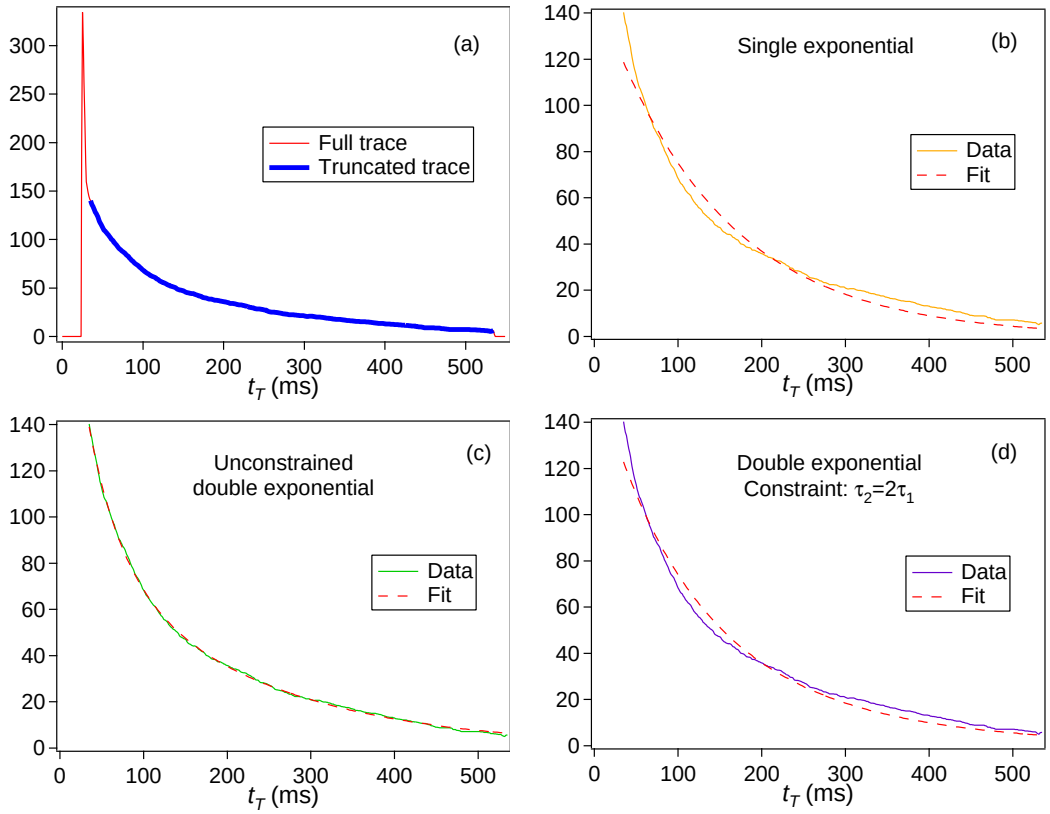

Figure 6.11: Various fitting attempts to determine the trap lifetime in our single-photon generation experiment. The vertical axis of all panels (arbitrary units) is proportional to the number of photon generation attempts per time bin (see text for further explanation). The asymptotes in all fits were forced to be zero (no vertical offsets allowed). In panel (b), the fit yields a lifetime $\tau = 140 \pm 28$ ms. This was the lifetime used for the analysis leading to Fig. 6.4. Panel (c) gave lifetimes $(\tau_1, \tau_2) = (200 \pm 5, 39.4 \pm 0.5)$ ms and weights $(A_1, A_2) \approx (94, 146)$ (arb. units). Panel (d) gives $\tau_1 = (95 \pm 18)$ ms, $\tau_2 = 2\tau_1$ and $(A_1, A_2) \approx (70, 90)$ (arb. untis).

the overall average of one detected photon every ≈ 36 attempts, this leads to an excess of recorded generation attempts before the determination is made that the atom is gone. This is an indication that our "triggering" algorithm outlined in Section 6.2.3 could be improved, since many of these short events are probably failed loading attempts ($N = 0$), with the recorded photoelectric events arising from background processes.

Turning next to the fitting attempts, it is clear that the single exponential fit in panel (b) is not in very good agreement, so we tried to consider slightly more complicated decay behavior. One idea was that since the two-atom population supposedly decays twice as fast, this additional timescale $\Gamma_2 = 2\Gamma_1$ should be incorporated into the decay model. This led to the fit attempt in panel (d), where the fitting equation was a sum of two exponentials with arbitrary weights, but whose time constants were constrained as indicated. This fit was not very successful either, and on further consideration, the small ($\eta_{II} \approx 3\%$) two-atom contribution is so small that the impact on such a

decay curve should not be appreciable anyway. With this consideration in mind, it is somewhat puzzling that the double exponential fit in panel (c) is in such close agreement with the data. The two resulting timescales ($\approx$ 200 ms and $\approx$ 40 ms) are widely separated, and the weights of the two exponentials are similar.

Our hypothesis is that there is most likely an inhomogeneity from event to event in the trap decay rates, for any of several possible reasons. There could be a distribution of event durations from a spread in initial atomic temperatures right after trap loading. Another possibility is that there could be a dependence of the lifetime on which well of the standing-wave FORT the atom is trapped in, since the coupling strength g at the center of various wells is different. It will be interesting to see if future attempts to do reliable three-dimensional cooling and well-selective trap loading will eliminate this possible inhomogeneity in lifetimes.

In any case, since we only sought qualitative agreement for the purpose of Fig. 6.4, and since it would have been difficult to incorporate more complex decay dynamics than Equations 6.41, we decided to simply use the single exponential result shown in Fig. 6.11(b).

6.3 Additional experimental data

6.3.1 Dependence of pulse shape on pumping and recycling powers

One area that was not systematically explored much in the work leading to Ref. [36] was the dependence of the pulse shape $n(t)$ (Fig. 6.2(a)) on the pump powers $\Omega_{3,4}$. We did do one cursory investigation of this question, yielding somewhat interesting results, shown in Fig. 6.12. The two changes made from the usual power settings were to lower the power of each of the $\Omega_{3,4}$ beams separately by a factor of 5. The major observation of note is that the weakened Ω_3 field (Fig. 6.12 (b)) has a drastic impact on the pulse shape.

As discussed above in Section 6.1 [36], we hypothesize that the shape of these curves is actually inhomogeneously broadened in the following sense. The actual effective Rabi frequency Ω_3 for a given attempt to generate a photon depends on more than the beam intensity at the atom's position. Ω_3 also depends on the local polarization and the atom's magnetic sublevel (dictated by the relevant Clebsch-Gordan coefficients). In fact, if the atom happens to be in the state $(F = 3, m_F = 0)$ in a basis defined by the local Ω_3 polarization, the Rabi frequency vanishes. This type of dark state occurs generally for for transitions $F \rightarrow F'$, including $4 \rightarrow 4'$, used in our experiments for recycling.

In our experiment, the $\Omega_{3,4}$ beams formed a polarization gradient, meaning that with atomic motion in the transverse direction possibly extending over many μm, the atom "saw" different polarizations from shot to shot. In addition, stray magnetic fields and effective Zeeman shifts from residual ellipticity of the FORT (see chapter 7) presumably caused Larmor precession on fast timescales. This means that the sublevel could not be expected to remain constant from trial to

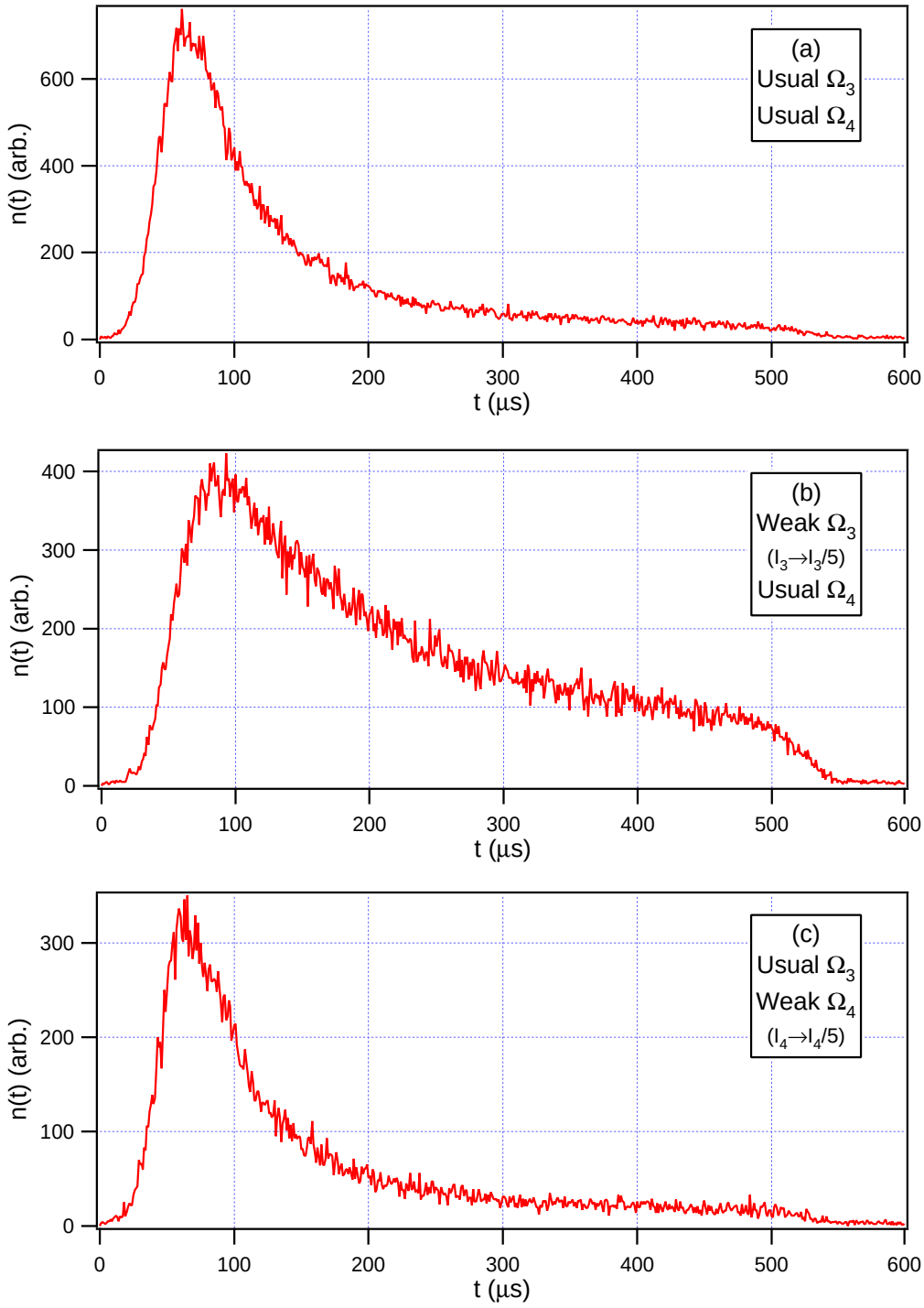

Figure 6.12: Single-photon pulse shape as characterized by time-resolved histograms $n(t)$ of photoelectric events. Three traces are shown, each for a different setting of the pumping/recycling powers $\Omega_{3,4}$. The arbitrary units on the vertical axes are *not* the same in the different panels, since the number of counts per time bin depends on the total amount of data taken (number of trials).

trial. The upshot of all this is that the randomness of these variables (polarization and m_F) led to large shot-to-shot fluctuations in the effective coupling Ω_3, which is largely responsible for how fast (or slowly) the photon is produced. Weakly coupled atoms presumably produced a broader pulse shape, and a delayed peak.

Returning now to Fig. 6.12, we see that the data support this theory somewhat. The lower Ω_3 setting (panel (b)) produced a significantly broadened and delayed pulse with respect to the pulse obtained at the usual settings (panel (a)). Lowering the overall power should have the same effect on the dynamics as a change in the Clebsch-Gordan coefficient due to the Zeeman substructure. In panel (c), we see that the pulse shape is not significantly modified by a change in the Ω_4 power. This makes sense since Ω_4 is gated off during the actual Ω_3 photon production window. Incidentally, one effect not illustrated by these plots was a reduction in the photon production efficiency P_1 of about 40% for the weak Ω_4 case. This is not surprising since a weaker Ω_4 reduces the likelihood of recycling the atom back to $F = 3$, where it must be for photon production to succeed. It should be noted that the efficiency was not significantly affected by the weakened Ω_3 setting (cases (a) vs. (b) in Fig. 6.12).

6.3.2 Correlation function from experiment without filter cell

As discussed in Section 6.2.1, the use of the Cs filter cell led to a relatively high rate of background counts in between trials Ω_3 (scattered light from the pump beam). As a result of this, for the purpose of computing $C(\tau)$ (Fig. 6.3) we removed counts from the data set that did not lie in a 'production window' when Ω_3 was on (see Section 6.2.4). Earlier experiments, including those leading to Fig. 6.12, were performed without the filter cell in place. Although without the cell there was a higher background rate during the Ω_3 trials, the data looks qualitatively similar, and it is instructive to examine it here.

Fig. 6.13 displays such a correlation function, taken from the data set that produced Fig. 6.12(a). In Fig. 6.13(a), plotted out to ± 200 μs (± 20 trials) we observe no visible decay in the peak heights, meaning that it is just as likely to observe a coincidence separated by 20 trials as if they were separated by only one. This results from the fact that the ± 200 μs displayed here is much less than the mean storage time of the atoms in the presence of the pumping and recycling fields, $\tau_{trap} \approx 140$ ms. This emphasizes the strong qualitative difference between our work documented in Ref. [36] and that of Ref. [66], where the peak heights in their equivalent function decayed at a rate given by the transit time of a freely falling atom (about 17.5 μs).

We turn now to a comparison between Figs. 6.3 and 6.13. As can be seen in Figs. 6.13(a, b), the regions between the peaks have a background level of coincidence counts which is absent in Fig. 6.3 (for which the counts in between trials have been removed). With those counts removed it is trivial to show that it is impossible to register a coincidence event for which the separation is $\Delta t/2 = 5$ μs

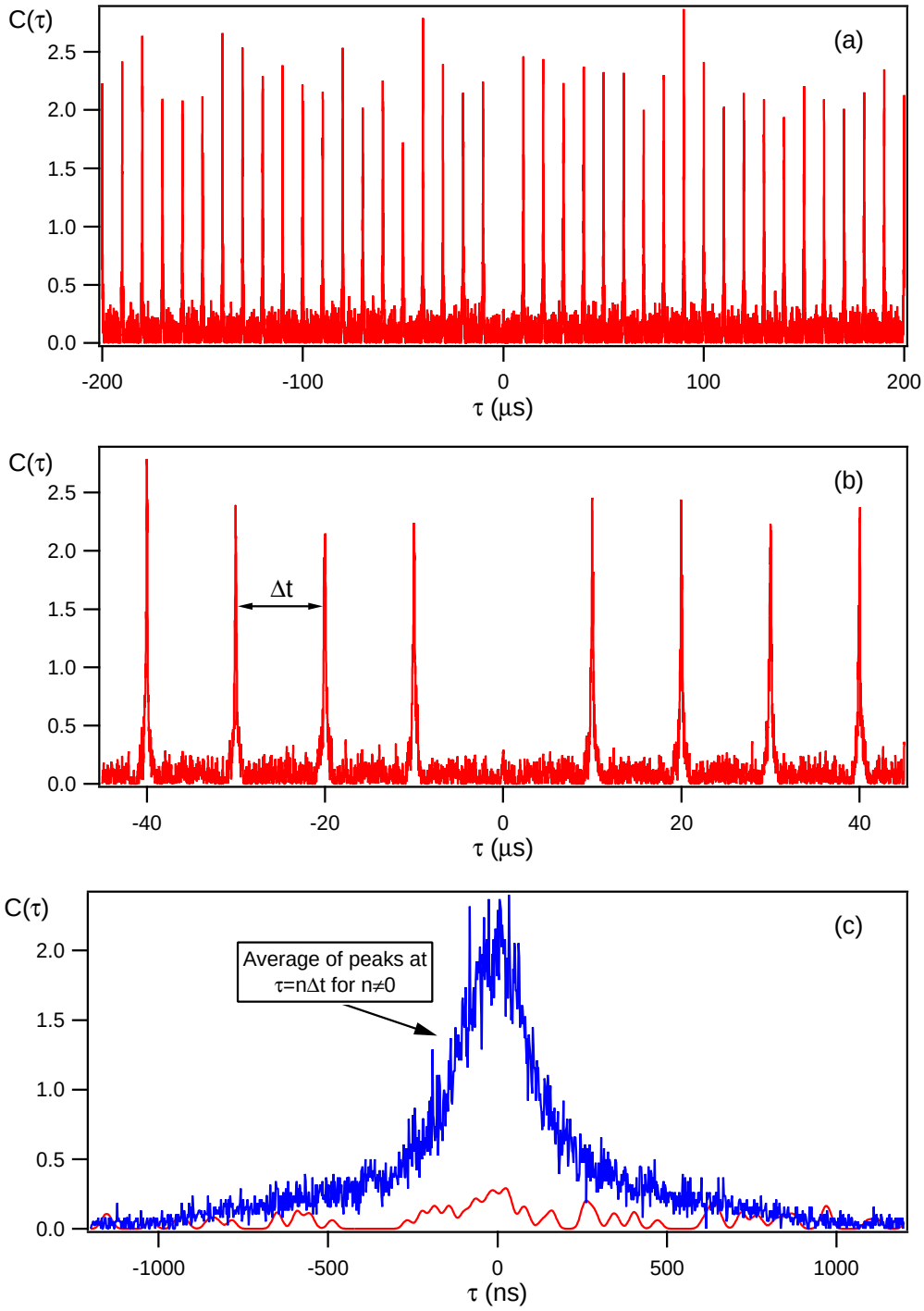

Figure 6.13: Correlation function $C(\tau)$ (histogram of time-resolved coincidence events) computed from the same data set used for Fig. 6.12(a), and plotted at three levels of detail (ranges of the τ axis). All traces $C(\tau)$ have been smoothed as described in Section 6.2.4. $\Delta t = 10$ μs is the time separation between trials.

(for example). More precisely, $C(\tau)$ vanishes for τ outside the regions defined by $|\tau - n\Delta t| \leq 2\delta t$ (n is an arbitrary integer). In Fig. 6.13 on the other hand, coincidences occur at all delay times. It is obvious that when all counts from the record are included, background events such as dark counts give rise to coincidences with arbitrary time separations. Scattered Ω_4 light contributes significantly to $C(\tau)$ between peaks (these counts are removed in the processing for Fig. 6.3 since they occur simultaneously with the cell pumping stage, in between trials). In spite of this background related noise level in $C(\tau)$, Fig. 6.13 is shown here partly to indicate that the data in Fig. 6.3 is not qualitatively altered by this processing step, and the sought-after features of $C(\tau)$ are still present without it.

Fig. 6.13(c) is zoomed in on the central region around $\tau = 0$. We also display the average of the non-central peaks ($n \neq 0$) on the same plot. Specifically, this curve is the average of $C(\tau - n\Delta t)$ over n, excluding $n = 0$ and going out to $n = \pm 19$. This emphasizes the suppression of likelihood to register two events (a coincidence) in the same trial, compared to registering them in separate trials. It can be shown that the ratio of areas of the two traces shown here corresponds approximately to the quantity R, and this has been verified for these data.

Chapter 7

Calculation of AC Stark Shifts

Motivated by our desire to implement a state-insensitive dipole trap for atomic cesium in the setting of cavity quantum electrodynamics [27], we have developed a unified, consistent formalism for computing the ac Stark shifts that includes the shifts of the excited states. Although there already exists a great deal of literature on this subject, many authors restrict their attention to the ground-state shifts, which determine the depths of dipole traps. The shifts of the excited states are important for any spectroscopic application since they alter transition frequencies. They also impact motional heating which arises from force fluctuations on driven atoms in dipole traps.

The structure of the chapter is as follows. Section 7.1 presents the basic formalism and equations necessary for computing the Stark shifts. Section 7.2 presents the application of the formalism to the special case of the alkali atom ground states. Section 7.3 gives the relevant expressions for obtaining absolute Stark shifts in real units, based on experimentally accessible quantities. Section 7.4 then presents results of the calculations for the excited states of Cs, with particular emphasis on state-insensitive trapping [27]. A quantitative evaluation is included of the contributions to the shifts of higher-lying excited states and the counter-rotating terms.

7.1 Basic formalism and dipole matrix elements

The expressions provided herein are most relevant to the case of far-off-resonance traps (FORTs), in which the field drives the atom well below saturation due to very large detunings. The detunings also far exceed all hyperfine splittings, which also somewhat simplifies the formalism.

We consider a multilevel atom with several levels labelled by their total electronic angular momentum J and energies $E_{\gamma J}$, where γ is a shorthand index for all other quantum numbers (e.g., radial, electron orbital angular momentum). Each of these levels has hyperfine structure due to the nuclear spin I, so that each state within the J-manifold also has total angular momentum F and magnetic quantum number m (we neglect the hyperfine splittings). The specific example of cesium is depicted in Fig. 7.1.

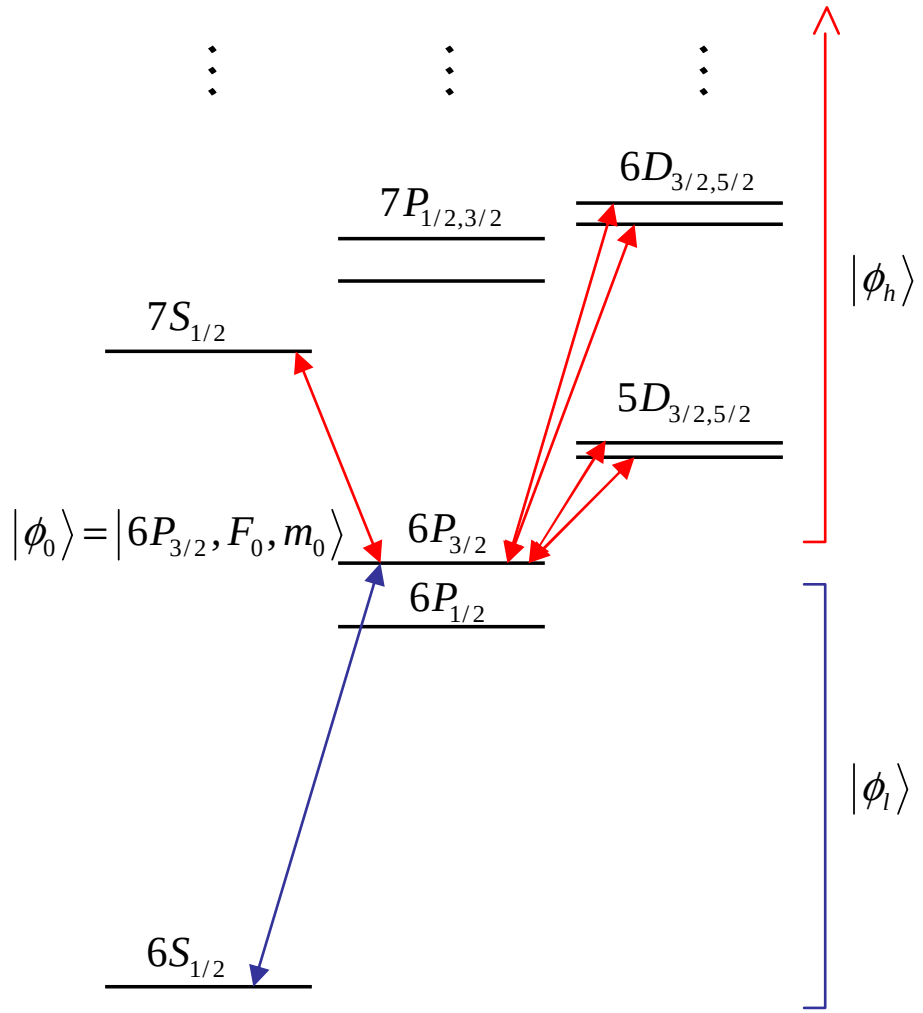

Figure 7.1: A partial schematic level structure of cesium. Allowed dipole transitions from states in the $6P_{3/2}$ manifold are indicated with arrows. The ac Stark shift to a state $|\phi_0\rangle$ in this manifold will contain contributions $U_0^{(L)}$ from the ground state $6S_{1/2}$ as well as $-U_0^{(H)}$ from the higher-lying S and D states.

The perturbation to be considered is the dipole interaction with a laser field of frequency ω_L,

$$\mathbf{E}(\mathbf{r},t) = E(\mathbf{r})\vec{\varepsilon}(\mathbf{r})\cos\left(\omega_L t + \Phi(\mathbf{r})\right), \tag{7.1}$$

where throughout this chapter we will only study the case of spatially varying amplitude and constant polarization: $\vec{\varepsilon}(\mathbf{r}) = \vec{\varepsilon}$, where $|\vec{\varepsilon}| = 1$ for all $\mathbf{r}$.

In the presence of $\mathbf{E}$, the state $|\phi_0\rangle = |\gamma_0 J_0 F_0 m_0\rangle$ with unperturbed energy $\mathcal{E}_0$ will experience the following ac Stark shift, due to the interaction of the field with the induced atomic dipole moment:

$$U_0(\mathbf{r}) = U_0^{(H)}(\mathbf{r}) - U_0^{(L)}(\mathbf{r}) \ , \tag{7.2}$$

where $U_0^{(H)}$ ($U_0^{(L)}$) is the shift to due to atomic levels with energies $\mathcal{E}_h > \mathcal{E}_0$ ($\mathcal{E}_l < \mathcal{E}_0$). In the large detuning limit where no transition is near saturation, these terms are given by [68]

$$\begin{aligned} U_0^{(H)}(\mathbf{r}) &= \sum_h \frac{|\langle\phi_0|\hat{\mathbf{d}}\cdot\mathbf{E}(\mathbf{r})|\phi_h\rangle|^2}{4\hbar\Delta_h} \\ U_0^{(L)}(\mathbf{r}) &= \sum_l \frac{|\langle\phi_0|\hat{\mathbf{d}}\cdot\mathbf{E}(\mathbf{r})|\phi_l\rangle|^2}{4\hbar\Delta_l}\ , \end{aligned} \tag{7.3}$$

where $\Delta_{h,l} = \omega_L - |\mathcal{E}_{h,l} - \mathcal{E}_0|/\hbar$.

We will now restrict our calculation to fields with pure polarization q in the spherical basis, $\mathbf{E}(\mathbf{r}) = E(\mathbf{r})\vec{\varepsilon}_q$. However, this treatment can be extended to more general polarization states by taking linear superpositions of these.

From this point on, we adopt a convention for the ordering of the dipole matrix elements: we will always write the state with higher energy to the left of the dipole operator. The reason for this is that the process of reduction of the matrix elements via the Wigner-Eckart theorem is inherently asymmetric. The contributions $U^{(H,L)}$ to the Stark shift must then be written

$$\begin{aligned} U_0^{(H)}(\mathbf{r}) &= |E(\mathbf{r})|^2 \sum_h \frac{|\langle J_h F_h m_h|\hat{d}_q|J_0 F_0 m_0\rangle|^2}{4\hbar\Delta_h} \\ U_0^{(L)}(\mathbf{r}) &= |E(\mathbf{r})|^2 \sum_l \frac{|\langle J_0 F_0 m_0|\hat{d}_q|J_l F_l m_l\rangle|^2}{4\hbar\Delta_l}\ , \end{aligned} \tag{7.4}$$

where the γ indices have been omitted in the interest of compactness.

The next task is the reduction of the dipole matrix elements. For this we will use primed quantum numbers for higher-lying states.

$$|\langle J'F'm'|\hat{d}_q|JFm\rangle|^2 = (2F+1)|(J'\|\mathbf{d}\|J)|^2 \times \left|\left\{\begin{array}{ccc} F' & I & J' \\ J & 1 & F \end{array}\right\}\right|^2 |c_{F,m}^{F',m'}|^2, \tag{7.5}$$

where the quantity in curly brackets is the Wigner 6-j symbol[1], the shorthand notation $c_{F,m}^{F',m'}$ for the Clebsch-Gordan coefficients is explicitly given as follows[2]:

$$c_{F,m}^{F',m'} = \langle Fm1q|F'm'\rangle \tag{7.6}$$

$$= (-1)^{m+F-1}\sqrt{2F'+1}\begin{pmatrix} F & 1 & F' \\ m & q & -m' \end{pmatrix}, \tag{7.7}$$

and the selection rule is $m' = m + q$. We choose the following normalization for the reduced matrix

[1] The Wigner 6-j symbols are computed using the Mathematica function "SixJSymbol"

[2] These conventions are consisent with the Mathematica functions "ClebschGordan" (Equation 7.6, RHS) and "ThreeJSymbol" (Equation 7.7, RHS)

element, expressed in terms of the lifetime $\tau_{J'\to J}$ of state J' in the case of one decay channel $J' \to J$:

$$|(J'\|\mathbf{d}\|J)|^2 = (2J'+1)\frac{3\pi\epsilon_0\hbar c^3}{\omega_{JJ'}^3\tau_{J'\to J}} \ , \tag{7.8}$$

where $\omega_{JJ'}$ is the resonant frequency of the transition, and we have used MKS units. It is important to point out that there are several conventions for this normalization. Here I have used notation from the notes of Steck [43], since the treatment here corresponds to the alternative normalization he describes on p. 7 (*not* his main choice of normalization). In her thesis, Christina Hood [40] relies on the formalism of Deutsch and Jessen [121], which seems to require a third, different normalization convention. In addition, it seems that the reduced matrix elements in Table 6.2 of her thesis are not normalized properly for this formalism. Armed with Equation 7.8 and the others in this section, however, it is possible to calculate unambiguously the matrix elements (and hence the Stark shifts).

At this point, given the partial lifetimes for all relevant transitions and their resonant frequencies, as well as the FORT intensity, these equations are sufficient for calculating Stark shifts of any state (ground or excited).

7.2 Special case: the ground states

Perhaps the most commonly required formula for alkali atom FORTs is the expression for the ground-state shifts $U_{F,m,q}^{(G)}(\mathbf{r})$, considering only the lowest lying $P_{1/2}$ and $P_{3/2}$ excited states (i.e., the $D1$ and $D2$ lines). In our approximation of large detuning and weak excitation, there is negligible excited state population, so that the ground-state shift is effectively the FORT depth.

Without going through the required angular momentum algebra, we simply state here the formula for these shifts in several forms. The first is in terms of the reduced matrix elements $(J'\|\mathbf{d}\|J)$, which in the formalism of this chapter is given by

$$U_{F,m,q}^{(G)}(\mathbf{r}) = \frac{1}{24}|E(\mathbf{r})|^2\left(\frac{|(6P_{3/2}\|\mathbf{d}\|6S_{1/2})|^2(2+qg_Fm)}{2\hbar\Delta_{D2}} + \frac{|(6P_{1/2}\|\mathbf{d}\|6S_{1/2})|^2(1-qg_Fm)}{\hbar\Delta_{D1}}\right) \ . \tag{7.9}$$

Here, g_F are the g-factors for the hyperfine ground states of Cs ($g_3 = -1/4$ and $g_4 = 1/4$). The detunings are with respect to the $D1$ and $D2$ resonance frequencies, e.g. $\Delta_{D1} = \omega_L - \omega_{D1}$.

Using the following approximate identity from further reduction of the matrix elements (which seems to differ from experimental values by about 1%) [43]

$$d_{D2}^2 \equiv |(6P_{3/2}\|\mathbf{d}\|6S_{1/2})|^2 \approx 2|(6P_{1/2}\|\mathbf{d}\|6S_{1/2})|^2 \ , \tag{7.10}$$

we can simplify Equation 7.9 somewhat:

$$U^{(G)}_{F,m,q}(\mathbf{r}) = \frac{|d_{D2}E(\mathbf{r})|^2}{48}\left(\frac{2+qg_Fm}{\hbar\Delta_{D2}} + \frac{1-qg_Fm}{\hbar\Delta_{D1}}\right). \tag{7.11}$$

This agrees with the following equation, which also appears as Equation 19 in Ref. [68] and as Equation 7.16 in Ref. [25]:

$$U^{(G)}_{F,m,q}(\mathbf{r}) = \frac{\pi c^2\Gamma_{D2}}{2\omega^3_{D2}}\left(\frac{2+qg_Fm}{\Delta_{D2}} + \frac{1-qg_Fm}{\Delta_{D1}}\right) I(\mathbf{r}) \ , \tag{7.12}$$

where $I(\mathbf{r}) = \frac{1}{2}c\epsilon_0|E(\mathbf{r})|^2$. Please note that in Ref. [68], the undefined quantities Γ and ω_0 are for the $D2$ line ($\Gamma = \Gamma_{D2}$ and $\omega_0 = \omega_{D2}$).

Writing this expression yet another way, we can gain some insight into the qualitative characteristics of the shifts:

$$U^{(G)}_{F,m,q}(\mathbf{r}) = \frac{\pi c^2\Gamma_{D2}}{2\omega^3_{D2}}\left[\left(\frac{2}{\Delta_{D2}} + \frac{1}{\Delta_{D1}}\right) + \left(\frac{1}{\Delta_{D2}} - \frac{1}{\Delta_{D1}}\right) qg_Fm\right] I(\mathbf{r}) \ , \tag{7.13}$$

The m-dependent part of this shift is directly proportional to g_Fm, just like a Zeeman shift in a static magnetic field. For this reason, this contribution is often referred to as an "effective magnetic field" term. In addition, this m-dependent component does not occur for linear polarization $q = 0$. If one goes through the algebra for a general (elliptical) state of FORT polarization, it is not difficult to obtain the following formula [64]:

$$U^{(G)}_{F,m,\epsilon}(\mathbf{r}) = \frac{\pi c^2\Gamma_{D2}}{2\omega^3_{D2}}\left[\left(\frac{2}{\Delta_{D2}} + \frac{1}{\Delta_{D1}}\right) + \left(\frac{1}{\Delta_{D2}} - \frac{1}{\Delta_{D1}}\right)\sqrt{1-\epsilon^2}g_Fm\right] I(\mathbf{r}) \ , \tag{7.14}$$

where ϵ is the ellipticity of the field, as defined in Ref. [64] by the following normalized polarization vector:

$$\begin{aligned}\vec{\varepsilon}_L &= \frac{1}{\sqrt{2}}(\vec{\varepsilon}_x\sqrt{1+\epsilon} + i\vec{\varepsilon}_y\sqrt{1-\epsilon}) \\ &= \frac{1}{2}((\sqrt{1+\epsilon}+\sqrt{1-\epsilon})\vec{\varepsilon}_1 + (\sqrt{1+\epsilon}-\sqrt{1-\epsilon})\vec{\varepsilon}_{-1}) \ ,\end{aligned} \tag{7.15}$$

where $\vec{\varepsilon}_{\pm1} = \frac{\vec{\varepsilon}_x \pm i\vec{\varepsilon}_y}{\sqrt{2}}$. Operationally, the ellipticity ϵ can be measured as follows: when rotating a polarizer before a photodetector one measures maximum and minimum powers P_{max} and P_{min} as a function of polarizer angle. The ellipticity is then

$$\epsilon = \frac{P_{max} - P_{min}}{P_{max} + P_{min}} \ . \tag{7.16}$$

The formula 7.14 is not written exactly as it appears in Ref. [64] (as Equation 1), but it does

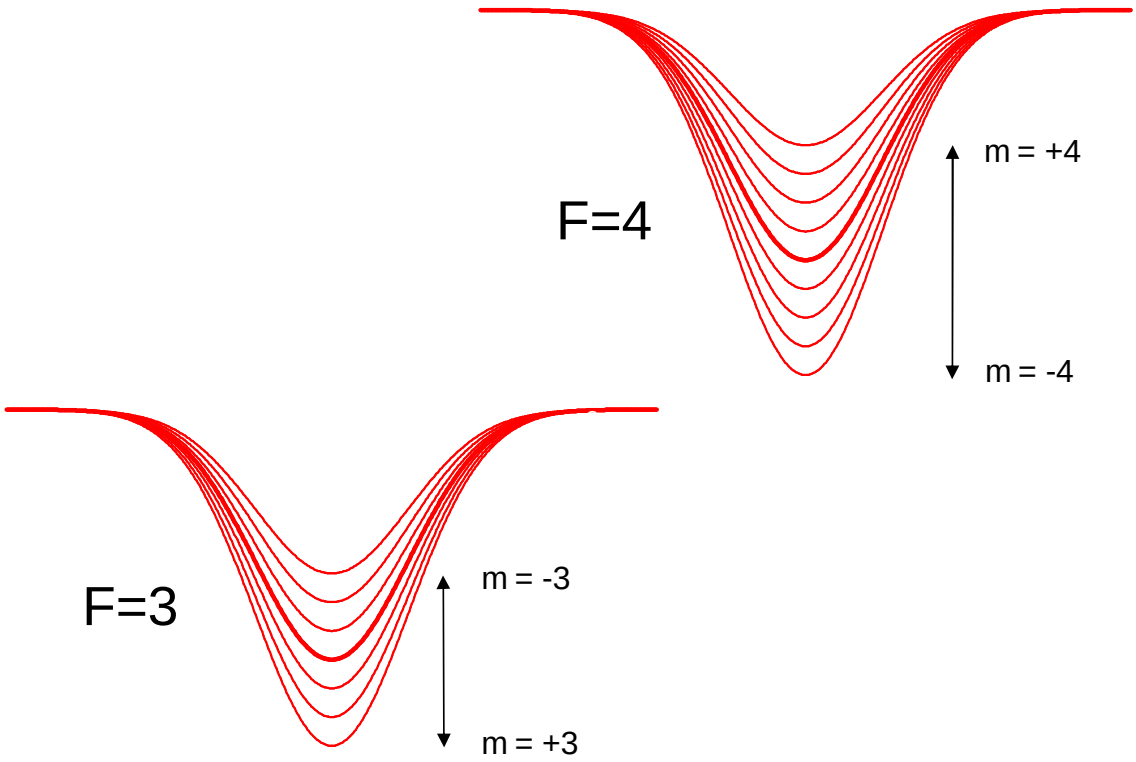

Figure 7.2: Schematic representation of spatially dependent ground-state Stark shifts in an elliptically polarized FORT with a Gaussian intensity profile. Neighboring sublevels m are separated by a constant Zeeman-like splitting at a given point in space, with opposite signs in the two manifolds due to the g_F factors (see text). The thicker lines in each F manifold represent the $m = 0$ state, which is equal to the Stark shift for all sublevels in the case of linear polarization.

agree with it, provided their ambiguously defined quantities γ and λ are for the $D2$ line ($\gamma \equiv \Gamma_{D2}$, $\lambda \equiv 2\pi c/\omega_{D2}$). Figure 7.2 displays an example of these m-dependent ground-state shifts.

It is also worth pointing out that the shifts $U^{(G)}_{F,m,q}$ reduce to a familiar simple form for the case $F = m = 4$ and $q = 1$: the case of the two-level atom. In other words, the "stretched" ground state in circularly polarized light of the correct helicity is only coupled to the state $6P_{3/2}, F = m = 5$, forming an effective two-level system. Equation 7.12 reduces to

$$U^{(G)}_{4,4,1}(\mathbf{r}) = \frac{3\pi c^2}{2\omega^3_{D2}} \frac{\Gamma_{D2}}{\Delta_{D2}} I(\mathbf{r}) \ . \tag{7.17}$$

Although I have presented this result for the case of Cs, it also applies to the analogous stretched state in the other alkali atoms.

One issue that has been neglected above is that even in linear polarization, the ground states are not all shifted by the exact same amount. Due to the hyperfine splitting $\delta_{HFS} = 9.2$ GHz, the detunings of the FORT field from the $D1$ and $D2$ lines are slightly different for each of the ground levels. This causes a difference in the shifts of the hyperfine manifolds of order $\Delta U^{(G)}/U^{(G)} \approx$

$\delta_{HFS}/\Delta_{D1,D2}$. Please note that a precise expression for this can be easily computed by using different resonant frequencies $\Delta_{D1,D2}$ in Equation 7.12 for each of the hyperfine ground states.

7.3 Absolute stark shifts: intensity, power and field amplitudes

7.3.1 Single beam running-wave

Since we already have expressions for the Stark shift as a function of local intensity $I(\mathbf{r})$, we need to relate this to a single beam power P. Consider a beam of wavelength λ_F propagating along z focussed to a waist w_0 (Rayleigh parameter $z_R = \pi w_0^2/\lambda_F$). We have the following expression for the intensity:

$$I(\rho) = I_0 \frac{w_0^2}{w(z)^2} \exp\left[-\frac{2\rho^2}{w(z)^2}\right] , \tag{7.18}$$

where ρ is a cylindrical radial coordinate with respect to the propagation direction, and I_0 is the peak intensity, and $w(z) = w_0\sqrt{1+\frac{z^2}{z_R^2}}$. Since $P = 2\pi \int I(\rho)\rho d\rho$ for all z, we trivially obtain

$$I_0 = \frac{2P}{\pi w_0^2} . \tag{7.19}$$

This intensity corresponds to the maximum Stark shift, and hence gives the FORT depth.

7.3.2 Intracavity FORT

Next consider the case of a standing-wave FORT field of wavelength λ inside a cavity. The task is to compute the peak intracavity intensity based on the transmitted FORT power P_{out}. The additional quantities needed are the transmission coefficient T of the output mirror at λ and the beam waist, w_0. For all the experiments described in this thesis [27, 35, 36, 33] $\lambda_F = 935.6$ nm, for which the cavity finesse is $\mathcal{F} = 2.2 \times 10^3$, well below its maximum reflectivity. Assuming a symmetric cavity and no scattering or absorption in the mirrors, we calculate $T = \pi/\mathcal{F} = 1.4 \times 10^{-3}$ [59]. We justify the assumption of zero scattering and absorption by noting that these effects amount to $A \approx 2 \times 10^{-6}$ at $\lambda_0 = 852$ nm [59], and that they should be approximately the same (or at least negligible compared to T) at λ_F. Section 7.3 of Ref. [41] (among numerous others) contains the requisite formalism on how to determine w_0, so I omit the details here.

We obtain the following expression for the peak intensity:

$$I_0 = \frac{8P_{out}}{T\pi w_0^2} . \tag{7.20}$$

Comparing this to Equation 7.19 and noting that the output power is related to the one-way intra-

cavity power by $P_{out} = TP_{in}^{(1-way)}$, we see there is an additional factor of four in this standing wave case relative to a running wave. The physical explanation is that the antinode of the standing wave has twice the electric field amplitude of the one-way case, and therefore four times the intensity. Please note that the Stark shifts computed in Refs. [25, 26] do not incorporate this standing-wave factor, and after careful evaluations and cross-checks with similar calculations done by others, we conclude that the older calculations are incorrect. In addition, this does not seem to be the only discrepancy between those earlier calculations and the ones presented here.

7.4 Excited states, transition shifts and the state-insensitive trap

In order to illustrate the capabilities of the formalism described above, we now present some more general results which include excited state shifts.

7.4.1 A simple model: $6S$, $6P$ and $6D$ levels only

We begin by concentrating on the ground and excited states of the commonly employed $6S - 6P$ transitions. The shifts to the ground states are dominated by contributions from the $6P$ levels, and the $6P$ states themselves are mostly shifted by $6S$ and by the higher-lying $6D$ states [40]. Therefore the inclusion of only these three manifolds is sufficient for most Stark shift calculations. Please note that the exclusion of higher-lying states and counter-rotating terms (see below) accounts for the small discrepancies between the simplified results of this section and those of Ref. [27] which use the full formalism (see Fig. 3.1 of this thesis).

The reduced matrix elements for these calculations have been obtained from two sources. For the $6S - 6P$ transitions, I have used the notes of Steck [43], with the proper adjustment to the normalization. For the $6P - 6D$ transitions, I have used the numbers from Table 6.2 of Christina Hood's thesis [40] (they are in atomic units ea_0). It turns our that her convention for normalizing the reduced matrix elements is compatible with the formalism presented here. Please see Section 7.1 for further discussion of these conventions.

Figure 7.3 shows the Stark shifts of the ground and excited states of the $D2$ line within this restricted set of included levels, where for $6P_{3/2}$ we have chosen the $F' = 4$ manifold. The intensity chosen corresponds to the approximate power typically used in our experiments. Although within the approximation of negligible hyperfine splitting the ground states are all degenerate for $q = 0$ (a linearly polarized FORT), the $6P_{3/2}$ excited states are not, as is clearly evidenced in Fig. 7.3. See Section 7.4.3 below for further discussion and details. We also include the shifts for the $D1$ line in Fig. 7.4.

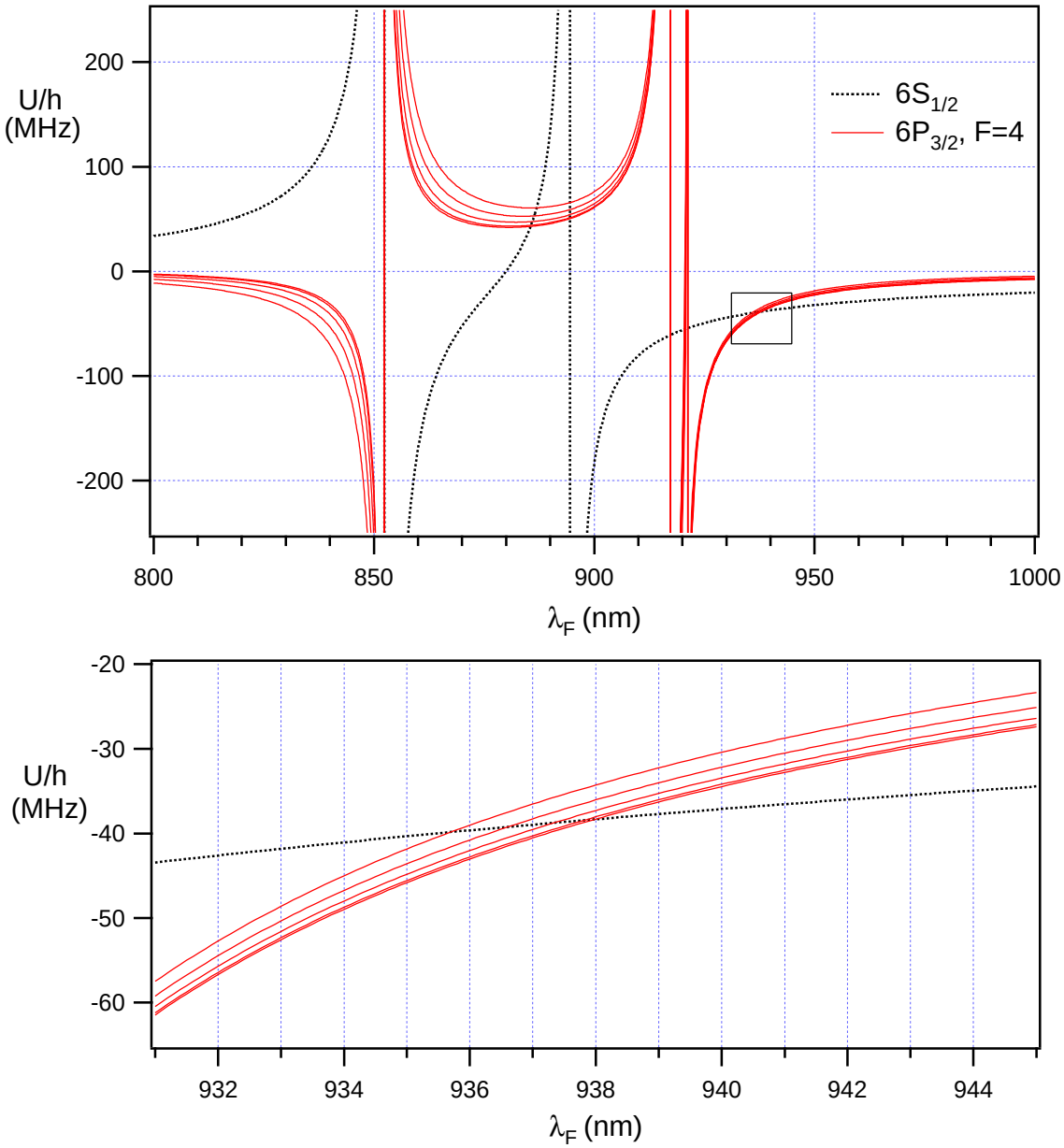

Figure 7.3: AC Stark shifts of ground and excited states of the $D2$ line in Cs for a linearly polarized FORT ($q = 0$), and an intensity of $I_0 = 2.92 \times 10^9$ W/m^2. This corresponds to a cavity output power of 1 mW for the cavity parameters of our experiments (see text). For the ground states, all sublevels of both hyperfine manifolds have nearly the same shift, and for the $6P_{3/2}$ excited states all sublevels of the $F' = 4$ hyperfine level have been plotted. These shifts have been computed considering only the $6S$, $6P$ and $6D$ levels, without counter-rotating terms. The Stark shifts for the ground and excited states are approximately equal around $\lambda_F \approx 937$ nm, as indicated by the small box in the upper panel. The lower panel is a blowup of this region.

7.4.2 A more complete model: Inclusion of higher-lying excited states and the counter-rotating terms

We have also investigated two contributions to the Stark shifts that are often neglected: higher-lying excited states and the counter-rotating terms [122]. We were also able to compute the shifts of the

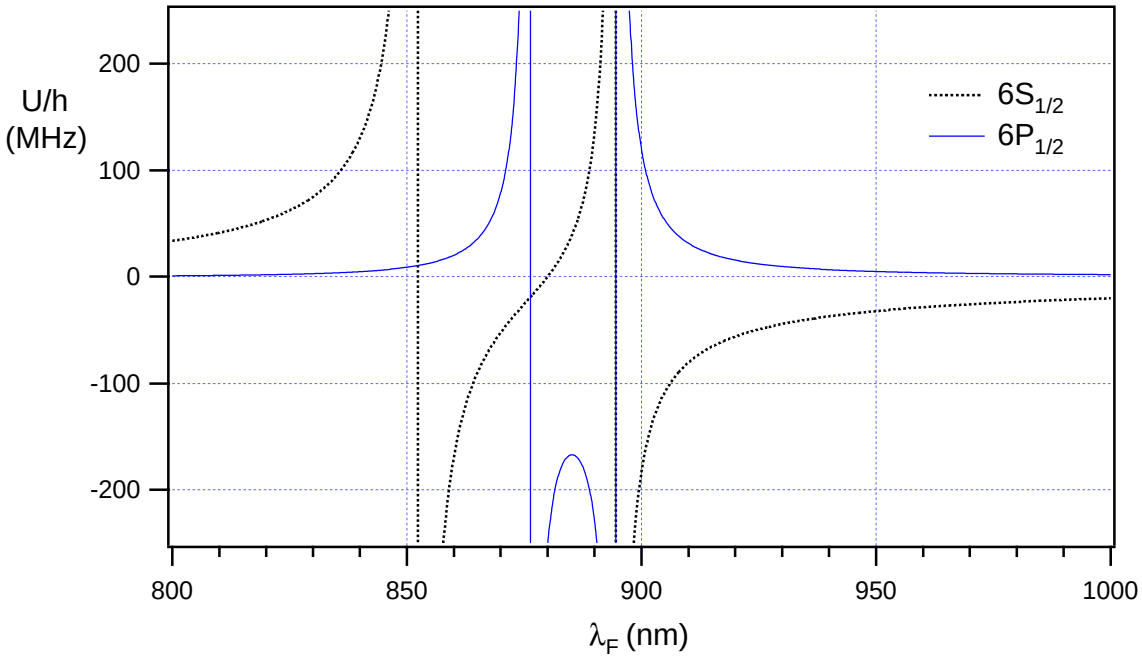

Figure 7.4: AC Stark shifts of ground and excited states of the D1 line in Cs for a linearly polarized FORT ($q = 0$). The intensity is the same as in Fig. 7.3. All sublevels within both hyperfine manifolds are degenerate, for each of $6S_{1/2}$ and $6P_{1/2}$. These shifts have been computed considering only the $6S$, $6P$ and $6D$ levels, without counter-rotating terms.

$5D$ states, which may be of interest for cooling applications.

We begin by tabulating relevant wavelengths and oscillator strengths for various transitions. The tables are organized such that each level for which we wish to compute shifts gets one table for each set of higher-lying states nL. For example, Table 7.1 lists the information for the $6S_{1/2} - nP$ transitions. Using these lifetimes and wavelengths, the reduced matrix elements necessary for computation of the Stark shifts can be computed via Equation 7.8.

Level nP	$\lambda_{1/2}$ (nm)	$\tau_{1/2}$ (μs)	$\lambda_{3/2}$ (nm)	$\tau_{3/2}$ (μs)
$6P$	894.6	0.03494	852.4	0.03051
$7P$	459.3	1.308	455.5	0.5787
$8P$	388.9	10.17	387.6	2.542
$9P$	361.7	45.94	361.2	6.852
$10P$	348.0	153.1	347.7	14.35
$11P$	340.0	418.0	339.8	25.70

Table 7.1: Partial lifetimes and wavelengths for decays $\mathbf{nP_J \rightarrow 6S_{1/2}}$. τ_J is the partial lifetime of the nP_J state decaying to $6S_{1/2}$, at wavelength λ_J. Data for $6P \rightarrow 6S$ is obtained from Ref. [43]. For $(7-11)P \rightarrow 6S$, oscillator strengths are obtained from Ref. [123] (Table 1, column b), and wavelengths taken from Ref. [58], Table 4.

The counter-rotating terms can be included by the following substitution involving the detunings

Level nS	$\lambda_{1/2}$ (nm)	$\tau_{1/2}$ (μs)
$7S$	469.5	0.07529
$8S$	794.4	0.2599
$9S$	658.8	0.5533
$10S$	603.4	0.9924
$11S$	574.6	1.607
$12S$	557.3	2.428
$13S$	546.3	3.490
$14S$	538.5	4.809
$15S$	532.9	6.431

Table 7.2: Partial lifetimes and wavelengths for decays $\mathbf{nS_{1/2} \rightarrow 6P_{3/2}}$. $\tau_{1/2}$ is the partial lifetime of the $nS_{1/2}$ state decaying to $6P_{3/2}$, at wavelength $\lambda_{1/2}$. All wavelengths and oscillator strengths are obtained from Ref. [58], Table 4.

Level nD	$\lambda_{3/2}$ (nm)	$\tau_{3/2}$ (μs)	$\lambda_{5/2}$ (nm)	$\tau_{5/2}$ (μs)
$5D$	3612.7	10.090	3489.2	1.433
$6D$	921.1	0.3466	917.2	0.0587
$7D$	698.3	709.7	697.3	0.1198
$8D$	621.7	1.284	621.3	0.2170
$9D$	584.7	2.131	584.5	0.3587
$10D$	563.7	3.290	563.5	0.5527
$11D$	550.4	4.807	550.3	0.8063

Table 7.3: Partial lifetimes and wavelengths for decays $\mathbf{nD_J \rightarrow 6P_{3/2}}$. τ_J is the partial lifetime of the nD_J state decaying to $6P_{3/2}$, at wavelength λ_J. All wavelengths are taken from Ref. [58], Table 4. The oscillator strengths for $5D \rightarrow 6P$ are from Ref. [58], for $6D \rightarrow 6P$ from Ref. [40], and for $(7-11)D \rightarrow 6P$ from Ref. [123].

Level nF	$\lambda_{5/2}$ (nm)	$\tau_{5/2}$ (μs)
$4F$	1002.5	0.07689
$5F$	801.8	0.1291
$6F$	722.9	0.2117
$7F$	682.5	0.3273
$8F$	658.6	0.4829
$9F$	643.2	0.6791
$10F$	632.6	0.9249
$11F$	625.0	1.227
$12F$	619.4	1.589
$13F$	615.0	2.069
$14F$	611.7	2.646
$15F$	609.0	3.078
$16F$	606.8	3.747

Table 7.4: Partial lifetimes and wavelengths for decays $\mathbf{nF_{5/2} \rightarrow 5D_{3/2}}$. $\tau_{5/2}$ is the partial lifetime of the $nF_{5/2}$ state decaying to $5D_{3/2}$, at wavelength $\lambda_{5/2}$. All wavelengths and oscillator strengths are obtained from Ref. [58], Table 4.

[124]:

$$\frac{1}{\Delta_r} = \frac{1}{\omega_L - \omega_r} \rightarrow -\left(\frac{1}{\omega_r - \omega_L} + \frac{1}{\omega_r + \omega_L}\right) , \tag{7.21}$$

Level nP	$\lambda_{1/2}$ (nm)	$\tau_{1/2}$ (μs)	$\lambda_{3/2}$ (nm)	$\tau_{3/2}$ (μs)
$7P$	1375.9	0.825	1324.4	11.90
$8P$	891.8	2.922	885.3	43.20
$9P$	760.9	6.889	758.4	106.1
$10P$	702.7	13.220	701.3	210.1

Table 7.5: Partial lifetimes and wavelengths for decays $\mathbf{nP_J \rightarrow 5D_{3/2}}$. τ_J is the partial lifetime of the nP_J state decaying to $5D_{3/2}$, at wavelength λ_J. All wavelengths and oscillator strengths are obtained from Ref. [58], Table 4.

Level	Simple Model	Full Model (No CR)	Full Model (Incl. CR)
$6S_{1/2}$	1.0000	1.0005	1.035
$6P_{3/2}$, $F' = 4,\ m = 0$	1.105	1.010	1.072
$6P_{3/2}$, $F' = 4,\ m = \pm 4$	1.005	0.865	0.935
$F' = 4$ spread	0.100	0.145	0.138

Table 7.6: The effect of additional terms on the $6S_{1/2}$ and $6P_{3/2}$ Stark shifts in Cs for $\lambda_F = 935.6$ nm, relative to the simple model described in Section 7.4.1. The second column shows the impact of the inclusion of additional higher-lying S, P and D levels (see text). The third column includes the effect of the counter-rotating terms.

where ω_r is the resonant frequency of a given $J - J'$ transition (regardless of whether its energy lies above or below the state of interest, i.e., $r = h, l$), and this substitution is made for every term in both summations in Equation 7.4.

Table 7.6 summarizes the effect of including the additional higher-lying levels and the counter-rotating terms. We also provide Fig. 7.5, which plots the ground and excited state shifts for all magnetic sublevels of the $D2$ transition at $\lambda_F = 935.6$ nm, including both of these contributions.

In addition, we plot in Fig. 7.6 the shifts to the $5D_{3/2}$ levels. Since the $6S - 5D$ transition at 690 nm is not dipole-allowed, there may be potential to use it for narrow-line Doppler cooling. At our FORT wavelength, however, the $5D$ states are shifted up, possibly precluding the success of such a cooling scheme.

7.4.3 The state-insensitive trap

As evidenced in Fig. 7.3, the ac Stark shifts for $6S_{1/2}$ and $6P_{3/2}$ are nearly equal around $\lambda_F \approx$ 936 nm. This is in marked contrast to the conventional dipole trap, where the excited state is shifted *up* with the same magnitude as the (negative) ground-state shift [40, 68]. In this more typical regime, the transition frequency of the $D2$ line is increased by twice the trap depth at the location of peak intensity. We have referred to our FORT at $\lambda_F = 935.6$ nm as a state-insensitive trap, and have exploited this feature significantly in our experiments.

This state-insensitive trap provides tremendous advantages in two main ways. The first is from a spectroscopic point of view: the transition shifts are reduced over tenfold compared to the standard

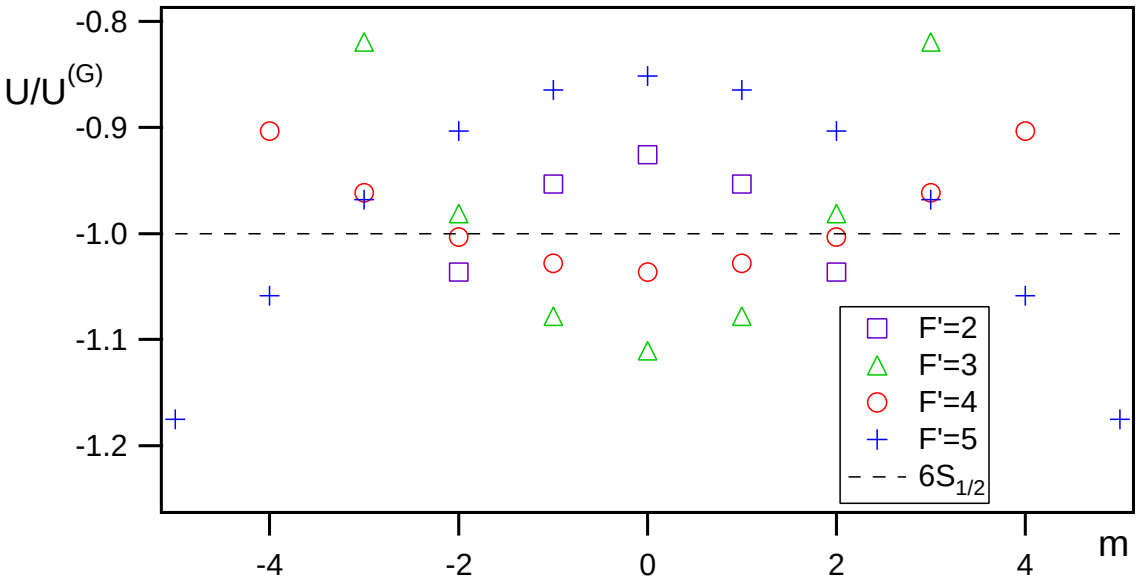

Figure 7.5: AC Stark shifts of all magnetic sublevels m in the $6P_{3/2}$ excited manifold. The scaling is relative to the ground-state shift $U^{(G)}$, and the wavelength is $\lambda_F = 935.6$ nm. The dashed line represents the (degenerate) ground-state shift of all sublevels of both $6S_{1/2}$ hyperfine manifolds. These shifts have been computed considering the $6S - 15S$, $6 - 11P$ and $5 - 11D$ levels, including the counter-rotating terms. This figure contains the same data as Fig. 1 of Ref. [27], plotted with a different axis range.

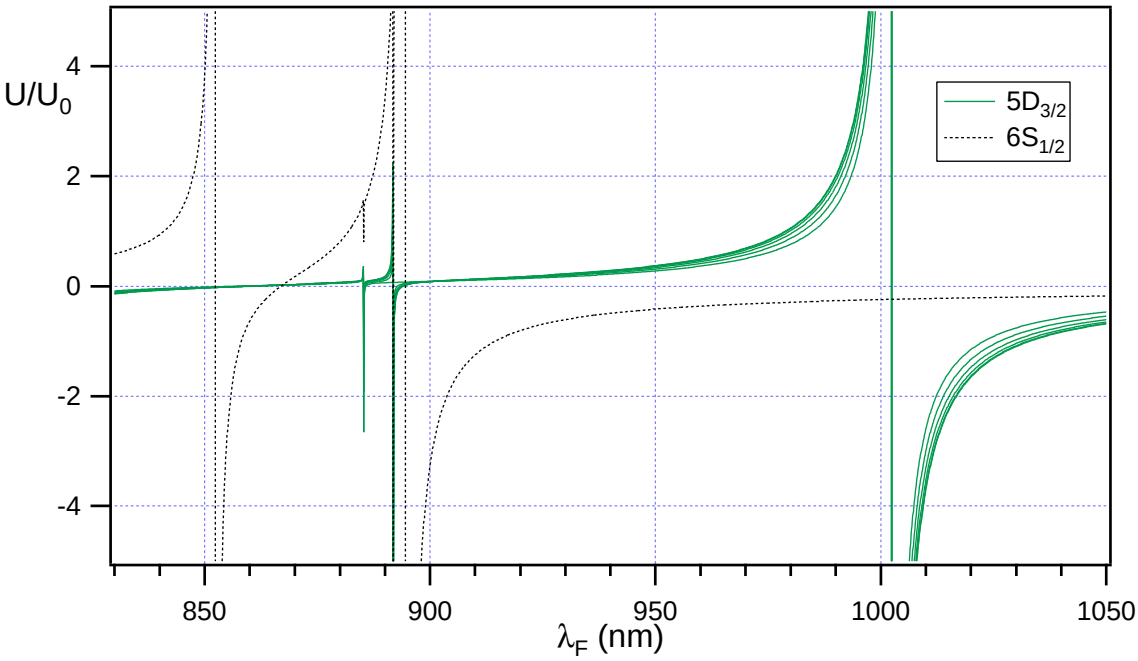

Figure 7.6: AC Stark shifts of all magnetic sublevels m in the $5D_{3/2}$ excited manifold, plotted vs. FORT wavelength λ_F. The scaling is relative to the ground-state shift $U_0 \equiv U^{(G)}(\lambda_F = 935.6$ nm). These shifts have been computed considering the $6 - 11P$ and $4 - 16F$ levels, including the counter-rotating terms.

dipole trap. Second, the fact that the excited state has a negative shift similar in magnitude to that of the ground state means force fluctuations are greatly reduced for driven atoms in the FORT. In other words, when an atom is pumped to the excited state, the dipole force does not switch sign, as it does in a conventional FORT, and furthermore its magnitude stays nearly constant.

However, as shown in Fig. 7.5, the $6P_{3/2}$ excited states are not all shifted equally. At our chosen wavelength of 935.6 nm, the magnetic sublevels are split by as much as $\approx \pm 15\%$ relative to the ground-state shift. In order to discuss the implications of this splitting, we return to the discussion of the spectroscopic issues. Note that for the particular trap depth chosen in our experiments (which corresponds to about $U^{(G)}/k_B \approx 2.2$ mK), the transition shifts are at most around 8 MHz. If in future endeavors the trap depth can be lowered thanks to improved cooling techniques, this transition shift could conceivably be reduced to well below the natural linewidth $\Gamma_{D2} = 5.2$ MHz. Indeed, a 200 μK trap would give transition shifts of below 1 MHz, almost negligible from the point of view of direct spectroscopy.

It is also worthwhile to point out that the quantization axis for the m levels here is the *polarization* direction of the FORT field. In any scheme where we consider alternate quantization axes, such as along the cavity axis, it is important to bear in mind that the excited states are "mixed" in this basis by the FORT. The implications of this mixing would only be important for situations where the excited states are populated, so some schemes would be unaffected (presumably including Raman transitions and adiabatic passage). However optical pumping, for example, may not function as expected if mixing timescales (of order MHz for these typical FORT powers) are comparable to the excited state decay rates.

Bibliography

[1] W. Neuhauser, M. Hohenstatt, P. E. Toschek, and H. Dehmelt. Localized visible Ba^+ mono-ion oscillator. *Phys. Rev. A*, 22:1137, 1980.

[2] D. J. Wineland and W. M. Itano. Spectroscopy of a single Mg^+ ion. *Phys. Lett. A*, 82:75, 1981.

[3] S. Chu. Nobel lecture: The manipulation of neutral particles. *Rev. Mod. Phys.*, 70:685, 1998.

[4] W. D. Phillips. Nobel lecture: Laser cooling and trapping of neutral atoms. *Rev. Mod. Phys.*, 70:721, 1998.

[5] C. Cohen-Tannoudji. Nobel lecture: Manipulating atoms with photons. *Rev. Mod. Phys.*, 70:685, 1998.

[6] Z. Hu and H. J. Kimble. Observation of a single atom in a magneto-optical trap. *Opt. Lett.*, 19:1888, 1994.

[7] F. Ruschewitz, D. Bettermann, J. L. Peng, and W. Ertmer. Statistical investigations on single trapped neutral atoms. *Europhys. Lett.*, 34:651, 1996.

[8] D. Haubrich, H. Schadwinkel, F. Strauch, B. Ueberholz, R. Wynands, and D. Meschede. Observation of individual neutral atoms in magnetic and magneto-optical traps. *Europhys. Lett.*, 34:663, 1996.

[9] P. A. Willems, R. A. Boyd, J. L. Bliss, and K. G. Libbrecht. Stability of magneto-optical traps with large field gradients: Limits on the tight confinement of single atoms. *Phys. Rev. Lett.*, 78:1660, 1997.

[10] D. Frese, B. Ueberholz, S. Kuhr, W. Alt, D. Schrader, V. Gomer, and D. Meschede. Single atoms in an optical dipole trap: Towards a deterministic source of cold atoms. *Phys. Rev. Lett.*, 85:3777, 2000.

[11] N. Schlosser, G. Reymond, I. Protsenko, and P. Grangier. Sub-poissonian loading of single atoms in a microscopic dipole trap. *Nature*, 411:1024, 2001.

[12] M. A. Nielsen and I. L. Chuang. *Quantum computation and quantum information.* Cambridge University Press, Cambridge, 2000.

[13] F. De Martini and C. Monroe, editors. *Experimental Quantum Computation and Information: Proceedings of the International School of Physics "Enrico Fermi", Course CXLVIII.* IOS Press, Amsterdam, 2002.

[14] D. P. DiVincenzo. The physical implementation of quantum computation. *Fortschr. Phys.*, 48:9, 2000, quant-ph/0002077.

[15] D. Kielpinski, C. Monroe, and D. J. Wineland. Architecture for a large-scale ion-trap quantum computer. *Nature*, 417:709, 2002.

[16] D. Leibfried, B. L. DeMarco, V. Meyer, D. Lucas, M. Barrett, J. Britton, W. M. Itano, B. M. Jelenkovic, C. Langer, T. Rosenband, and D. J. Wineland. Experimental demonstration of robust, high-fidelity geometric two ion-qubit phase gate. *Nature*, 422:412, 2003.

[17] F. Schmidt-Kaler, H. Hffner, M. Riebe, S. Gulde, G. P. T. Lancaster, T. Deuschle, C. Becher, C. F. Roos, J. Eschner, and R. Blatt. Realization of the Cirac-Zoller controlled-NOT quantum gate. *Nature*, 422:408, 2003.

[18] Q. A. Turchette, C. J. Hood, W. Lange, H. Mabuchi, and H. J. Kimble. Measurement of conditional phase shifts for quantum logic. *Phys. Rev. Lett.*, 75:4710, 1995.

[19] P. Berman, editor. *Cavity Quantum Electrodynamics.* Academic Press, San Diego, 1994.

[20] H. J. Kimble. Strong interactions of single atoms and photons in cavity QED. *Physica Scripta*, T76:127, 1998.

[21] J. I. Cirac, P. Zoller, H. J. Kimble, and H. Mabuchi. Quantum state transfer and entanglement distribution among distant nodes in a quantum network. *Phys. Rev. Lett.*, 78:3221, 1997.

[22] H.-J. Briegel, S. J. van Enk, J. I. Cirac, and P. Zoller. Quantum networks I: Entangling particles at separate locations. In D. Bouwmeester, A. Ekert, and A. Zeilinger, editors, *The Physics of Quantum Information*, page 192. Springer-Verlag, Berlin, 2000.

[23] H. Mabuchi and A. C. Doherty. Cavity quantum electrodynamics: Coherence in context. *Science*, 298:1372, 2002.

[24] C. J. Hood, T. W. Lynn, A. C. Doherty, A. S. Parkins, and H. J. Kimble. The atom-cavity microscope: Single atoms bound in orbit by single photons. *Science*, 287:1447, 2000.

[25] D. W. Vernooy. *Cold atoms in cavity QED for quantum information processing.* PhD thesis, California Institute of Technology, 2000.

[26] J. Ye, D. W. Vernooy, and H. J. Kimble. Trapping of single atoms in cavity QED. *Phys. Rev. Lett.*, 83:4987, 1999.

[27] J. McKeever, J. R. Buck, A. D. Boozer, A. Kuzmich, H.-C. Naegerl, D. M. Stamper-Kurn, and H. J. Kimble. State-insensitive cooling and trapping of single atoms in an optical cavity. *Phys. Rev. Lett.*, 90:133602, 2003.

[28] J. R. Buck. *Cavity QED in Microsphere and Fabry-Perot Cavities.* PhD thesis, California Institute of Technology, 2003.

[29] A. B. Mundt, A. Kreuter, C. Becher, D. Leibfried, J. Eschner, F. Schmidt-Kaler, and R. Blatt. Coupling a single atomic quantum bit to a high finesse optical cavity. *Phys. Rev. Lett.*, 89:103001, 2002.

[30] G. R. Guthöhrlein, M. Keller, K. Hayasaka, W. Lange, and H. Walther. A single ion as a nanoscopic probe of an optical field. *Nature*, 414:49, 2001.

[31] P. Maunz, T. Puppe, I. Schuster, N. Syassen, P. W. H. Pinkse, and G. Rempe. Cavity cooling of a single atom. *Nature*, 428:50, 2004.

[32] J. A. Sauer, K. M. Fortier, M. S. Chang, C. D. Hamley, and M. S. Chapman. Cavity QED with optically transported atoms. 2003, quant-ph/0309052.

[33] J. McKeever, J. R. Buck, A. D. Boozer, and H. J. Kimble. Cavity QED "by the numbers". 2004, quant-ph/0403121.

[34] S. Kuhr, W. Alt, D. Schrader, M. Mller, V. Gomer, and D. Meschede. Deterministic delivery of a single atom. *Science*, 293:278, 2001.

[35] J. McKeever, A. Boca, A. D. Boozer, J. R. Buck, and H. J. Kimble. Experimental realization of a one atom laser in the regime of strong coupling. *Nature*, 425:268, 2003.

[36] J. McKeever, A. Boca, A. D. Boozer, R. Miller, J. R. Buck, A. Kuzmich, and H. J. Kimble. Deterministic generation of single photons from one atom trapped in a cavity. *Science*, 303:1992, 2004. Published online 26 February 2004; 10.1126/science.1095232.

[37] A. S. Parkins and H. J. Kimble. Quantum state transfer between motion and light. *J. Opt. B: Quantum Semiclass. Opt.*, 1:496, 1999.

[38] H. Mabuchi. *Continuous observation of quantum dynamics.* PhD thesis, California Institute of Technology, 1998.

[39] H. Mabuchi, J. Ye, and H. J. Kimble. Full observation of single-atom dynamics in cavity QED. *Appl. Phys. B*, 68:1095, 1999.

[40] C. J. Hood. *Real-time measurement and trapping of single atoms by single photons.* PhD thesis, California Institute of Technology, 2000.

[41] T. W. Lynn. *Measurement and control of individual quanta in cavity QED.* PhD thesis, California Institute of Technology, 2003.

[42] T. Yabuzaki, T. Mitsui, and U. Tanaka. New type of high-resolution spectroscopy with a diode laser. *Phys. Rev. Lett.*, 67:2453, 1991.

[43] D. A. Steck. Cesium D line data. available at http://steck.us/alkalidata, 2003.

[44] R. W. P. Drever, J. L. Hall, F. V. Kowalski, J. Hough, G. M. Ford, A. J. Munley, and H. Ward. Laser phase and frequency stabilization using an optical-resonator. *Appl. Phys. B*, 31:97, 1983.

[45] J. H. Shirley. Modulation transfer processes in optical heterodyne saturation spectroscopy. *Opt. Lett.*, 7:537, 1982.

[46] C. E. Wieman and L. Hollberg. Using diode lasers for atomic physics. *Rev. Sci. Instrum.*, 62:1, 1991.

[47] H. J. Metcalf and P. van der Straten. *Laser Cooling and Trapping.* Springer-Verlag, New York, 1999.

[48] S.J. van Enk, J. McKeever, H. J. Kimble, and J. Ye. Cooling of a single atom in an optical trap inside a resonator. *Phys. Rev. A*, 64:013407, 2001.

[49] A. C. Doherty, T. W. Lynn, C. J. Hood, and H. J. Kimble. Trapping of single atoms with single photons in cavity QED. *Phys. Rev. A*, 63:013401, 2000.

[50] P. W. H. Pinkse, T. Fischer, P. Maunz, and G. Rempe. Trapping an atom with single photons. *Nature*, 404:365, 2000.

[51] T. Pellizzari, S. A. Gardiner, J. I. Cirac, and P. Zoller. Decoherence, continuous observation, and quantum computing: A cavity QED model. *Phys. Rev. Lett.*, 75:3788, 1995.

[52] S. J. van Enk, J. I. Cirac, and P. Zoller. Photonic channels for quantum communication. *Science*, 279:205, 1998.

[53] C. Cabrillo, J. I. Cirac, P. García-Fernández, and P. Zoller. Creation of entangled states of distant atoms by interference. *Phys. Rev. A*, 59:1025, 1999.

[54] S. Bose, P. L. Knight, M. B. Plenio, and V. Vedral. Proposal for teleportation of an atomic state via cavity decay. *Phys. Rev. Lett.*, 83:5158, 1999.

[55] H. J. Kimble et al. In R. Blatt et al., editors, *Laser Spectroscopy XIV*, page 80. World Scientific, Singapore, 1999.

[56] H. Katori, T. Ido, and M. Kuwata-Gonokami. Optimal design of dipole potentials for efficient loading of Sr atoms. *J. Phys. Soc. Japan*, 68:2479, 1999.

[57] T. Ido, Y. Isoya, and H. Katori. Optical-dipole trapping of Sr atoms at a high phase-space density. *Phys. Rev. A*, 61:061403, 2000.

[58] M. Fabry and J. R. Cussenot. Détermination théorique et expérimentale des forces d'oscillateur des transitions de l'atome de césium. *Can. J. Phys.*, 54:836, 1976.

[59] C. J. Hood, H. J. Kimble, and J. Ye. Characterization of high-finesse mirrors: Loss, phase shifts, and mode structure in an optical cavity. *Phys. Rev. A*, 64:033804, 2001.

[60] H. Mabuchi, Q. A. Turchette, M. S. Chapman, and H. J. Kimble. Real-time detection of individual atoms falling through a high-finesse optical cavity. *Opt. Lett.*, 21:1393, 1996.

[61] C. J. Hood, M. S. Chapman, T. W. Lynn, and H. J. Kimble. Real-time cavity QED with single atoms. *Phys. Rev. Lett.*, 80:4157, 1998.

[62] T. A. Savard, K. M. O'Hara, and J. E. Thomas. Laser-noise-induced heating in far-off resonance optical traps. *Phys. Rev. A*, 56:R1095, 1997.

[63] C. W. Gardiner, J. Ye, H.-C. Nägerl, and H. J. Kimble. Evaluation of heating effects on atoms trapped in an optical trap. *Phys. Rev. A*, 61:045801, 2000.

[64] K. L. Corwin, S. J. M. Kuppens, D. Cho, and C. E. Wieman. Spin-polarized atoms in a circularly polarized optical dipole trap. *Phys. Rev. Lett.*, 83:1311, 1999.

[65] R. A. Cline, J. D. Miller, M. R. Matthews, and D. J. Heinzen. Spin relaxation of optically trapped atoms by light scattering. *Opt. Lett.*, 19:207, 1994.

[66] A. Kuhn, M. Hennrich, and G. Rempe. Deterministic single photon source for distributed quantum networking. *Phys. Rev. Lett.*, 89:067901, 2002.

[67] D. Boiron, A. Michaud, P. Lemonde, Y. Castin, C. Salomon, S. Weyers, K. Szymaniec, L. Cognet, and A. Clairon. Laser cooling of cesium atoms in gray optical molasses down to 1.1 μK. *Phys. Rev. A*, 53:R3734, 1996.

[68] R. Grimm, M. Weidemüller, and Yu. B. Ovchinnikov. Optical dipole traps for neutral atoms. *J. Adv. At. Mol. Opt. Phys.*, 42:95, 2000, physics/9902072.

[69] L. Mandel and E. Wolf. *Optical Coherence and Quantum Optics.* Cambridge Univ. Press, Cambridge, 1995.

[70] L. M. Duan and H. J. Kimble. Efficient engineering of multiatom entanglement through single-photon detections. *Phys. Rev. Lett.*, 90:253601, 2003.

[71] J. Hong and H.-W. Lee. Quasideterministic generation of entangled atoms in a cavity. *Phys. Rev. Lett.*, 89:237901, 2002.

[72] A. S. Sorensen and K. Molmer. Probabilistic generation of entanglement in optical cavities. *Phys. Rev. Lett.*, 90:127903, 2003.

[73] P. Maunz, T. Puppe, T. Fischer, P. W. H. Pinkse, and G. Rempe. Emission pattern of an atomic dipole in a high-finesse optical cavity. *Opt. Lett.*, 28:46, 2003.

[74] A. D. Boozer, A. Boca, J. R. Buck, J. McKeever, and H. J. Kimble. Comparison of theory and experiment for a one-atom laser in a regime of strong coupling. 2003, quant-ph/0309133.

[75] Y. Mu and C. M. Savage. One-atom lasers. *Phys. Rev. A*, 46:5944, 1992.

[76] C. Ginzel, H.-J. Briegel, U. Martini, B.-G. Englert, and A. Schenzle. Quantum optical master equations: The one-atom laser. *Phys. Rev. A*, 48:732, 1993.

[77] T. Pellizzari and H. Ritsch. Preparation of stationary Fock states in a one-atom Raman laser. *Phys. Rev. Lett.*, 72:3973, 1994.

[78] T. Pellizzari and H. Ritsch. Photon statistics of the three-level one-atom laser. *J. Mod. Opt.*, 41:609, 1994.

[79] P. Horak, K. M. Gheri, and H. Ritsch. Quantum dynamics of a single-atom cascade laser. *Phys. Rev. A*, 51:3257, 1995.

[80] G. M. Meyer, H.-J. Briegel, and H. Walther. Ion-trap laser. *Europhys. Lett.*, 37:317, 1997.

[81] M. Löffler, G. M. Meyer, and H. Walther. Spectral properties of the one-atom laser. *Phys. Rev. A*, 55:3923, 1997.

[82] G. M. Meyer, M. Löffler, and H. Walther. Spectrum of the ion-trap laser. *Phys. Rev. A*, 56:R1099, 1997.

[83] G. M. Meyer and H.-J. Briegel. Pump-operator treatment of the ion-trap laser. *Phys. Rev. A*, 58:3210, 1998.

[84] B. Jones, S. Ghose, J. P. Clemens, P. R. Rice, and L. M. Pedrotti. Photon statistics of a single atom laser. *Phys. Rev. A*, 60:3267, 1999.

[85] S. Ya. Kilin and T. B. Karlovich. Single-atom laser: Coherent and nonclassical effects in the regime of a strong atom-field correlation. *JETP*, 95:805, 2002.

[86] M. Sargent III, M. O. Scully, and W. E. Lamb, Jr. *Laser Physics.* Addison-Wesley, Reading Mass., 1974.

[87] H. Haken. *Laser Theory.* Springer-Verlag, Berlin, 1984.

[88] H. J. Carmichael. *Statistical Methods in Quantum Optics 1.* Springer-Verlag, Berlin, 1999.

[89] C. W. Gardiner and P. Zoller. *Quantum Noise.* Springer-Verlag, Berlin, 2000.

[90] G. Raithel, C. Wagner, H. Walther, L. M. Narducci, and M. O. Scully. In P. Berman, editor, *Cavity Quantum Electrodynamics*, page 57. Academic Press, San Diego, 1994.

[91] S. Haroche and J. M. Raimond. In P. Berman, editor, *Cavity Quantum Electrodynamics*, page 123. Academic Press, San Diego, 1994.

[92] P. Meystre. In E. Wolf, editor, *Progress in Optics*, volume XXX, page 261. Elsevier Science Publishers B.V., Amsterdam, 1992.

[93] K. An and M. S. Feld. Semiclassical four-level single-atom laser. *Phys. Rev. A*, 56:1662, 1997.

[94] R. K. Chang and A. J. Campillo, editors. *Optical Processes in Microcavities.* World Scientific, Singapore, 1996.

[95] K. J. Vahala. Optical microcavities. *Nature*, 2003.

[96] P. R. Rice and H. J. Carmichael. Photon statistics of a cavity-QED laser: A comment on the laser-phase-transition analogy. *Phys. Rev. A*, 50:4318, 1994.

[97] S. M. Tan. A computational toolbox for quantum and atomic optics. *J. Opt. B: Quantum Semiclass. Opt.*, 1, 1999.

[98] N. Lutkenhaus. Security against individual attacks for realistic quantum key distribution. *Phys. Rev. A*, 61:052304, 2000.

[99] I. L. Chuang and Y. Yamamoto. Simple quantum computer. *Phys. Rev. A*, 52:3489, 1995.

[100] E. Knill, R. Laflamme, and G. Milburn. A scheme for efficient quantum computation with linear optics. *Nature*, 409:46, 2001.

[101] L.-M. Duan and H. J. Kimble. Scalable photonic quantum computation through cavity-assisted interaction. *Phys. Rev. Lett.*, 92:127902, 2004.

[102] J. F. Clauser. Experimental distinction between the quantum and classical field-theoretic predictions for the photoelectric effect. *Phys. Rev. D*, 9:853, 1974.

[103] H. J. Kimble, M. Dagenais, and L. Mandel. Photon antibunching in resonance fluorescence. *Phys. Rev. Lett.*, 39:691, 1977.

[104] P. Grangier, G. Roger, and A. Aspect. Experimental-evidence for a photon anticorrelation effect on a beam splitter − a new light on single-photon interferences. *Europhys. Lett.*, 1:173, 1986.

[105] F. Diedrich and H. Walther. Nonclassical radiation of a single stored ion. *Phys. Rev. Lett.*, 58:203, 1987.

[106] T. Basché, W. E. Moerner, M. Orrit, and H. Talon. Photon antibunching in the fluorescence of a single dye molecule trapped in a solid. *Phys. Rev. Lett.*, 69:1516, 1992.

[107] B. Lounis and W. E. Moerner. Single photons on demand from a single molecule at room temperature. *Nature*, 407:491, 2000.

[108] P. Michler, A. Imamoğlu, M. D. Mason, P. J. Carson, G. F. Strouse, and S. K. Buratto. Quantum correlation among photons from a single quantum dot at room temperature. *Nature*, 406:968, 2000.

[109] C. Santori, M. Pelton, G. Solomon, Y. Dale, and Y. Yamamoto. Triggered single photons from a quantum dot. *Phys. Rev. Lett.*, 86:1502, 2001.

[110] R. Brouri, A. Beveratos, J.-P. Poizat, and P. Grangier. Photon antibunching in the fluorescence of individual color centers in diamond. *Opt. Lett.*, 25:1294, 2000.

[111] C. Kurtsiefer, S. Mayer, P. Zarda, and H. Weinfurter. Stable solid-state source of single photons. *Phys. Rev. Lett.*, 85:290, 2000.

[112] P. Michler, A. Kiraz, C. Becher, W. V. Schoenfeld, P. M. Petroff, L. Zhang, E. Hu, and A. Imamoğlu. A quantum dot single-photon turnstile device. *Science*, 290:2282, 2000.

[113] E. Moreau, I. Robert, J. M. Gérard, I. Abram, L. Manin, and V. Thierry-Mieg. Single-mode solid-state single photon source based on isolated quantum dots in pillar microcavities. *Appl. Phys. Lett.*, 79:2865, 2001.

[114] M. Pelton, C. Santori, J. Vučković, B. Zhang, G. S. Solomon, J. Plant, and Y. Yamamoto. Efficient source of single photons: A single quantum dot in a micropost microcavity. *Phys. Rev. Lett.*, 89:233602, 2002.

[115] C. K. Law and H. J. Kimble. Deterministic generation of a bit-stream of single-photon pulses. *J. Mod. Opt.*, 44:2067, 1997.

[116] H. J. Kimble. Comment on "Deterministic single-photon source for distributed quantum networking". *Phys. Rev. Lett.*, 90:249801, 2003.

[117] A. S. Parkins, P. Marte, P. Zoller, and H. J. Kimble. Synthesis of arbitrary quantum states via adiabatic transfer of Zeeman coherence. *Phys. Rev. Lett.*, 71:3095, 1993.

[118] L.-M. Duan, A. Kuzmich, and H. J. Kimble. Cavity QED and quantum-information processing with "hot" trapped atoms. *Phys. Rev. A*, 67:032305, 2003.

[119] M. Hennrich, T. Legero, A. Kuhn, and G. Rempe. Vacuum-stimulated Raman scattering based on adiabatic passage in a high-finesse optical cavity. *Phys. Rev. Lett.*, 85:4872, 2000.

[120] A. Kuzmich, W. P. Bowen, A. D. Boozer, A. Boca, C. W. Chou, L. M. Duan, and H. J. Kimble. Generation of nonclassical photon pairs for scalable quantum communication with atomic ensembles. *Nature*, 423:6941, 2003.

[121] I. H. Deutsch and P. S. Jessen. Quantum-state control in optical lattices. *Phys. Rev. A*, 57:1972, 1998.

[122] H. J. Kimble. Unpublished notes on Stark shifts from January 2002.

[123] G. Laplanche, M. Jaouen, and A. Rachman. Atomic core polarisation influence on single and multiphoton processes in atomic caesium. *J. Phys. B: At. Mol. Phys.*, 16:415, 1983.

[124] D. Cho. Coherent population trapping with linearly polarized pumping laser in multi-Zeeman-sublevel atoms. *J. Korean Phys. Soc.*, 30:373, 1997.